Synthesis and Reactivity of PtZn Nanostructures and Nanocrystals for Heterogeneous Catalysis Applications

Alter Zakhtser

Thèse de doctorat de

Sorbonne Université

L'ECOLE DOCTORALE DE CHIMIE PHYSIQUE ET DE

CHIMIE ANALYTIQUE DE PARIS CENTRE (ED 388)

Synthesis and Reactivity of PtZn Nanostructures and Nanocrystals for Heterogeneous Catalysis Applications

Par **Alter ZAKHTSER**

Présentée et soutenue publiquement le [27/09/2019]

Devant le jury composé de :

Mme. A. COURTY	Professeur	Sorbonne Université	(Présidente du jury)
M. L. PICCOLO	Chercheur	Université Claude Bernard Lyon 1	(Rapporteur)
M. G. HELD	Professeur	University of Reading	(Rapporteur)
M. H. BLUHM	Professeur	Fritz Haber Institute of the Max Planck Society	(Examinateur)
Mme. S. GIORGIO	Professeur	Université d'Aix-Marseille	(Examinatrice)
M. A. NAITABDI	Maître de conférences	Sorbonne Université	(Directeur de thèse)
Mme C. SALZEMANN	Maître de conférences	Sorbonne Université	(Co-encadrante)
M. C. PETIT	Professeur	Sorbonne Université	(Co-directeur de thèse)
M. F. ROCHET	Professeur	Sorbonne Université	(Co-encadrant)

The Contents

The Abbreviations List

AS	As Synthesized
CCD	Charge Coupled Device
EDS	Energy-Dispersive X-ray Spectroscopy
EELS	Electron Energy Loss Spectroscopy
ETEM	Environmental Transmission Electron Microscope
FEG-SEM	Field Emission Gun Scanning Electron Microscopy
HOR	Hydrogen Oxidation Reaction
HRTEM	High-resolution transmission electron microscopy
MTL	Mass Transfer Limitation
NA	Nanoalloy
NAP-XPS	Near-Ambient Pressure X-ray Photoemission Spectroscopy
NC	Nanocrystal
NM	Nobel Metals
NP	Nanoparticle
ORR	Oxygen Reduction Reaction
PEMFC	Proton-Exchange Membrane Fuel Cell
PLIF	Planar Laser Induced Fluorescence
PPh_3	Triphenylphosphine
PROX	Preferential Oxidation
PVP	Polyvinylpyrolidone
QMS	Quadrupole Mass Spectrometer
SEM	Scanning electron microscope
SNOM	Scanning Near-Field Optical Microscopy
STM	Scanning Tunneling Microscopy
TDA	Tetradecylammonium
TDAB	Tetradecylamonium Bromide
TEM	Transmission Electron Microscopy
TM	Transition Metal
TOF	Turnover Frequencies
UHV	Ultra High Vacuum
WGS	Water-Gas-Shift
XPS	X-ray photoelectron spectroscopy

Chapter I. Introduction

1. General Concepts

The general framework of our research thesis concerns the synthesis of well-defined nanostructures and their properties at the nanoscale. In this regard, the atomic-level understanding of fundamental properties of metallic and metal oxide nanostructures represents the main focus of this research. One of the original approaches followed herein was the investigation of these nanostructures under reactive conditions in real-time while the chemical reactions take place. While this approach represented a significant challenge, it provided however the opportunity for better understanding of phenomena that govern their properties and their reactivity.

The thesis research was dedicated to the rational design of efficient and strong nano-structured catalysts, with view to potential applications in the environment remediation and energy generation systems. Our approach within the framework of transition-metal heterogeneous catalysis tackles major challenges and limitations inherent to these nanocatalysts. These include the requirement to better control the size, the composition and the crystallinity of nanoparticles, on the one hand. The handling of issues related to the catalytic activity which include the sintering, deactivation and active sites poisoning, on the one hand. It also seeks suitable pathways to better investigate major chemical reactions in in situ conditions such as the CO oxidation on the other hand. The original approach followed here consists in monitoring these phenomena (chemical reactions, surface segregation…) in in situ conditions in the presence of the reactive environment. In particular, we designed PtZn nanocrystals with controlled size, shape and surface composition with drastic reduction of the precious metal loads. The use of more abundant but efficient materials, Zn, and the possibility to tune the structure as a function of the desired chemical reaction and durability expectations represent an exquisite goal. Probing their properties at the atomic level will provide access to valuable insights into the understanding of central phenomena that govern the activity of catalysts such as the structure/nature of active sites and catalyst-reactant interface. Ultimately, we will take advantage of these phenomena to provide long-life catalysts with enhanced activity.

The investigation of fundamental properties of nanocatalysts especially under their realistic conditions of pressure and temperature represents a real strategy toward a deeper understanding of their chemical state and reactivity.[1–3] Therefore, we have designed PtZn nanocrystals and their model catalyst analogues, ZnO nanostructures supported on Pt(111), and implemented

methods to monitor their catalytic activity using state-of-the-art environmental techniques. Indeed, in-situ studies of nanocatalysts are among the current trends being actively explored in heterogeneous catalysis. While Pt is one of the most prominent transition metal catalysts owing to its relevance in a wide range of industrial applications,[4–6] in particular in the composition of environmentally friendly energy generation solutions such as hydrogen fuel cells,[7,8] it however suffers from several drawbacks including rapid deactivation due to CO poisoning, material dissolution and high cost. In this regards, we have designed PtZn nanocrystals and nanostructures in order to deal with these issues. By essence the catalysts are flexible and often undergo structural and surface composition changes under chemical reaction conditions,[9,10] so that their properties before and after the reaction may differ noticeably.[11] Thus, determining the active phase, chemical composition and morphology of the catalysts is better achieved when in situ investigation techniques are used. In particular, near ambient pressure X-ray photoelectron spectroscopy (NAP-XPS),[12,13] which fits perfectly within these requirements, provides direct access to the surface elemental composition, gas phase in the vicinity of the surface (product of the chemical reaction), oxidation states of the catalysts and their evolution during the reaction under gas pressure up to 25 mbar. It also allows the monitoring of a chemical reaction as it takes place, for example the CO oxidation can be observed through the CO_2 gas phase uptake near the surface and the chemical nature of the adsorbates.[3]

The investigation of CO oxidation, which is also considered as a paradigmatic reaction that provides valuable insights on more complicated catalytic reactions,[14] remains still challenging under reaction conditions due to the changing of the structure and chemical composition on bimetallic nanocatalysts. A common occurrence under high pressure exposure to reactive gases, such as O_2, are dynamic changes of the surface chemical composition and structure. Therefore, real time monitoring of the CO oxidation reaction in in situ conditions is greatly needed, particularly in bimetallic Pt-based nanocatalysts in order to identify the nature of the active sites, the gas-surface interaction mechanism and the role of each constituents. Because of a wealth of physical and chemical phenomena occurring, CO oxidation studies address also the key practical issue of CO pollution control, in automotive exhaust gas and in the CO-abatement in H_2 produced via steam reforming of natural gas (still the main source of hydrogen). In hydrogen fuel cells CO contaminant leads inevitably to the poisoning of Pt catalyst at the anodes. Herein, the catalysts play a prominent role, therefore new research strategies are emerging in order to address these issues and produce catalysts with enhanced activity and long-term stability. Within these current trends, efforts are deployed towards the design of strongly

stable Pt-based catalysts. Thus, Zn, has recently emerged as one of the most prominent candidate to form enhanced Pt-based catalysts owing in part to its greater "affinity" with oxygen compared with that of the noble metal Pt, and the stability of its ZnO oxide under oxidizing or reducing conditions. This system is within current trends dedicated to the investigation of ultrathin films of metal and metal-oxide overlayers on crystalline surfaces.[15–17] These systems exhibit remarkable structural and electronic properties different from their bulk analogues, at the basis of their use in a broad range of applications, especially in heterogeneous catalysis.[18,19]

1.1 What is Nanoscience?

'Nanos' means 'dwarf' in Ancient Greek, and like other prefixes borrowed from Greek or Latin, 'nano' is used to denote a certain fraction of physical quantities. In this case, we are talking about one billionth of an amount. For sufficiently small systems, the functional properties of materials or their individual components begin to depend on the sizes of the objects. The point is that the basic characteristics of a substance as a whole, usually regarded as a constant (hardness, electrical conductivity, colour or chemical activity of small particles) for any given material, begin to depend on the particle's size. This effect cannot be observed in bulk materials or in larger particles. The establishment of a nano-region in the range of 1-100 nm is of particular importance, since it is in this area of dimensions that the most completely new object properties appear. Nanostructures can be produced using top-down methods (the main principle of which consists in the gradual reduction of sizes from the macro through to the micro- and nano-region), as well as through bottom-up methods based on atomic or molecular synthesis of larger and more complex structures.

1.2 Brief Historical Overview

Even the ancient Romans used ultra-fine particles of gold or silver and gold in order to give glasses and other glass products a particularly distinctive colour. The effect was achieved by introducing a noble metal into the nanoparticle material, which gave the glass unusual optical properties.

Figure I-1. Lycurgus Cup. A glass on which particles of 70 nm in size are applied (containing seven parts of silver and three parts of gold) appears green in reflected light and red when illuminated from behind.

Strictly speaking, the famous American physicist Richard Feynman should be considered the true forerunner and founder of today's nanotechnology (NT). He examined the consequences of limitless miniaturization from the standpoint of theoretical physics in extensive detail in his famous speech to the American Physics Society in December 1959. Vaguely speaking, Feynman analyzed the possibilities of changing the scale of electromechanical devices, electrical circuits and the problem of recording, compressing and storing information. Feynman's ideas seemed fantastic to the listeners, since the practical implementation of the devices and mechanisms offered to them was considered a problem for the distant future or even entirely impossible. Today we are convinced that the ideas of the great physicist have turned out to be quite realistic, and many of them are already embodied in mathematical calculations and practical applications. At the same time, Feynman himself did not use the term "nanotechnology" - this concept came in use later, suggested by Japanese Norio Taniguchi in 1974.

The invention of the raster tunnel microscope at the end of 1981 was a very important moment in the history of NT, since, for the first time ever, that device made it possible to obtain images of individual atoms instead of their ordered clusters. The Nobel Prize in Physics for the

invention of this valuable device was given to Gerd Binnig and Heinrich Rohrer from the IBM research laboratory in Rüschlikon. The importance of their discovery lay in the fact that the creation of a whole series of instruments, analyzing the behavior of a substance at the molecular and atomic levels became possible, and later the capabilities for controlling the behavior of atoms and molecules were realized. Nevertheless, Binnig and Rohrer were not the only ones receive awards in 1986. Half of the Nobel Prize was awarded to Ernst Ruska "for his fundamental work in electron optics, and for the design of the first electron microscope". Despite some difficulties, those tools remain in strong demand in imaging and exploring the nanoworld to this day.

Thus the development of nanoscience is based on the encounter of small objects (nanoparticles, single crystal surfaces etc.) and advanced investigation techniques, which permit us to conceptualize the structure of nano-objects on an atomic scale - as well as on their response to environmental changes, chemical reactions or other external stimuli.

2. Synthesis of Nanoparticles

2.1. Nanoparticles synthesized by Colloidal Synthesis Methods:

Modern colloidal chemistry is based, on the one hand, on the idea of a high degree of dispersion of colloidal systems, and on the other, on the physical chemistry of surfaces. Their combination creates a single theoretical basis for this science. Freundlich's famous work “Kapillarchemie” (1909) is the first systematic and very deep reflection on colloid chemistry from the standpoint of the physical chemistry of surfaces.

The first scientific and rational studies on nanomaterials is the famous Michel Faraday's work in the mid-19th century,[20] in which he succeeded to synthesize the first colloidal gold particles by reducing an aqueous solution of chlorauric acid (Fig. I-2). He will replicate this study with other metals.

Figure I-2. Gold nanoparticles solution from M. Faraday work preserved since its synthesis at the Royal Institution of Great Britain

In his research, M. Faraday reports that the pink coloration of the solution (Fig. I-2) was due to the presence of very small gold nanoparticles not detectable by the techniques of the time. It would take a century for Turkevich et al to study these solutions by transmission electron microscopy (TEM) to reveal that these ruby-colored colloids produced by Faraday were indeed gold particles with an average size of 6 ± 2 nm.[21]

Since this seminal work numerous studies were reported on metallic nanoparticles. Indeed, the large family of nanomaterials and more specifically of metallic and bimetallic nanocrystals represent a particularly interesting class of materials owing their potential use in catalysis, ultra-high density magnetic recordings, and new development in sustainable energy (*i.e.* fuel cells). In order to study these specific properties, a wide variety of both chemical and physical routes have been developed for the synthesis of metallic nanoparticles.

Metallic nanoparticles will initiate important development in nanotechnologies due to their specific chemical and physical properties (*i.e.* in catalysis, magnetism, optics, etc). It is now well known that these properties are mainly controlled by the fine tuning of structural parameters such as the size, shape, the chemical composition, the surface states and ligands

adsorption. Concerning their fabrication, the bottom up approach, either physical or chemical, is ideal to design this specific class of nanomaterials due to its versatility, facility and low cost. However, the realization of well controlled metallic and especially bimetallic nanoparticles is not always straightforward from the know-how developed for the synthesis of inorganic nanoparticles.

In a sustainable approach, soft chemistry is well-adapted to produce such material in large amount. However, at the nanometer scale, as the properties are strongly dependent on the size and the surface state (raw or passivated), it is crucial to develop method where the polydispersity in size and composition is finely controlled. These impose to clearly separate the nucleation step from the growth process and also to control this latter to limit the size. This can be done by using colloidal assemblies, as the micellar media or the two phase system, where both the nucleation and growth process are clearly separate in space and time.[22–25] More recently the organo-metallic approach has taken a growing place in this chemical route as this process allows decreasing size distribution.[26] Furthermore, chemical routes offers a wide variety of experimental conditions. Nanocrystals obtained by these routes are usually in the form of colloids. Thus the main advantages of the chemical methods is the ability to manipulate nanocrystals after synthesis. Indeed the post-synthesis treatments, the functionalization of surfaces or self-assembly process allow the chemist to manufacture new materials with specific properties bearing on the properties of new nanoalloys.

Two aspects of these materials have to be taken into account to elaborate the chemical process: on one hand the controls of the size and the size distribution, in order to control the physical and chemical properties and on the other hand, in the specific case of nanoalloys, the control of the composition.

2.2 General Concepts

The simplest and most often used method to produce metallic nanoparticles is to reduce the corresponding metal precursor in a solution in presence of protecting agent or in confined media to limit the growth.[27–29] In this last case, the size is determined by the size of confined media. More generally the size is determined by the number of atoms produced and the number of the nanocrystals formed, which are dependent on the kinetics of nucleation and growth of the nanocrystals.

As the physical and chemical properties of the metallic nanocrystals depend on their size, one of the key point, especially for application development, is to control the size distribution and,

in case of the nanoalloys, the homogeneity of the composition. This can be done by the separation of nucleation and growth (as in the organometallic method) and diffusion controlled growth (as in liquid-liquid phase method or by using colloidal systems as nanoreactor). The kinetics of these competing processes can be altered by changing the experimental conditions

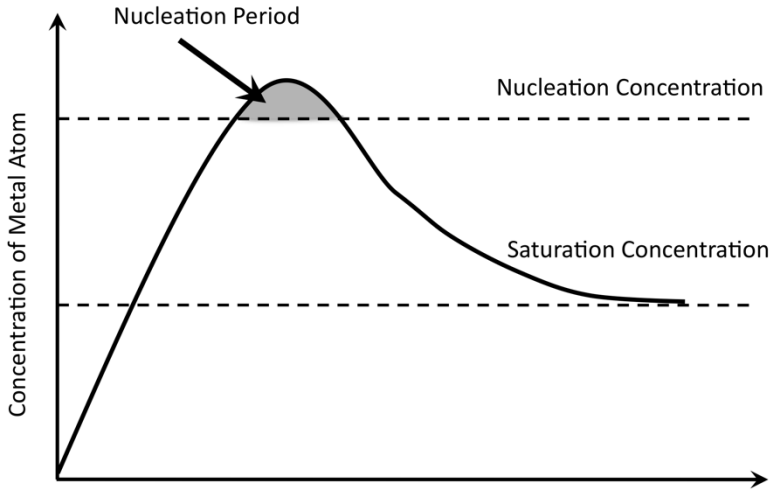

Figure I-3. The LaMer diagram illustrating variation of the monomer concentration with time during the growth process to obtain monodisperse population of nanocrystals (Redrawn from ref[31])

(temperature, pressure, solvent type or nature of the metallic precursor, reducing agent or capping agent). LaMer in his pioneering work published in 1946 proposed a general framework to understand qualitatively the role of the control of nucleation process.[30]

LaMer considered the case of a homogeneous nucleation process. Due to the evolution of the system from a homogeneous phase to a heterogeneous phase (liquid + nanocrystals), there exists a high energy barrier, the LaMer plot shows how this energy barrier works to separate nucleation and growth step (Fig. I-3).[31] Three periods can be identified:

i) *In the initiation phase*: the concentration of monomer (the smallest subunit of the crystal) increases continuously even under supersaturated conditions because the energy barrier for spontaneous homogeneous nucleation is very high.

ii) *In the nucleation phase*: the degree of supersaturation is high enough to overcome the energy barrier and nucleation occurs, yielding to the formation of stable nuclei. These nuclei start to growth. As a consequence of these two processes, the monomer concentration decreases until it reaches the level at which the net nucleation rate is zero.

iii) *In the growth phase*: the nucleation is effectively stopped and the particles growth as long as the solution is supersaturated.

In this framework, the concept of 'burst nucleation' can be understood, which is at the origin of the recent development of the organo-metallic route to produce nanocrystals: in this process, nuclei are produced at the same time and then nuclei start to grow without additional nucleation.[28] Conversely if nucleation process occurs during the formation of nanocrystals, the growth histories differ largely from one particle to another yielding to a large size distribution.[32]

In the following, we will describe some of these chemical routes (mainly the reduction of metallic salt and the decomposition of organic precursor and their application to the specific case of the nanoalloys). It is not an exhaustive list but the most common process, which can be used to synthesize bimetallic nanocrystals. We will explain the role of the capping agent and the structuration of the liquid media to limit the growth, yielding to size control.

2.3. Reduction of Metallic Salts

This is the simplest method used to produce metallic nanoparticles, more often monometallic as Ag, Au, Pd, Ru, Pt etc. This occurs in presence of polymer or capping agent or in confined media to control the size. Most commonly used reductants are sodium borohydride, hydrogen or alcohols. This method is illustrated by the work of Turkevich synthesizing stable solution of gold nanocrystals in water by using citrates ions both as reductant and stabilizer (stabilization occurs by electrostatic repulsion due to the charge of the citrates ions surrounding the nanocrystals).[21] Reduction of metallic salts by sodium borohydryde has been largely used to synthesized mono or bimetallic nanocrystals.[27,28]

2.4. Synthesis in Reverse Micelles

In order to control the size and also to separate nucleation and growth, confined media has been largely used. This is the case of reverse micelles (water in oil nano-droplets stabilized by a surfactant). The *in situ* synthesis in the water-pools of reverse micelles was developed in the 80's by Pileni *et al*.[22,33] In this method, the inner core of the reverse micelles can be considered as a nanoreactor and the size of the nanoparticles obtained is often approximately limited by that of the water pools. This is illustrated by the scheme presented in Fig. I-4. Nucleation first

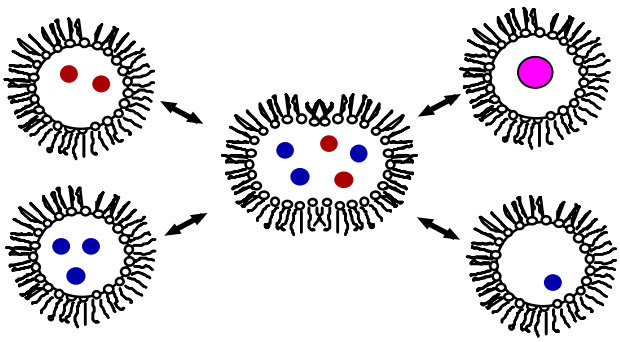

Figure I-4. Scheme of the inorganic synthesis using reverse micelle as a nanoreactor. Solution A (blue) and B (red) are mixed. Due to Brownian motion, inter-micellar exchanges are possible, yielding to reaction in confined media and formation of inorganic nanocrystals in the water-pool.

takes place inside the water-pool and then growth process occurs at the minute scale due to inter-micellar collision.

This method has been used for synthesis of semiconductor materials such as CdS[33] or CdSe[34], of metallic nanoparticles such as Pt[35], Cu[36], Co[37], Ag[38], and Au[39] but also of nanoalloys such as CoPt[40–42], PtPd[43], AgAu[44], AuFe[45]. In this last case the control of composition is reached due to the simultaneous location at the interface of the micelle of both metallic precursors yielding to an effective control of the average composition. Nanocrystals can be extracted from the micellar media by anchoring a strong capping agent as alkane thiols or dodecanoic acid to the metallic surface of the nanocrystals. Micellar media is then broken and passivated metallic nanocrystals can be recovered as a powder easily dispersible in organic solvent.[37,39]

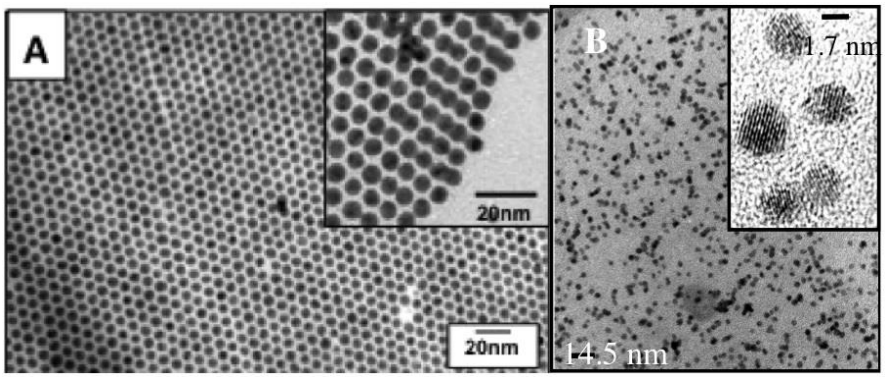

Figure I-5. TEM image of A) Gold Nanocrystals synthesized in situ in AOT reverse micelles (from ref[39]). B) CoPt nanocrystals synthesized in situ in AOT reverse micelles (from ref[21]).

There is, however, some limitation to the micellar way, mainly the low yield of formation of the nanocrystals and the difficulty to control the size polydispersity as the growth process is not completely separated from the nucleation step. This last difficulty can be overcome by using

post-synthesis process as the size selection precipitation. Fig. I-5 and I-6 show some example of metallic and bimetallic nanoparticles obtained by this way.[45]

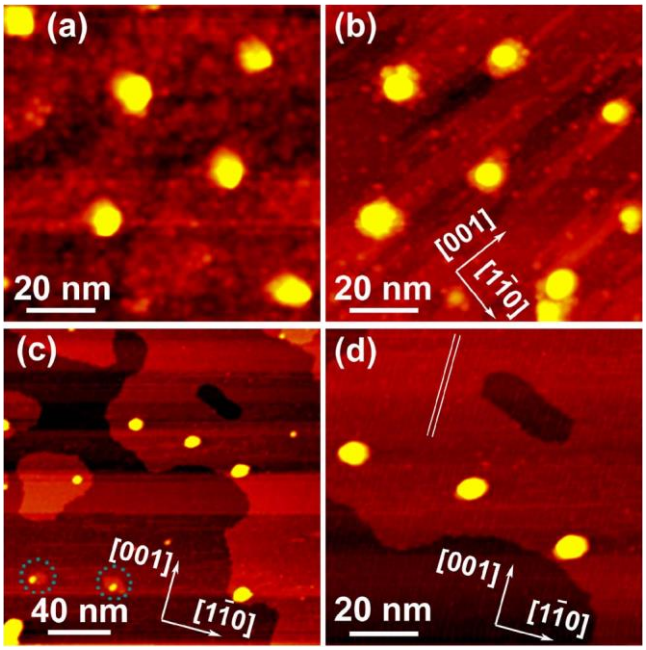

Figure I-6. STM images (Vt = 1.0 V , It = 0.30 nA) of $Au_{0.5}Fe_{0.5}$ NPs on TiO_2(110) measured at 15 °C after an O_2-plasma treatment and subsequent annealing at 300 °C, 20 min (a), 900 °C, 10 min (b) and 1000°C, 10 mn (c and d) (from ref[45]).

2.5. Two-Phase liquid-liquid Synthesis

The second method involves transfer of the metal ion from a polar phase to a non-polar phase using a transferring agent. It has been used for synthesis of metallic nanoparticles and the phase transfer method, also called two-phase synthesis, has been developed by Brust *et al.* in the 90's.[46,47] It has been largely used to synthesize metallic nanoparticles as silver, gold, platinum or palladium but also bimetallic nanoalloys as AgAu[48] or CoPt[24]. It typically involves the

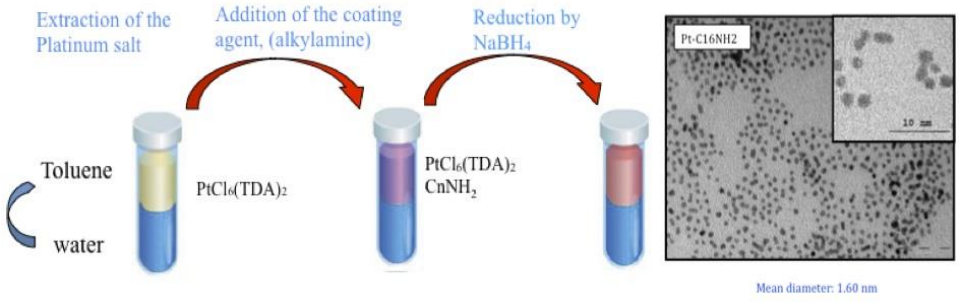

Figure I-7. On the left, two phase liquid synthesis of platinum nanocrystals. On the right, TEM picture of Platinum nanocrystals after extraction from the media and dispersion in toluene (from ref[24]).

transfer of the metal precursor (metallic ions) from an aqueous solution to an organic solution containing a ligand as alkane thiol or amine. The transfer is assisted by a phase transfer agent such as tetradecylamonium bromide (TDAB). Reduction of metallic precursor is then carried by adding an aqueous solution of reducing agent (mainly $NaBH_4$) (Fig. I-7)

The reduction takes place at the interface between the two phases. The nuclei are mainly solubilized in the organic phase due to the presence of both the capping molecule and phase transferring agent where the growth process takes place. The interest of this method is that the kinetics of nanocrystal growth is controlled by the surface coverage and thus cluster size is controlled by the reaction conditions at the interface and not by the metal-ion reduction kinetics in the homogenous aqueous phase. Nanocrystals coated by ligand as alkylamin can then be recovered as a powder and dispersed in an organic solvent. Synthesis conditions such as concentrations of the metallic salt, the reducing agent and the nature of the capping agent (strongly or weakly anchored, the length of the alkyl chains[49]) allow to control the kinetics of nucleation and growth of the nanocrystals and then the size. In most of cases, this method can produce large amount of nanocrystals with a low size distribution (around 10%).

Only few works deal on nanoalloys obtained by this two-phase synthesis due to the difficulty to control their composition. In the case of CoPt synthesis.[24] Perfect control on the composition can be only achieved if the two precursors are similar in structure and in location in the liquid media. As a matter of fact the large difference in redox potential of platinum and cobalt can induce a variation in the reduction kinetics.[28] Therefore the kinetics of nucleation differs for the two components and as a consequence a strong discrepancy occurs in the average content of the cobalt in the nanocrystal compared to the expected ratio. Conversely if both cobalt and platinum salts are in the organic phase interacting with an interface as in the liquid-liquid phase

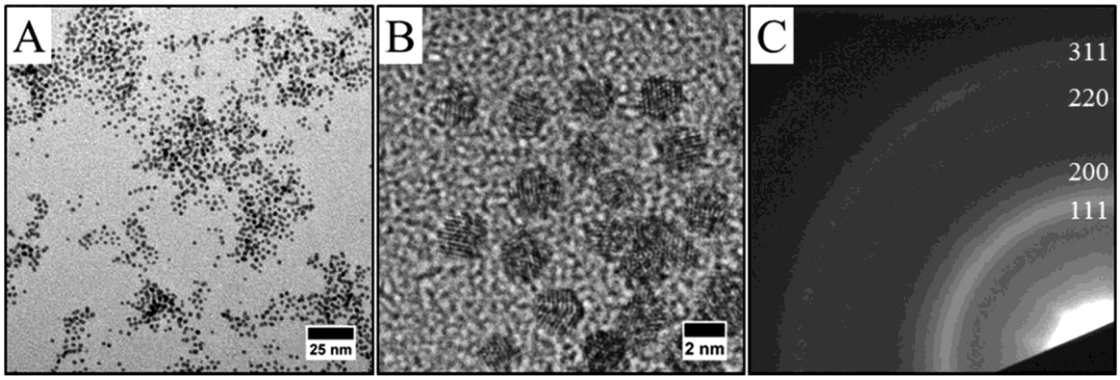

Figure I-8. TEM images (A), HRTEM images (B) and electronic diffraction (C) of ($Co_{30}Pt_{70}$) (from ref[6]).

transfer method, only the reaction conditions are predominant and the difference in redox potentials is no longer a problem for this interfacial reaction.[50] Thus, the best results are obtained when cobalt is in the same form as the platinum: $CoCl_2(TDA)_2$ and $PtCl_4(TDA)_2$, *i.e.* both complexed by the same agent transfer. These two molecules have a similar structure and then the composition of the interface where the reduction takes place is directly related to the initial composition of metallic precursor. Hence, the reduction yields to a precise control of the composition. Fig. I-8 shows typical CoPt nanoalloys obtained by this two-phase synthesis.

2.6 Single Phase Synthesis

Numerous groups in the world develop single phase methods to synthesize metallic and bimetallic nanocrystals. In these methods, the metal precursor, the reducing agent and the ligand are all dispersed in the same solvent. This can be done either using $NaBH_4$ to reduce metallic ions in a water/methanol solution in presence of hydrophilic ligand to control the growth or using a strong hydrophobic reducing agent to reduce metallic complex solvated in an organic solvent in presence of hydrophobic ligand. Thus the reduction, nucleation and growth occur homogeneously and not at an interface or in confined media. This could yield to a better control of the nanocrystals nucleation and growth.[28,32]

Another method based on single phase synthesis is the "polyol process". In this case, the solvent, diol or polyalcohol (as ethylene glycol for example) acts as a reducing agent to reduce the metal salts. However, contrary to the previous one, this reaction is performed at high temperature (typically 100-200 °C). This has been largely used in case of nanoalloys as FePt[51] or NiPd[52]. Hence, the use of iron acetylacetonate ($Fe(Acac)_3$) and platinum acetylacetonate ($Pt(acac)_2$) in ethylene glycol or tetraethylene glycol, generates FePt nanocrystals. Oleic acid or oleic amine are often used as ligands and added directly in the chemical bath to limit the growth process. Furthermore, this high temperature process often allows to reach a better crystal quality and to avoid boron contamination often observed in monometallic nanocrystals obtained by single phase borohydride reduction.[28]

2.7 The Organometallic Route: Thermal Decomposition Method

In case of the nanoalloys, the derivated co-reduction method is often used. However as the two metal precursors are involved in the reduction reactions, the influence of the experimental conditions on the nucleation and growth is complex as it has been illustrated in the case of CoPt obtained by the two phase method. Thus, the size distribution and crystalline structure of the nanoalloys are difficult to control by these methods. Some problem of reproducibility could

occur depending on the purity of the metallic precursor or of the reducing agent. Furthermore, changes in the composition of the nanoalloys have been reported, often coupled with changes in the nanocrystals size and size distribution.[53]

This is the reason of the development of the organometallic route, in which fast thermal decomposition reactions of organometallic or metal-surfactant complexes were performed at high temperature in presence of surfactant molecules acting as a ligand to prevent the growth. This method is now widely used to synthesize inorganic nanocrystals (not only metallic) because it is a clear example of the concept of "burst nucleation".[28] In fact, as all the precursors have the same structure, they decompose massively at the same time and the subsequent growth by ageing takes place at slightly lower temperature in a media containing the ligand. All the metal atoms generated from the thermal decomposition of the precursor are transformed into polynuclear clusters, which in turns lead to the nucleation and growth of the metallic nanocrystals (Fig. I-9).[26] This is highly profitable in case of nanoalloys where it is important to generate the two components monomer at the same time and with the same kinetics.

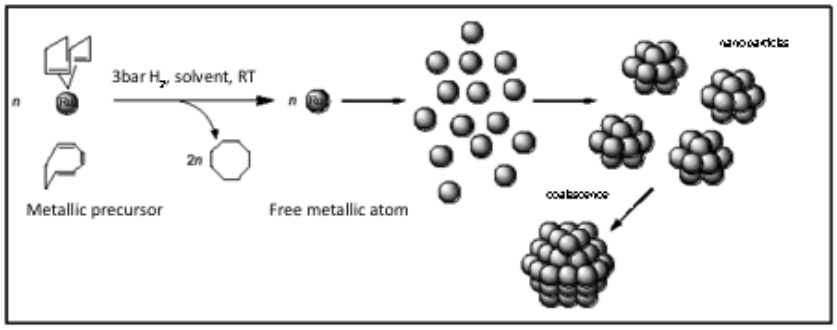

Figure I-9. Schematic of the organo-metallic route for synthesis of ruthenium nanocrystals by decomposition at low temperature under H_2 of ruthenium precursor (ref[26]).

A better separation between the nucleation and the growth step is observed, which yields to very narrow size distribution. Typically, a size distribution between 5 to 10% could be achieved.[28,32] This control of the monodispersity is essentially a kinetic process driven by high initial supersaturation. It requires that the precursor be reactive enough to induce high supersaturation immediately after injection of the precursor in the heated solution (burst nucleation). This allows also a better control of the cristallinity of the nanocrystals, which can be easily dispersed in organic solvents. This route of synthesis, sometimes called "hot injection method", has been developed by the pioneering group of Bawendi for the synthesis of quantum dots[54] and then extended to metal or metal oxides.[29,32] It has been used by the Murray's group

to synthesize FePt nanoalloys by thermal decomposition of $Fe(CO)_5$ in presence of oleic acid and oleylamine.[54] The composition of the nanoalloys was varied by changing the molar ratio of the two metal complexes. Size could be controlled by the concentration of initial precursors between 3 to 10 nm. This has been also used to synthesize $CoPt_3$ or CoPt or even FeCoPt.[28] One of the advantages of this technique is the high yields of formation of metallic nanocrystals, some of the variations of this process allow gram scale synthesis of nanocrystals. However, it is more complex than the co-reduction method and some problem of reproducibility have been observed. It should be mentioned that, it is also possible to control the structure of the nanoalloys, either homogeneous or core/shell.[55] The organo-metallic route was also widely developed by Chaudret and collaborators.[26] For example, they synthesize PtRu nanocrystals by decomposition at low temperature of organometallic precursors under dihydrogen in the presence of polyvinylpyrolidone, PVP, as stabilizer.[56]

A method of organometallic decomposition using a progressive increase of the temperature has recently been developed at the MONARIS laboratory. It is based on a simple coordination complex that can be easily synthesized in large quantities ($[CoCl(PPh_3)_3]$) and redispersed in oleylamine.[57,58] Nanocrystals have thus been produced whose size can be controlled with a very low dispersion and which are mainly of hc structure. Typical cobalt nanocrystals obtained by this method are represented on Fig. I-10.

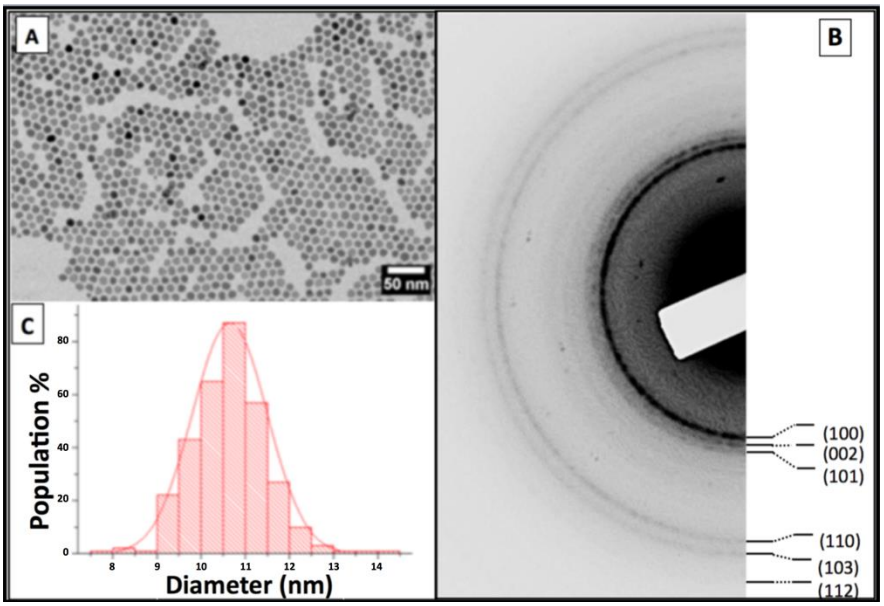

Figure I-10. (A) TEM image of Cobalt nanoparticles obtained by disproportionation of $CoCl(PPh_3)_3$ precursor in a mixture of tetradecane:oleylamine (9:1), (B) the eletronic diffraction showing characteristic patterns of hcp crystalline structure and (C) the corresponding size distribution. (from ref[39]).

3. Analytical Methods:STM, TEM, SEM

Purposeful use of links between the functionality and the size of the substance structures requires, above all, the creation of appropriate equipment. The desire to minimize the characteristic dimensions of technical devices and their elements is apparently one of the most important motives for the development of new technologies and an essential element of technical progress in general. Inventors have always sought to reduce the size of technical details, both to increase the functionality of the whole system, and for greater ease of use and operation for economic reasons.

Strictly speaking, the complex measurement of the structure parameters of any object consists primarily in the exact quantitative description of its three-dimensional geometry with sufficient accuracy, and the next stage of the analytical study is to determine the required functional properties of this structure (for example, its chemical composition, electrical conductivity, mechanical and optical properties, etc.). The description of the geometric and functional properties of the structure under study is carried out, formally speaking, by appropriate devices or probes. The general process of research and analysis is to cause the sample to "react" to the effects "provoked" by the probe, which makes it possible to obtain information on its physicochemical properties.

Many analytical methods are enable to solve many practical problems associated with NT (for example, they cannot reveal the absence of individual atoms on the surface of a silicon crystal or determine the exact position of defects). More accurate information (at the level of the atomic

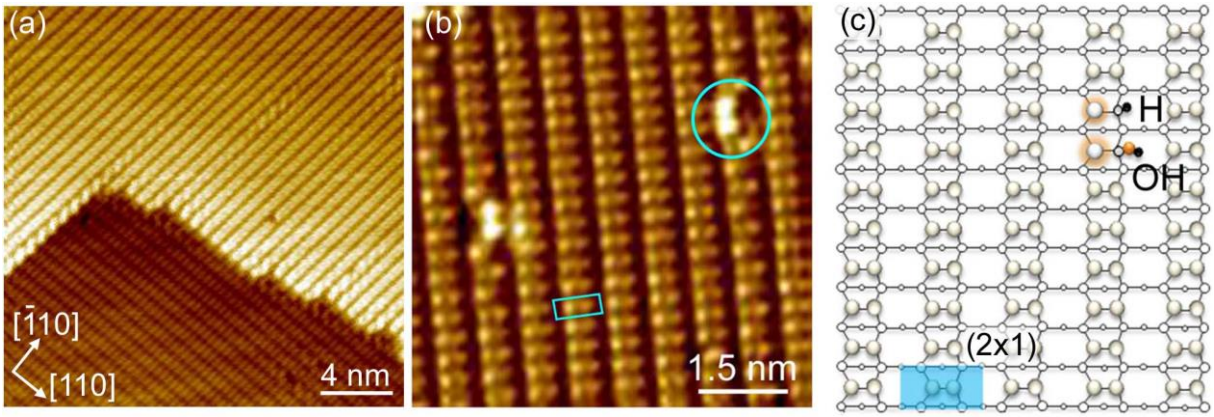

Figure I-11. Filled-state STM images (bias = -2V, It = 100 pA), of a pristine n-doped Si(001)-(2×1) (highly n-doped ρ = 0.003 Ω × cm). (a) large scale image, (b) high resolution STM with atomic resolution, and (c) the schematic representation of a part of the Si(001) surface shown in (b). The solid circle in (b) indicates a C-defect. The rectangle indicates a (2×1) unit cell. (from ref[59]).

structure), if necessary, can be obtained using high-resolution scanning microscopes (Fig. I-11 from ref[59,60]).

To measure and analyze individual nano- and subnanostructures, it is necessary to develop new microscopic techniques that have a sufficiently high spatial resolution and allow to investigate local features of objects, the scale of which is determined by the size of the elements of the analyzed structure that interest us.

3.1. Scanning Probe Microscopy

In scanning probe microscopy, a local probe moves "line by line" along the surface of the sample and, following the corresponding offset of individual "rows", creates a two-dimensional image of the area under study.

It seems obvious that the methods that can really achieve the spatial accuracy (resolution) of the order of nanometers or even less will be of particular importance in the development of NT. These possibilities are provided by a scanning tunneling microscope (STM), created in late 1981 by IBM research laboratories in Zurich, Gerd Binnig and Heinrich Rohrer, which was the starting point for a number of scanning and probe methods in microscopy. This method is based on a single physical approach, which consists in the fact that the local probe moves "line by line" above the sample surface, allowing to obtain information about the structure with nanometer accuracy. Experiments of this kind allow not only to analyze the composition and structure of the sample, but even to purposefully modify the surface under study, which erases the difference between the study and the surface treatment. The use of various probes and a change in environmental conditions makes it possible at the present time to conduct extremely interesting and versatile experiments in the nanometer range, practically with any samples.

The general scheme of the structure of a scanning probe microscope is shown in the Scheme I-1. The central part of the device is a piezoelectric element that allows to create the desired position of the probe relative to the sample surface. The piezoelectric effect is that the electric field in some materials (the so-called piezoelectrics) causes changes in the crystal structure, meaning its expansion or contraction in some directions, and this effect manifests itself in very different forms. The probe microscope uses the so-called transverse piezoelectric effect (in

which the applied electric field E is directed perpendicularly to the axis of expansion / compression).

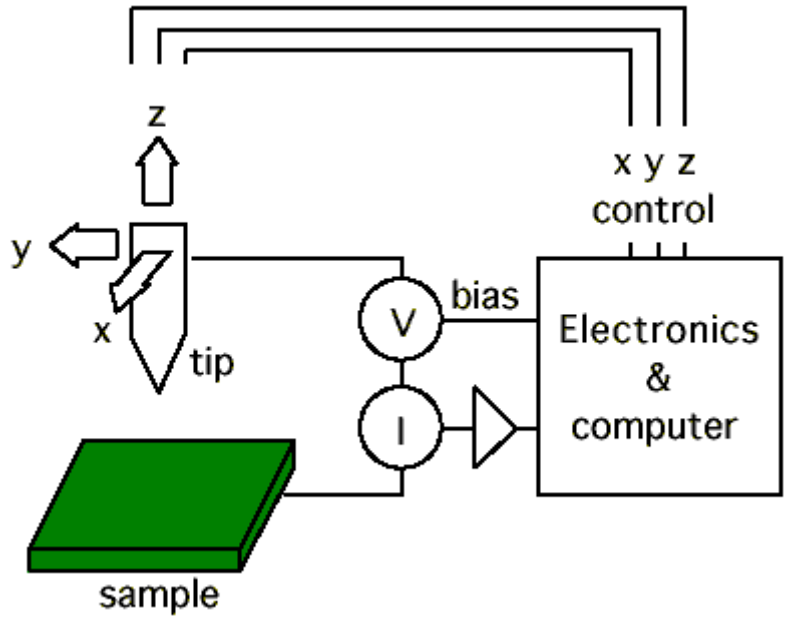

Scheme I-1. General scheme of a scanning probes experiments. The curse of the tip is controlled by piezoelectric devices. Electronic included the feedback loop to control the tip-surface distances.

The piezo resizing is described by the formula:

$$\Delta L = L\frac{V}{t}d_{31}\ ,$$

Where d_{31} denotes the so-called vertical piezoelectric constant of a substance.

A rather complicated technical problem with such measurements is that in the initial state (the beginning of the experiment) the probe and the sample must be separated from each other by a macroscopic distance (millimeters) so that the signal cannot be read from the surface of the sample by scanning. With a sufficiently small working distance between the probe and the sample, the signal at the detector output reflects the properties of the sample under study due to the use of a piezotube. The lateral region of the raster is usually from 1 μm to 100 μm, and the typical distance between the probe and the sample is from a fraction of a nanometer to several tens of nm. At sufficiently low temperatures (for example, at a boiling point of liquid helium of 4.2 K), the inhomogeneities of the motion of the piezotube are significantly reduced, since the piezoelectric constant d_{31} is very dependent on temperature. For the “coarse” installation of the probe (within a millimeter with an accuracy of the order of 1 μm), one can use peculiar piezoelectric motors.

In principle, scanning probe methods can be used in a wide variety of environmental conditions (in many cases they should be operated under normal conditions and at room temperature), but scanning tunneling microscopy is very sensitive to contamination and surface heterogeneity, which under normal conditions is almost unavoidable. For more accurate measurements with a minimum level of impurities, experiments should be carried out in an ultra-high vacuum (pressure of about 10^{-10} mbar), so scanning microscopy is often combined with high-vacuum installations, inside which are mounted devices for preparation and analysis of samples, as shown in the Fig. I-12. Naturally, the operation of such complexes is carried out at low temperatures (in the range up to millikelvin).

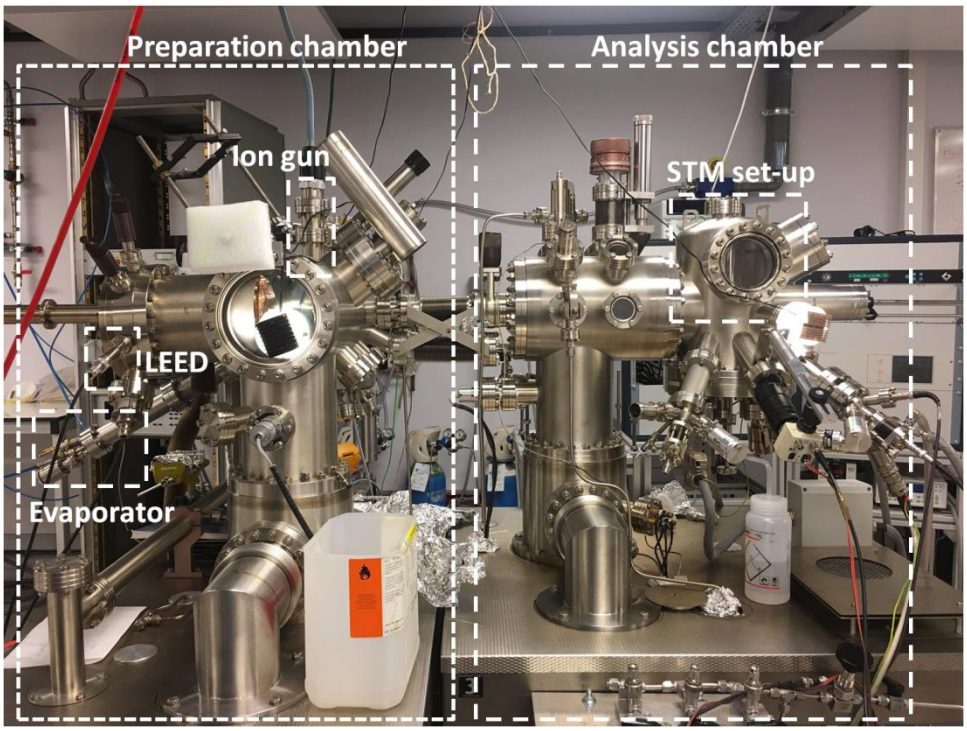

Figure I-12. The real STM setup used in our experiments.

The decrease in heat energy (kT) improves the energy resolution, but lowers the dynamics of many processes associated with temperature, especially in cases where the analyzed phenomena depend on the corresponding phase transitions. For example, the occurrence of superconductivity refers to low-temperature effects, although in some cases it is naturally necessary to work at high temperatures of the sample (for example, when studying melting processes, etc.). In such situations, it is necessary to carefully monitor the distance between the probe and the sample surface and take into account thermal effects.

Probes for tunneling microscopes are made by electrochemical etching of metallic conductors through which an electrical tunneling current must flow, which has a complex physical nature (superposition or other interaction of electronic orbitals between the atoms of the sample and the probe). Naturally, such processes very strongly depend on the distance between the probe and the sample, which, strictly speaking, is used to register very small differences in the interatomic distances. The described microscopes are based on this principle, which makes it possible, with very high registration accuracy, to obtain current-related atomic structures on the sample surface and even to guess the patterns of their structure with atomic accuracy.

Scanning methods are based on a single hardware concept, in which the use of a piezoelectric element to determine the position of the probe relative to the sample surface plays a central role, which, due to very small distances, requires the use of complex closed control loops. Scanning microscopy methods have great promise for the study of nanostructures.

3.2. Electronic Microscopies (Transmission, TEM and Scanning, SEM)

In catalysis, new active, stable and more efficient nanocatalysts appear for a wide range of environmental applications from pollution control to the development of clean and renewable energies. For these applications where nanomaterials are subjected to a gaseous environment, characterization under vacuum or by post-mortem studies provides only very partial information on the structural states that nanomaterials adopt during their operation. Indeed, nanoparticles generally expose different surface sites simultaneously, each with a different reactivity depending on the reactive gas used. A detailed study of the surface of nanoparticles and the specific reactivity of a site is therefore necessary to understand the catalytic mechanisms involved and thus improve the performance of catalysts of the future. Crystal structures can be determined by X-ray and neutron diffraction, while transmission electron microscopy (TEM) is indispensable for characterization of nanocrystal materials. For example, using an electron beam with an acceleration voltage of 200 kV, the wavelength of the electron beam is 2.5 pm (well below 1 nm). Although scanning tunneling microscopy and atomic force microscopy can provide atomic-resolution images of large crystal surfaces (see above), they are unlikely to clearly resolve the atomic lattices of nanoparticles because of the surface coating and the wobbling of the nanocrystals under the scanning tip. TEM is likely to be very powerful for revealing the atom distributions on nanocrystal surfaces even when they are passivated with polymers. Indeed, the physical and chemical properties of nanophase materials rely on their crystal and surface structures. Transmission electron microscopy (TEM) is a powerful and

unique technique for structure characterization. The most important application of TEM is the atomic-resolution real-space imaging of nanoparticles. By forming a nanometer size electron probe, TEM is unique in identifying and quantifying the chemical and electronic structure of individual nanocrystals. Electron energy-loss spectroscopy analysis of the solid-state effects and mapping the valence states are even more attractive. In situ TEM is demonstrated for characterizing and measuring the thermodynamic, electric, and mechanical properties of individual nanostructures, from which the structure-property relationship can be registered with a specific nanoparticle/structure.[61] Today's TEM is a versatile tool that provides not only atomic-resolution lattice images but also chemical information at a spatial resolution of 1 nm or better, allowing direct identification the chemistry of a single nanocrystal. With a finely focused electron probe, the structural characteristics of a single nanoparticle can be fully characterized. TEM is unique for characterizing the in situ structural evolution of nanocrystals resulting from annealing, electric field, or mechanical stress. However, nanoparticles often respond dynamically to changes in the surrounding environment. This effect is mainly due to changes in the composition of the reaction gas or liquid which induces changes in the free energy of the exposed surfaces.[1] The structure of the surface and the reactivity are therefore coupled to the reaction conditions. It is therefore necessary to study the active sites and their properties in situ and in real time during the catalytic reaction.

The first transmission electron microscope was made in 1931 by Ernst Ruska. In the last decades, transmission electron microscopy was in full expansion. In parallel with technical advances related to the performance of microscopes corrected for aberrations, significant technological developments have been made to study the specific properties of certain materials and their behavior in their application environment. Nanoparticles can now be observed both under gas[1] and temperature as well as in liquid media[62,63] thanks to environmental microscopy, either on dedicated microscopes or in sealed cells obtained from optical masking and etching techniques (micro manufacturing).

From a technical point of view (Scheme I-2), electron microscopes work in a similar way to an optical microscope: a light beam passes through a set of lenses and illuminates the sample being studied. However, as the probe is an electron beam, the lenses are magnetic coils that can deflect the beam. Hence modern TEM is composed of an illumination system, a specimen stage, an objective lens system, the magnification system, the data recording system(s), and the chemical analysis system.[61] The electron gun is the heart of the illumination system, which typically uses LaB6 thermionic emission source or a field emission source. The LaB6 gun gives a high illumination current, but the current density and the beam coherence are not as high as those of a field emission source. Field emission source is unique for performing high coherence lattice imaging, electron holography, and high spatial resolution microanalysis. The illumination system also includes the condenser lenses that are vitally important for forming a fine electron probe. The specimen stage is key to carrying out structure analysis, because it can be used to perform in situ observations of phenomena induced by annealing, electric field, or mechanical stress, giving the possibility of characterizing the physical properties of individual nanostructures. The objective lens is the heart of a TEM which determines the limit of image resolution.

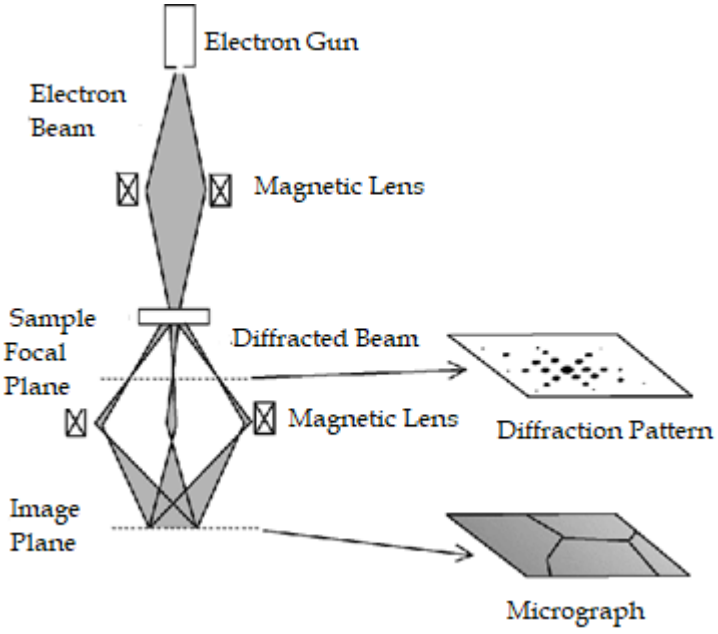

Scheme I-2. TEM Schematic Diagram

The magnification system consists of intermediate lenses and projection lenses, and it gives a magnification up to 1.5 million. The data recording system tends to be digital with the use of a charge coupled device (CCD), allowing quantitative data processing and quantification. Finally, the chemical analysis system is the energy-dispersive X-ray spectroscopy (EDS) and electron

energy loss spectroscopy (EELS), both can be used complementary to quantify the chemical composition of the specimen. EDS relies on the counting of X-rays emitted from the beam-illuminated specimen region as a function of the photon energy, and it is probably the most precise microanalysis technique in TEM. EELS analyzes the intensity distribution of the transmitted electrons as a function of their energy loss. It provides not only the chemical information on the specimen but also its electronic structure. A complementary application of the diffraction, imaging, and spectroscopy techniques available in a TEM is likely to give a more precise and reliable determination of the crystal structure.

Depending on the thickness of the latter, the observation can be made in transmission and/or reflection. These two concepts, as well as the possibility of using an electron beam, have led to the development of two types of electron microscopes: the Transmission Electron Microscope (TEM) and the Scanning Electron Microscope (SEM). During the thesis we worked with a MET-JEOL 1011 and a MET-HR JEOL 2100 F. For the SEM we used a JEOL JSM5510LV and a Hitachi SU-70 SEM-HR.

4. X-Ray Photoelectron Spectroscopy

XPS is a surface-sensitive quantitative analysis technique. With the development of a high-resolution XPS by Kai Siegbahn and his research group in Uppsala University in Sweden[64], XPS allowed to measure accurate binding energy of photoelectron peaks, in which the investigation of electronic structure has been realized. The work of Kai Siegbahn was awarded by the Nobel prize in physics in 1981.

An XPS measurement is operated by irradiating the sample surface with a beam of monochromatic X-rays. If the photon energy is enough, electrons from the sample atoms can be excited and create the photoelectrons, which are then emitted from the sample surface. Figure I.13 is the schematic of a photoemission process. In this process, the electrons on a given orbital are first promoted from a bound state to an excited state by absorbing certain photon energy $h\upsilon$. Before escaping to vacuum, the photoelectrons travel some distance inside the sample, in which the photoelectrons collide elastically or inelastically with the lattice atoms of the sample. The elastically scattered electrons escape from the sample surface without any kinetic energy loss, which will form the main XPS core level peak (also called adiabatic peak). On the contrary, the inelastically scattered electrons escape from the sample surface with losing a part of the kinetic energy, which will create the background of the XPS spectrum. Therefore, the surface sensitivity of XPS is determined by the electron inelastic mean free path (IMFP), which is the

characteristic length that an electron on average travels through before suffering an inelastic scattering. After reaching the sample surface, the photoelectrons still need to overcome a barrier potential which exist at the sample surface in order to get to the vacuum level. That barrier potential refers to the work function of the sample.

In general, the binding energy of a photoelectron coming from the sample can be obtained by the Einstein equation:

$$E_b = h\upsilon - E_k - \Phi_{sample} \quad (1)$$

where E_b is the binding energy of the core level, $h\upsilon$ is the photon energy of the X-ray, E_k is the kinetic energy and Φ_{sample} is the work function of the sample.

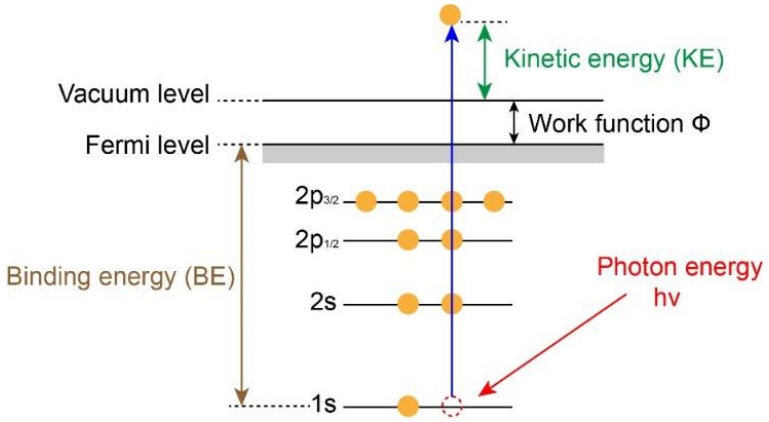

Figure I-13. Schematic of the photoemission process.

Particularly, when the kinetic energy is measured by the XPS analyzer (Figure I-14), the work function of the analyzer should be considered. By grounding both the sample and the analyzer to align the Fermi level, the equation (1) can be rewritten as:

$$E_k = h\upsilon - E_b - \Phi_{analyzer} \quad (2)$$

where E_b is the binding energy of the core level, $h\upsilon$ is the photon energy of the X-ray, , E_k is the kinetic energy and $\Phi_{analyzer}$ is the work function of the analyzer.

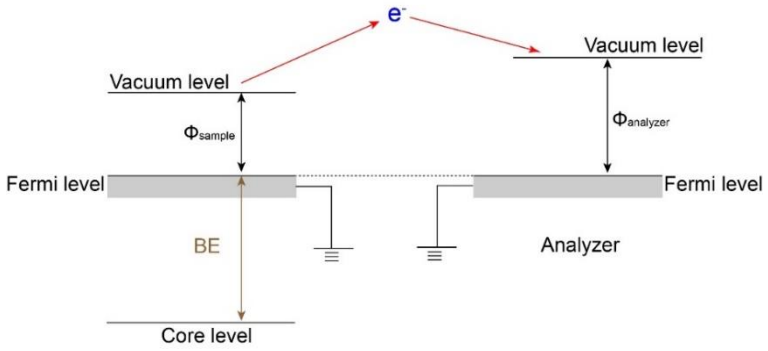

Figure I-14. Schematic of the sample and analyzer energy level.

The binding energy of a core electron measured by XPS is influenced by the interactions between the electron and the surrounding environment, which are Coulomb interactions with other electrons and the attraction from the nuclei. Changes in the chemical environment have an influence on the valence electron of the element, which then lead the electrons to a spatial redistribution and affect the value of the binding energy of the core electron. Consequently, the variation of the binding energy of the core electron is observed as a shift on the XPS peak of the core electron, which is called the chemical shift ($\Delta\xi$). Due to the advantage of XPS, chemical shift can be easily interpretable in XPS spectrum with a well-defined energy position, such as the different oxidation state and different chemical environment.

Due to the spin-orbit splitting effect, all orbital levels (except s orbital) will show two spin-orbit splitting peaks in XPS spectrum, i.e. doublet pairs. Based on the quantum mechanics, the total angular momentum (j) is expressed as:

$$j = l + s \tag{3}$$

where l is the orbital angular momentum ($l = 1$ for p orbital, $l = 2$ for d orbital and $l = 3$ for f orbital) and s is the spin angular momentum ($s = \pm 1/2$). The formula (31) gives two values j_1 and j_2, which corresponds to the two peaks due to splitting, respectively. (e.g. $nf_{5/2}$ and $nf_{7/2}$, where n is the principal quantum number.) Moreover, the relative intensities of the doublet pairs are given by $\frac{j_1+1}{j_2+1}$. Thus, for p electrons the relative intensities are $1:2$, while for d electrons the relative intensities are in the proportion $2:3$ and for f orbital the ratio is $3:4$. Also, the energy separation of the doublet pairs depends on both the principal (n) and angular momentum (j) of the core level electrons and can result in widely separated doublet pairs.

Figure I-15 shows the schematic of the XPS system in UHV. Basically, the system consists of three critical components, which are the X-ray source, the electron analyzer and the

detector with appropriate signal counting electronics. Electrons are first emitted from the sample surface by the X-ray source (usually Mg/Al X-ray source). Then they are supposed to decelerate or accelerate by the electrostatic lenses to the pass energy E_p and focus on the inlet slit. The potentials applied to the inner and outer hemisphere of the electron analyzer correspond to a selection of electrons with the kinetic energy E_p. Therefore, the photoelectrons are registered in a small kinetic energy range, which determines the resolution of the analyzer. Electrons are finally detected by the electron multiplier of the detector in pulse counting mode.

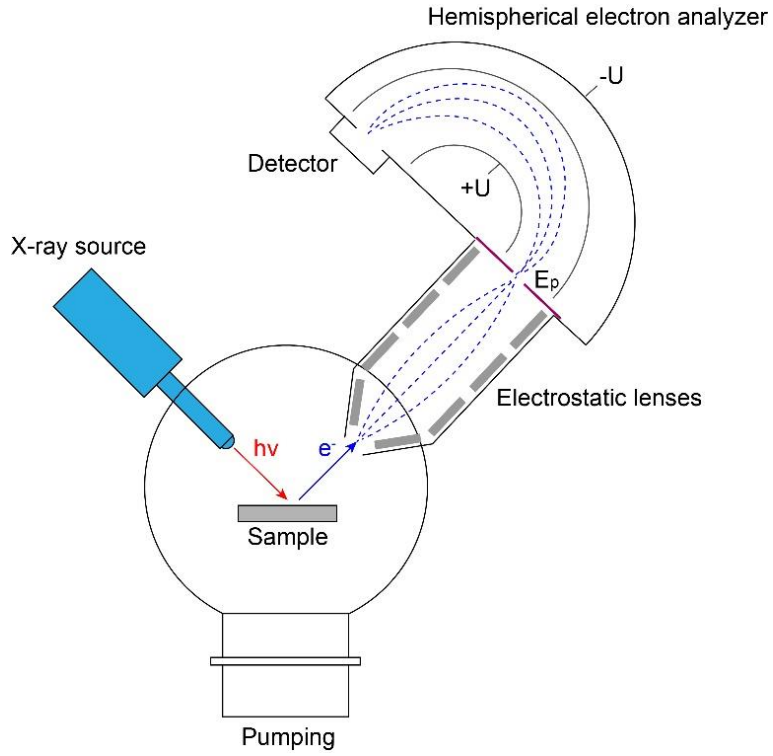

Figure I-15. Schematic diagram of the XPS apparatus in UHV.

4.1. Near-Ambient Pressure XPS

Due to the exponential decrease of the photoelectron signal in gas phase, NAP-XPS technique is designed to partially overcome the pressure gap in surface science. Unlike the ordinary XPS, NAP-XPS allows the sample to be exposed in high pressures in order of millibars, which can study the dynamics of catalytic reactions. The most significant change for NAP-XPS is the introduction of the differential pumping system which dramatically decreases photoelectron attenuation between the sample and the analyzer. Different from the laboratory X-ray source (Al/Mg source) used in the XPS, the synchrotron-based light is applied onto the NAP-XPS, which can produce a high flux of photons and a more focalized size at the sample

generating more photoelectrons. Nowadays, a number of synchrotron-based NAP-XPS setups have arisen all over the world, such as SOLEIL, DIAMOND, BESSY, ALS and SSRL.[65]

A schematic diagram of the SOLEIL synchrotron is shown in Figure I-16. Several steps are involved to obtain the synchrotron radiation. First, the electron beam is emitted by the electron gun, which is then accelerated by the linear accelerator to 10 MeV. The electrons are further accelerated to 100 MeV in the booster ring and up to a maximum energy of several GeV in the storage ring where the electrons are stored. When the electron beam circulates in the storage ring, the trajectory of the electron beam is altered by the dipole magnets and the electron beam is focused by the quadrupole magnets after the change of the trajectory. The beamlines, the end stations, are installed tangentially to take advantage of the synchrotron light for experiments. Comparing to the laboratory X-rays, the synchrotron light has a very broad spectral range, which covers from microwaves to hard X- rays. Thus, the photon energy can be selected based on different experiments. As for the TEMPO beamline, the synchrotron beam, a high flux of photons with the energy range from 50 to 1500 eV, is introduced into the analysis chamber of the NAP-XPS through a Si_3N_4Al window in order to keep the beam in UHV (the pressure range of 10^{-9} mbar).The beam spot has a diameter of 0.1 mm on the sample in the analysis chamber, which makes an angle of 54˚ with the sample normal.

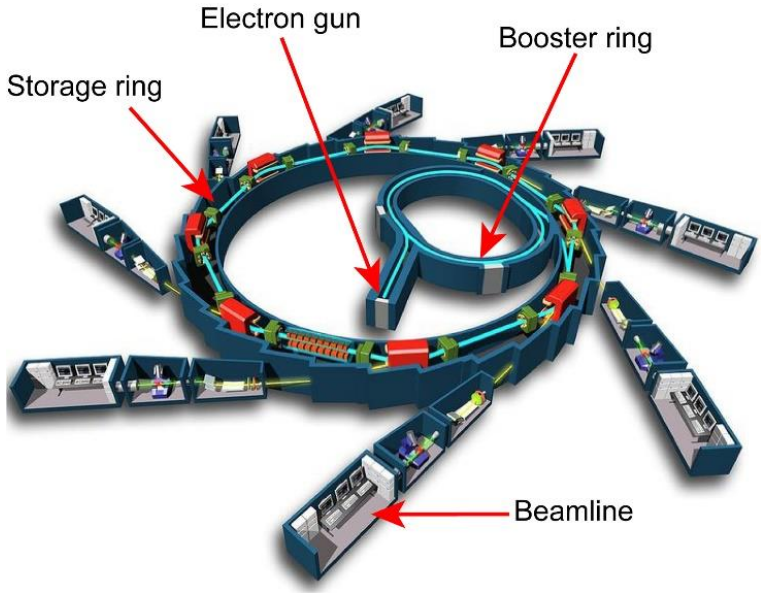

Figure I-16. Diagram of SOLEIL synchrotron radiation facility in France. Source: https://www.synchrotron-soleil.fr/fr/recherche

Figure I-17 shows the NAP-XPS at the TEMPO beamline, which is composed of several chambers, i.e. the load lock, the preparation chamber, the analysis chamber and the catalysis chamber (not shown in Figure I-17). Especially, the analysis chamber is the gold coated mu-

metal chamber which equipped with 7 lines inlets. Five lines are reserved for dosing gases, in which four for pure gases and one for mixed gases. The other two lines are used as dosing liquid like water for example. The sample stage is mounted on a vertical manipulator (the inset of Figure I-17), which is mainly dedicated to catalysis reactions as the sample can be heated up to 1000 ℃ in the atmosphere of the reactive gases (the maximum working pressure 20 mbar) allowing to investigate the in situ catalytic reactions.

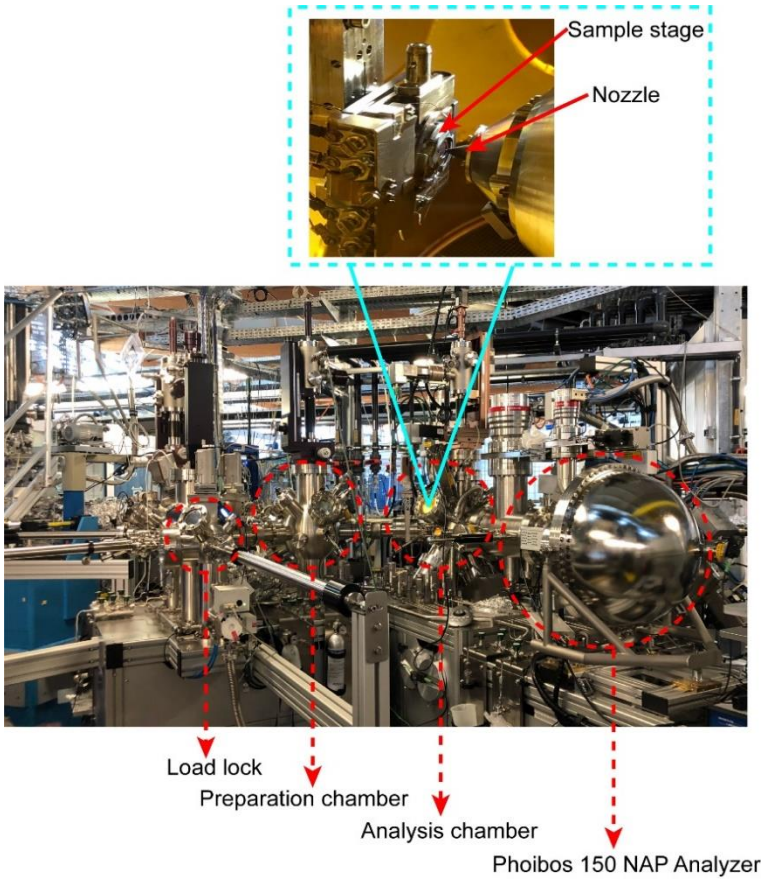

Figure I-17. The NAP-XPS at the TEMPO beamline. Inset is the profile of the sample stage and the nozzle.

The analyzer of the NAP-XPS at the TEMPO beamline is the Phoibos 150 NAP energy hemispherical analyzer (Figure I-18), which has four separate pressure stages separated by small apertures. The first pumping stage (hosting the wide-angle pre-lens) is separated from the analysis chamber by a conically-shaped nozzle pierced with a 0.3 mm diameter hole, which maximizes the differential pumping and brings the pressure in the first pumping stage down to $p_{ch}/10000$, where p_{ch} is the pressure in the analysis chamber. The second stage represents the front part of the electrostatic lenses of the PHOIBOS, separated by an iris aperture from the rear part, the third pumping stage. The fourth and final pumping stage at least work at a pressure of 10^{-7} mbar, which contain the true 180˚ hemispherical energy analyzer with 150 mm mean radius and the 3D delay line detector.

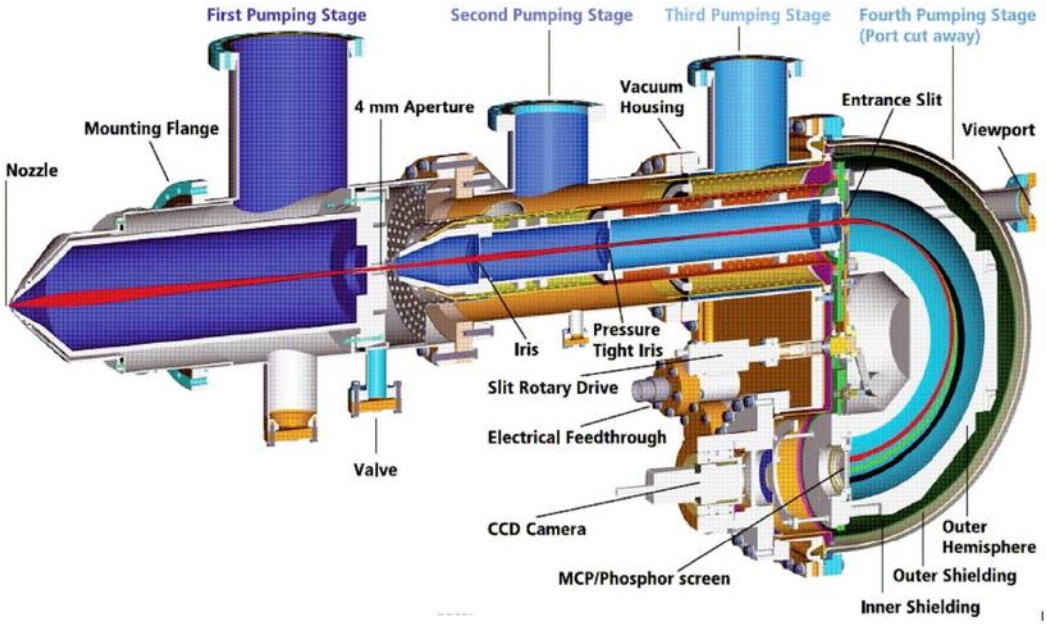

Figure I-18. Diagram of the Phoibos NAP 150 analyzer. Source: http://www.specs.de/cms/upload/PDFs/SPECS_Prospekte/2010_11_PHOIBOS_150_NAP_product_brochure_final_web.pdf

For gas phase spectra, NAP-XPS probes the gas phase layers close to the sample surface within a volume of height approximately 0.12 mm considering the X-ray beam diameter of 0.1 mm and the sample normal/beam angle of 54°. The binding energy of the gas phase core-levels BE_{FL} (gas phase) measured from the Fermi level is used to track changes in the surface work function. The relationship between BE_{FL} (gas phase) and the ionization energy IE_{vac} (gas phase) measured from the vacuum level is:

$$BE_{FL}(gas\ phase) = IE_{vac}(gas\ phase) - \Phi \quad (4)$$

where Φ is the sample work function.[66,67] Therefore, any change in ΔBE_{FL} (gas phase) will lead to a change in the work function ΔΦ equal to:

$$\Delta\Phi = -BE_{FL}(gas\ phase) \quad (5)$$

5. Catalysis

Transition metal nanocatalysts are of paramount interest in the development of efficient and valuable catalytic materials.[68–70] Nevertheless, widespread practical applications are still hindered by the high cost and instability of Pt and of noble metals (NM), on the one hand, and their rather limited life-time due to deactivation phenomena such as sintering and active sites poisoning, on the other hand.[71–74] Therefore, new research strategies are emerging in order to

address these limitations and produce catalysts with enhanced stability.[75–79] In particular, rational design of catalysts and fractional replacement of NMs by a more abundant transition metal provide a suitable method towards this goal. For example, the quantity of Au which is widely used as a catalyst owing to its high activity & selectivity in a large number of important chemical reactions,[80–82] is gradually minimized by the incorporation of Fe and yet its performances are preserved if not improved.[45,77,83] Indeed, the Au- FeO system is highly active for catalyzing low-temperature CO oxidation.[84] The latter reaction, which is relevant for pollutant abatement and for minimizing CO content in water-gas-shift (WGS) hydrogen fuel cells,[7] is also considered as a realistic prototype for understating fundamental concepts in heterogeneous catalysis.[85]

Similarly, Pt is widely used as a catalyst in the composition of both the anode and cathode of proton exchange membrane fuel cells (PEMFC).[74,86,87] In addition to the high cost of Pt, (i) CO poisoning, (ii) decomposition and leaching of Pt and (iii) the rather slow kinetics of the oxygen reduction reaction (ORR) at the cathode are other main issues that degrade and impede the performances of the fuel cells. Recently, Zn has emerged as one of the most prominent element in bimetallic catalysts owing in part to its higher oxophilicity compared with Pt or other TMs and to the stability of its ZnO oxide under reducing conditions.[3,88–90] Additionally, ZnO has remarkable characteristics: (i) a wide gap semi-conductor (3.37 eV), (ii) an accumulation layer at the surface due to the filling of surface states under particular conditions.[91] Therefore, Zn, an affordable metallic material, when combined with Pt or Cu will offer the opportunity to handle these limitations. Indeed, Pt-ZnO is active for CO oxidation[92] and promotes catalytic reactions relevant for fuel cells.[90,93] Cu-based materials are common heterogeneous catalysts used in WGS and preferential oxidation of CO (PROX) reactions relevant for fuel cells.[94–97] Additionally, Cu-ZnO is also an important industrial catalyst for methanol synthesis reactions.[88,97]

One of the major hurdle to the rational design strategies for heterogeneous catalysts is the difficult identifying of the active sites at the metal/oxide, metal/gas and oxide/gas interfaces. The catalysts often undergo structural and surface composition changes under chemical reaction conditions. Thus, determining the active phase, chemical composition and morphology of the catalysts can be achieved ultimately by rational design of NPs followed by their characterization by in situ methods using a combination of microscopy and spectroscopy techniques.

6. Thesis Objectives

The rational design of nanocatalysts and their investigation under their working conditions of pressures and temperatures represent a real strategy towards a realistic understanding of their catalytic reactivity and related issues. Additionally, the reduction of precious metals load in the catalysts while maintaining their optimum performances is essential for large scale practical applications, particularly in the environmentally friendly energy generation systems such as fuel cells. Thus, this project focuses, first on the design of size-selected (~2-5 nm) bimetallic PtZn, (NP) catalysts, including the control of the shape, of chemical compositions, of the nanocristallinity and of the inter-particle distances. These systems, which are considered modern integrated inverse catalysts, offer the advantage of being fully self-sufficient to promote the catalytic reaction where an active support is no longer a prerequisite.

Second, it addresses their reactivity using state-of-the-art, in situ techniques and by comparing surfaces Zn/Pt and ZnPt nanaolloys. This will be achieved through the monitoring of their morphological (size, shape, crystallinity, ordering) and chemical properties (oxidation states, composition, near-surface gas phase, adsorbates and ligands) using real-time Scanning Tunneling Microscopy (STM), Transmission and High Resolution Scanning Electron Microscopy (TEM, FEG-SEM), and Near-Ambient Pressure X-ray Photoemission Spectroscopy (NAP-XPS) operated in environmental conditions (under chemical reaction conditions up to 1 mbar).

For that we will study the the catalytic properties of zinc/platinum surfaces and Zn/Pt nanoalloys in carbon monoxide (CO) oxidation reactions and the preferential oxidation of CO to CO_2. Although the oxidation of CO to CO_2 is one of the simplest reactions of heterogeneous catalysis, it is of both technological and scientific importance. In the environmental field, it is involved, for example, in automobile pollution control, air treatment and clean energy production. From a scientific point of view, CO oxidation is a reference reaction whose intermediate steps (such as the dissociation of gaseous oxygen) are of great interest for many other oxidation reactions. Despite the simplicity of the reaction, a complete view of the role of metal catalysts in CO oxidation is still missing.

Similarly, while chemical states changes in intermetallic NPs in response to the annealing in UHV[75] or to oxidizing and reducing atmospheres[1,9,98] are quite well-studied, their effects on the catalytic properties remain largely elusive. In-situ real-time STM photoemission and X-ray absorption spectroscopy experiments will allow the monitoring of the morphology, chemical

state and composition variations as a function of the treatment (temperature, gas exposure) and ligands. In case of nanoparticles, the characterization would be completed by HR-TEM on material before and under exposure.

Chapter II. ZnO Thin Films on Pt (111): NAP-XPS, STM

1. Introduction

The oxidation of carbon monoxide to carbon dioxide on the surface of metals of the platinum family (Pt, Pd) has been rightly defined by Matera and coworkers as the "fruitfly" of catalytic sciences,[99,100] because of the conceptually simple reaction steps that are involved.[101] For instance, the classical molecular beam work by Ertl and coworkers[102] showed that a Langmuir-Hinshelwood mechanism is at work on the O-covered metallic Pt(111) surface. Although the main picture of surface reactivity may have seemed straightforward, a crucial question quickly emerged, that is, the poisoning of the metallic surface by strongly adsorbed CO molecules, the latter blocking all sites where O_2 could be dissociated.[103,104] Naturally this results in very low oxidation activity. Surface poisoning by CO can be eliminated by raising the temperature, to induce the desorption of adsorbed CO molecules. Taking CO oxidation in O_2 rich O_2:CO mixtures under pressures in the mbar range on Pt(110)[105] or on Pd(100)[106]as an example, very high turnover frequencies (TOF) are reached only above 500 K as CO-free, O-terminated[105,107] metal surfaces (or even surface oxides[101,108]) are formed. In fact, CO poisoning is a severe issue, as the catalyst should work at low temperature, especially when its use in proton-exchange membranes fuel cells is sought for.

To circumvent CO-poisoning at low temperature, a solution could be the separation of the place where CO adsorbs from the place where O_2 adsorbs and dissociates. This simple and elegant idea was the basis of the so-called "inverse catalysts", where 3d transition metal oxide (TMO) islands (where atomic O is produced) cover partly a platinum surface (where CO sticks exclusively).[109–111] This combination is thought to add a new "functionality" to the platinum surface that cope with the technological requirements of low temperature activity, and, as a beneficial consequence, to diminish the load of the precious metal in catalysts. The attention of the researchers focused on the *synergistic effect* that could be observed, *at low temperature,* at the platinum/TMO boundary. [109,111] Indeed the removal of *preadsorbed* CO by a steady-state flux of O_2 (under a pressure in the 10^{-8} mbar range) was observed at room temperature, both for FeO/Pt(111),[109] and NiO/Pt(111),[110] which is naturally impossible on the pure Pt(111). It was shown in Ref.[109] that the reactivity increases with the TMO/Pt boundary length per surface unit, which supports the idea that the reaction takes place at the phase boundary. Further theoretical calculations by Su et al.[111] addressed a series of 3d TMOs and showed that the key reaction site is a coordinatively unsaturated metal cation combined to a nearby platinum atom.

Besides the TMO oxides (FeO and NiO) that were known experimentally to be efficient when combined with Pt(111), Sun et al.,[111] also explored theoretically the reactivity of a *filled* 3d band transition metals oxide ZnO. When compared with pure Pt(111), the Pt- Zn^{2+} ensemble favors the breaking of the O-O bond at the boundary and lowers the barrier for CO oxidation by about 0.4 eV. While the Pt- Fe^{2+} ensemble presents a lower CO oxidation activation barrier than the Pt- Zn^{2+} one, the single oxidation state of Zn (2+) is a tremendous advantage with respect to the former case, because ferrous oxide can become ferric oxide under oxygen rich conditions, which is highly detrimental to its efficiency.[111] Therefore theoretical predictions makes the ZnO/Pt(111) system worthy of interest, especially in oxygen-rich CO/O_2 mixtures.

At the time of publication of Ref. [111] there was no experimental data yet available on CO oxidation on the ZnO/platinum system. The first announcement of synergistic effect for a discontinuous *submonolayer* ZnO films supported by Pt(111) was made a year after by Martynova and coworkers.[112] Apparently no experiment was carried out by the Berlin group at room temperature, where synergistic effects were already observed for the "benchmark" FeO(111)/Pt(111) system.[109] However, *at a temperature of 450 K* and for an oxygen-rich O_2:CO mixture (50 mbar:10 mbar, He balance to 1 bar) the CO_2 production rate measured at the outlet of the reaction chamber was found to be circa one order of magnitude higher on films of partial ZnO coverage than on bare Pt(111). Indeed at this temperature the pure Pt(111) surface may still be CO poisoned. A technique like near-ambient pressure photoemission spectroscopy (NAP-XPS) indicates that in oxygen-rich mixtures the transition between CO-Pt(111) to O-Pt(111) occurs in the 515-535 K range, according to Knudsen et al..[113] Therefore, the activation of the Pt-Zn^{2+} sites can be effective at 450 K for CO oxidation.

Given the promises of the ZnO/Pt(111) system in low temperature CO oxidation, further studies need to be performed, focusing on several issues that were not addressed in the pioneering work of Martynova et al..[112] First, instead of a single temperature (450 K), CO oxidation should be examined in a wide range of temperature, from room temperature, where the added value of "inverse" catalysis is major due to the poisoning of Pt by CO, to the high temperature regime (above ~520 K) where Pt itself is, beyond any doubt, the most reactive phase[107] (the reaction probability is close to one[102] when CO has desorbed from Pt areas). Second, we need to collect information on the chemical species present at the ZnO/Pt(111) surface when it is exposed to the O_2: CO mixture, as the preceding work by Martynova et al.[112] was based on gas composition measurements (at the chamber outlet) and "post-mortem"[112] STM observation of the surfaces.

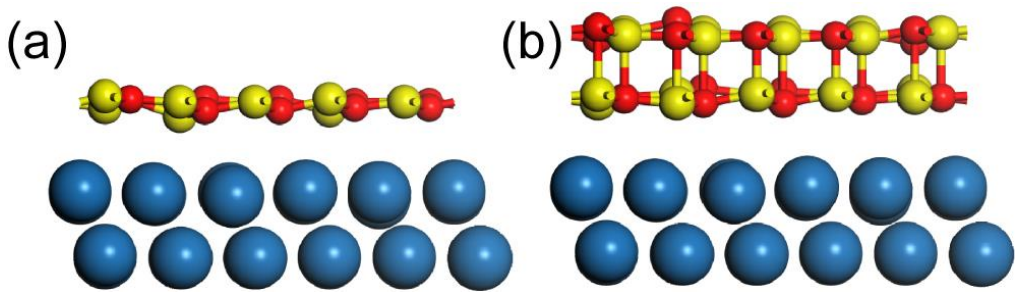

Figure II-1. Schematics of the side view (a) mono- and (b) bilayer- ZnO film on Pt(111). Pt atoms are shown in blue, whereas Zn and O atoms are in yellow and red, respectively.

We have realized this program using *in-situ* near ambient pressure X-ray photoelectron spectroscopy (NAP-XPS), an efficient spectroscopic tool to monitor catalytic reactions in operando conditions.[12,13,106,114,115] The CO oxidation experiments were carried out within a temperature range of 293-520 K and in an O_2 rich O_2:CO mixture (4:1), under a total pressure of 1 mbar. NAP-XPS provides a "synoptic view" of both the catalytic surface and the gas phase in the immediate vicinity of the surface, as the solid-state core-levels are, at least in the present case, well separated from those of the gas-phase reagents and products. Moreover, a mass spectrometer, embedded in the NAP-XPS spectrometer, provides additional information on the gas phase composition in the vicinity of the surface that can be cross-checked with gas phase XPS data.

As in our previous work on ZnPt nanoparticles on TiO_2,[66] where each metal and their combination were studied separately in the same conditions of pressure and temperature, it seemed crucial to us to carry out a comparative study of the reactivity of the "plain" Pt(111) surface and of the surface of Pt(111) partially covered by a monoatomic layer of ZnO (denoted ZnO/Pt(111) in the following). Mono- and bi-layers of ZnO on Pt(111),[116,117] Pd(111)[118] and coinage metals[119–122] abandon the wurtzite structure of the bulk phase for a planar one similar to *h*-BN or graphene (Fig. II-1). First a direct comparison of the XPS core-level spectra allowed us to see immediately what "extra" species were present on the ZnO/Pt(111) surface. Second, given that identical temperatures and pressures were used in both cases, platinum areal fractions could be determined for ZnO/Pt(111) by a simple CO-titration method. Third, this comparative approach should, in principle, put us in a position to determine which of the two surfaces is the most reactive. Indeed NAP-XPS results combined with mass spectrometry are often used to make such verdicts when an alloyed Pt surface (for instance Pt-Re[123]) is compared to plain Pt(111). Indeed, the only "observable" we have at hand to discuss the respective reaction rates on plain Pt(111) and ZnO/Pt(111) is the CO_2 partial pressure above the catalytic surface.

However, previous planar laser induced fluorescence (PLIF) experiments[100,124–126] warned us about the formation of a CO_2 –rich boundary layer (through which the minority reagent CO diffuses). Therefore, chemistry, i.e. the intrinsic turnover frequencies (TOF), is hard to disentangle from physics, i.e. mass transfer limitation (MTL), without any theoretical support.[99,100,127,128] The comparison of CO_2 pressures reached above the Pt(111) and ZnO/Pt(111) surfaces in identical operando conditions, the latter one being only partially covered by ZnO (60 to 70% of the total area) is a further asset to discuss the question of the occurrence of MTL.

The results of this operando NAP-XPS study are presented as follows. First, we show the gas phase molar fractions deduced from mass spectroscopy and when possible, we compare them to gas phase NAP-XPS data. This allows us to start a discussion on the relative reactivity of plain Pt(111) and ZnO/Pt(111), taking into account the MTL issue. After determining the stationary conditions, we can discuss changes in the NAP-XPS core-levels that are relative to the solid phase. We examine the surface chemistry of the plain Pt(111) surface at the various heating stages, which then gives us a straightforward way to highlight the chemical specificity of the inverse ZnO/Pt(111) model catalyst and to calibrate the surface density of the chemical species present on its surface. Finally, with the help of additional STM images, we start a discussion on the appearance of species at the Pt/ZnO boundary and of their function in the catalytic process.

2. Experimental Methods

Preparation of ZnO thin film on Pt(111). A clean Pt(111) surface was obtained by cycles of Ar^+-sputtering and annealing in UHV to 1200K. After which, the metallic Zn was deposited under O_2 at RT onto Pt(111) surface followed by postoxidation annealing at 600K. The deposition under O_2 must be conducted so that the PtZn intermixing at the interface is minimized.

The NAP-XPS setup as a flow reactor. The experiments were performed at TEMPO beamline, SOLEIL synchrotron (Saint-Aubin, France) with the NAP-XPS setup managed by the LCPMR group (Sorbonne Université). The maximum pressure attainable in the analysis chamber is 20 mbar. The X-ray beam is introduced into this chamber using a differentially pumped windowless beam entrance designed by SPECS. The direction of the X-ray beam (diameter of 0.1 mm) makes an angle of 54° with the sample normal. The NAP-XPS analyzer itself (a SPECS PHOIBOS 150 NAP analyzer[129]) is composed of four separate pressure stages separated by

apertures. The first pumping stage (hosting the wide-angle pre-lens) is separated from the analytic chamber by a conically-shaped nozzle pierced with a 0.3 mm diameter hole, which maximizes the differential pumping and brings the pressure in the first pumping stage down to $p_{ch}/10000$, where p_{ch} is the pressure in the analysis chamber.[129] This second stage represents the front part of the electrostatic lenses of the PHOIBOS, separated by an iris aperture from the rear part, the third pumping stage. The fourth and final pumping stage contains the hemispheres and detector. A quadrupole mass spectrometer (QMS) is installed in the second pumping stage, allowing the continuous monitoring the gas phase composition sampled from the gases of the analysis chamber. The QMS signal is converted into mbar by normalizing the CO and O_2 signal to the known initial partial pressures, and the CO_2 signal is scaled to match the observed conversion of CO. The CO partial pressure is corrected from the cracking pattern contribution of CO_2.

During the 6-hour experiment for each temperature, an O_2:CO mixture is fed into the chamber with a CO molar fraction at the inlet f_{in}^{CO} equal to 0.20. The overall pressure is kept constant at p_{ch}~1 mbar by feeding the analysis chamber via a leak valve, to compensate the diminishing number of molecules due to the *pumping* through the analyzer nozzle and the beamline entrance and to the reaction $2CO + O_2 \rightarrow 2CO_2$ that diminishes the number of molecules. Therefore, one can consider that the analysis chamber/NAP-XPS ensemble is a special case of a flow reactor, where pumping is realized via the NAP-XPS nozzle and the beamline entrance. To limit the attenuation of the photoelectron signal by inelastic scattering in the gas phase,[12] the nozzle is placed at distance d of 1.5 mm from the sample surface. Under a total pressure of 1 mbar, the molecule mean free path λ_m is ~0.05 mm, the gas flow regime is nearly attained, the Knudsen number λ_m/d being ~0.03.[12] The molar flow rate F_{out} through a pinhole of area A can be calculated from the flow rate of a gas at choked conditions.[12,130] Expressed in mol×s^{-1} F_{out} is:

$$F_{out} = \frac{A \times C_d \times p_{ch}}{\sqrt{MRT}} \gamma^{\frac{1}{2}} \left(\frac{2}{\gamma+1}\right)^{\frac{\gamma+1}{2\gamma-2}} = 0.417 \times A \times \frac{p_{ch}}{\sqrt{MRT}},$$

where C_d is the coefficient of discharge (~0.61 for an orifice plate), γ the adiabatic index (1.4 for the diatomics, and 1.28 for CO_2), R the gas constant and T the absolute temperature.

At room temperature, under a pressure of 1 mbar, and for an aperture of 7.07×10^{-8} m^2 (the nozzle pinhole area), F_{out} is equal to 3.3×10^{-7}, 3.5×10^{-7} and 4.47×10^{-7} mol.s^{-1}, for O_2 and CO and CO_2 respectively. As the capillary through which the X-ray beam is introduced has also a diameter of 0.3 mm, its contribution to the molar flow rate is equal to that of the nozzle.

Therefore, for the inlet gas composition (80% O_2 and 20 % CO) at room temperature the estimated total average molar flow rate F_{out} is 6.7×10^{-7} mol.s^{-1} (0.9 mL$_n$/min). Considering the volume of the chamber (35 L), the transit time (the gas exchange rate) τ_{tr} $(1/\tau_{tr})$ is 35 min ($2.8\ 10^{-2}$ min^{-1}). These numbers are useful when comparison are made with other AP-XPS systems.[126,113]

The comparison of the flow and pressure conditions with other experiments is of great importance. Zhou et al.[126] have built a PLIF analysis chamber pumped only via a nozzle with a geometry similar to that of NAP-XPS measurements (aperture 1 mm, nozzle-to-surface distance of 2 mm inserted in a reaction chamber of volume 23 mL). They aimed at studying the impact of pressure and gas exchange rate on the shape of the CO_2-rich boundary layer that forms above a Pd(100) surface when the reactivity is high (see below). The minimum working pressure they used was 25 mbar (partial pressures of 1.25 mbar CO, 1.25 mbar O_2 and 22.5 mbar Ar), with a total flow of 10 mL$_n$/min. Therefore, in the present conditions, the total pressure and the flow rates are about one order of magnitude smaller than those used in Ref. [126].

The concept of the reactor used by Martynova et al. is still different. It consists in a ~30 ml high-pressure cell[131] in which the crystal surface is exposed to the gas mixture, consisting of 10 mbar CO and 50 mbar O_2 balanced with He to 1 bar (similar to the PLIF experiments). The velocity was about 3 ml min^{-1}. The gas phase composition is examined at the outlet of the high-pressure cell, using gas chromatography, and then recycled into the reactor. The reactor apparently functions as a batch reactor, as Martynova et al.[112,131] measure CO_2 partial pressure increasing linearly with time, that is to say, initial reaction rates (given in arbitrary units, no absolute TOF is indicated), are obtained while we measure steady-state CO_2 partial pressures. As there is no spectroscopic tool in the vicinity of the platinum single crystal they use, Martynova and coworkers do not address the question of MTL or other hydrodynamic effects, as at high reaction rates, they may have an impact on the partial pressures at the outlet.[99] The question may be of no importance, as the reaction rates may be small at the working temperature they used (see below).

NAP-XPS spectroscopy probes the gas phase layers *close to the sample surface* within a volume of height approximately 0.12 mm considering the X-ray beam diameter of 0.1 mm and the sample normal/beam angle of 54°. The binding energy of the gas phase core-levels BE_{FL}(gas-phase) measured from the Fermi level is used to track changes in the surface work

function. The relationship between BE_{FL}(gas-phase) and the ionization energy IE_{vac}(gas-phase) measured from the vacuum level is:

$$BE_{FL}(\text{gas-phase}) = IE_{vac}(\text{gas-phase}) - \Phi$$

where Φ is the sample work function.[67,66] Therefore any change in ΔBE_{FL}(gas-phase) will lead to a change in the work function $\Delta\Phi$ equal to:

$$\Delta\Phi = -\Delta BE_{FL}(\text{gas-phase})$$

The STM data were acquired using a variable temperature XA microscope from Omicron NanoTechnology. The base pressure in the STM chamber prior to gas exposure was better than 3×10^{-11} mbar. The W tip was cleaned by flash heating, via direct current annealing in the UHV system prior to its use.

3. Results and Discussion

The gas phase. In Fig. II-2, we show the time-dependence of the QMS molar fractions for CO (f_{QMS}^{CO}), O_2 ($f_{QMS}^{O_2}$), and CO_2 ($f_{QMS}^{CO_2}$) for Pt(111) (panel (a)) and ZnO/Pt(111) (panel (b)). In panels (c) and (d) the QMS CO_2 molar fractions of both surfaces are given on a logarithmic y-scale to highlight the reaction starting at 293 K. Fig. II-2 shows that the QMS molar fractions are sensitive to the successive temperature increases. Transients that can last ~100 min are followed by steady states. The response of the ZnO/Pt(111) surface is very similar, if not identical to that of the reference Pt(111) surface. Three different regimes can be highlighted. The low temperature regime (Regime I, from RT to 410 K), the high temperature range (Regime III, from 485 to 520 K), and, in between, the intermediate regime (Regime II, from 445 to 465 K).

In Regime I (at 410 K), the steady-state values of the molar fraction $f_{QMS}^{CO_2}$= 0.0074 for Pt(111) ($p_{QMS}^{CO_2}$= 7 10^{-3} mbar) and 0.011 for ZnO/Pt(111) ($p_{QMS}^{CO_2}$ =10^{-2} mbar). The 30% deviation in the $p_{QMS}^{CO_2}$ signal is indicative that the ZnO/Pt(111) surface is more reactive than the Pt(111) one at this temperature. Note that the very low partial pressures of CO_2 make it undetectable in the gas phase O 1s spectra of Pt(111) (Fig. II-3) and ZnO/Pt(111) (Fig. II-4).

In Regime II, the steady-state CO_2 partial pressures above the Pt(111) surface increase by about one order of magnitude with respect to Regime I (Fig. II-2a). When the surface temperature is raised to 445 K, $f_{QMS}^{CO_2}$ $reaches$ 0.072 ($p_{QMS}^{CO_2}$= 0.07 mbar) for Pt(111) after a long transient. Interestingly, when the surface temperatures is raised to 465 K, we do not observe a strong

enhancement in $f_{QMS}^{CO_2}$. Instead, the molar fraction of the product $f_{QMS}^{CO_2}$ reaches a plateau at 0.09 ($p_{QMS}^{CO_2}$~0.09 mbar). In the gas layer comprised between the surface and the NAP-XPS nozzle, CO_2 starts to accumulate, but CO is far from being fully depleted. Indeed, the steady-state values of f_{QMS}^{CO} at 445 and 465 K, are 0.13 and 0.115, respectively, that is about half the molar fraction in the gas mixture fed into the gas chamber (0.2). We can make exactly the same kind of observations for ZnO/Pt(111), Fig. II-2b. The steady-state $f_{QMS}^{CO_2}$ (f_{QMS}^{CO}) values are 0.08 (0.12) and 0.09 (0.11) at 445 K and 465 K, respectively.

For both surfaces, Regime III is characterized by a complete depletion of CO above the sample surface after a transient of 92 min for Pt(111) and 155 min for ZnO/Pt(111) at 485 K. P_{QMS}^{CO} is not measurable, after the due correction of the CO_2 contribution to mass 28, and absent from C 1s and O 1s NAP-XPS spectra, see Fig. II-3 and II-4. When the steady state is reached in the final part of the 485 K heating step, $f_{QMS}^{CO_2}$ is ~0.22 (0.22 mbar) *for both surfaces* and does not vary when the temperature increases to 520 K.

The QMS data lead to two main observations. Within Regime II (where the CO pressure is divided by a factor of 2 or so) or within Regime III (where the CO pressure is almost zero), changes in temperature, and thus in the activated surface reaction rate, have no effect on $f_{QMS}^{CO_2}$. Such observations suggest that a relationship between the intrinsic production rate of CO_2 (the turnover frequency) and the steady-state value of $f_{QMS}^{CO_2}$ measured at the sample surface is lost. Indeed, the reaction rate is equal to the product concentration divided by a transit (or residence time) in the flow regime only for *perfectly mixed* reactors (which is not the case here), and, of course, at low pressure in the free molecular regime.[132] Second, in Regime II and III we see no difference in the steady-state value of $f_{QMS}^{CO_2}$ between pure Pt(111) and ZnO/Pt(111). Especially at high temperature (Regime III), one should expect a higher reaction rate for Pt(111) than for ZnO/Pt(111), for which the surface is made of Pt and ZnO mesoscopic areas (the ZnO layer de-wets, see below), the platinum patches being much more reactive (NAP-XPS shows that CO leaves the platinum patches) than the ZnO ones. These two observations suggest that mass transport limitation (MTL) is already effective in Regime II, leading to partial CO-depletion and CO_2-accumulation at the surface. In contrast, in Regime I (RT to 410 K), when $f_{QMS}^{CO_2}$ is one order of magnitude smaller than the partial pressures of the reagents, i.e. the boundary layer is not saturated, we find that the steady-state value of $f_{QMS}^{CO_2}$ is different for both surfaces (higher for ZnO/Pt(111) than for Pt(111)), in line with the findings of Martynova et al..[112]

What is the spatial extent of the boundary layer? In our case, the gas phase is probed either by NAP-XPS in a volume of height 0.12 mm above the surface (See Experimental Details), and through gas sampling by QMS through the analyzer nozzle, at 1.5 mm above the surface. We have calculated the CO_2 molar fractions $f_{NAP-XPS}^{CO_2}$ from the intensities of the gas phase XPS O 1s components of CO_2, of the $^2\Sigma$ $^4\Sigma$ O_2 doublet, and of the CO, whose energy positions are indicated in Fig. II-3 (Pt(111)) and II-4 (ZnO/Pt(111)). The $f_{NAP-XPS}^{CO_2}$ values are reported in Fig. II-2a and II-2b. The agreement between $f_{NAP-XPS}^{CO_2}$ and $f_{NAP-XPS}^{CO_2}$ is qualitatively good in measuring the gas phase spectral weights. This means that the CO-depleted (CO_2-accumulated) volume has an extension comparable or even greater than the surface-nozzle gap. The extension

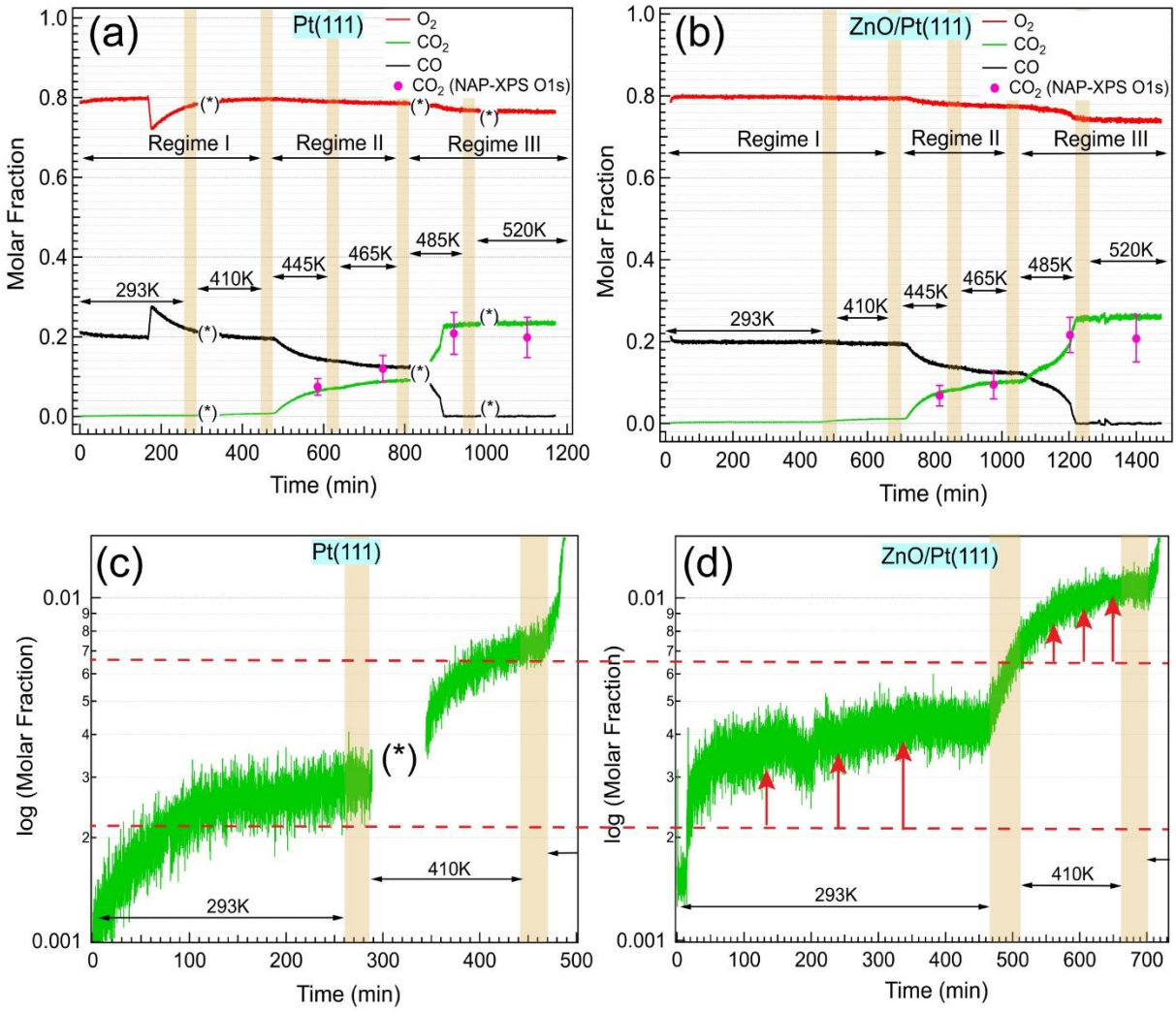

Figure II-2. Time evolution of the QMS molar fractions of CO (f_{QMS}^{CO}), O_2 ($f_{QMS}^{O_2}$) and CO_2 ($f_{QMS}^{CO_2}$) for the four heating steps (293 K, 445 K, 465 K, 485 K, and 520 K) for (a) the Pt(111) surface, (b) the ZnO/Pt(111) surface. Pink filled disks in (a) and (b) are CO_2 molar fractions $f_{NAP-XPS}^{CO_2}$ deduced from gas phase O 1s spectra (Regime II and III). In Panels (c) and (d) we compare the $f_{QMS}^{CO_2}$ values of Pt(111) and ZnO/Pt(111) at low temperature (y-logarithmic plot) for the regimes I and II. The experiment is performed under a total pressure of 1 mbar. In panel (a) the deviation of the molar fractions from the nominal values observed at 293 K is due to a temporary malfunction of the flowmeter. The vertical arrows indicate the higher molar fraction of CO_2 production measured on ZnO/Pt(111) compared with that of pure Pt(111). (*) this symbol indicates a momentary interruption of the QMS data acquisition.

of the CO_2-rich "boundary layer" over a catalytic crystal surface is a question that has been addressed carefully by PLIF in several papers,[100,125,126] including one in which the NAP-XPS geometry is reproduced.[126] In the latter work the boundary layers extension is a few mm, i.e. a value comparable to the sample-nozzle gap. However, in the present experiment the much smaller mass flow (one order of magnitude smaller) and above all the much lower overall pressure (was used in Ref.[126] to balance the overall pressure to 1 bar) should lead to much larger extensions of the boundary layer (in the limit of very low pressures, the CO_2 boundary layers extends in the whole reaction vessel).

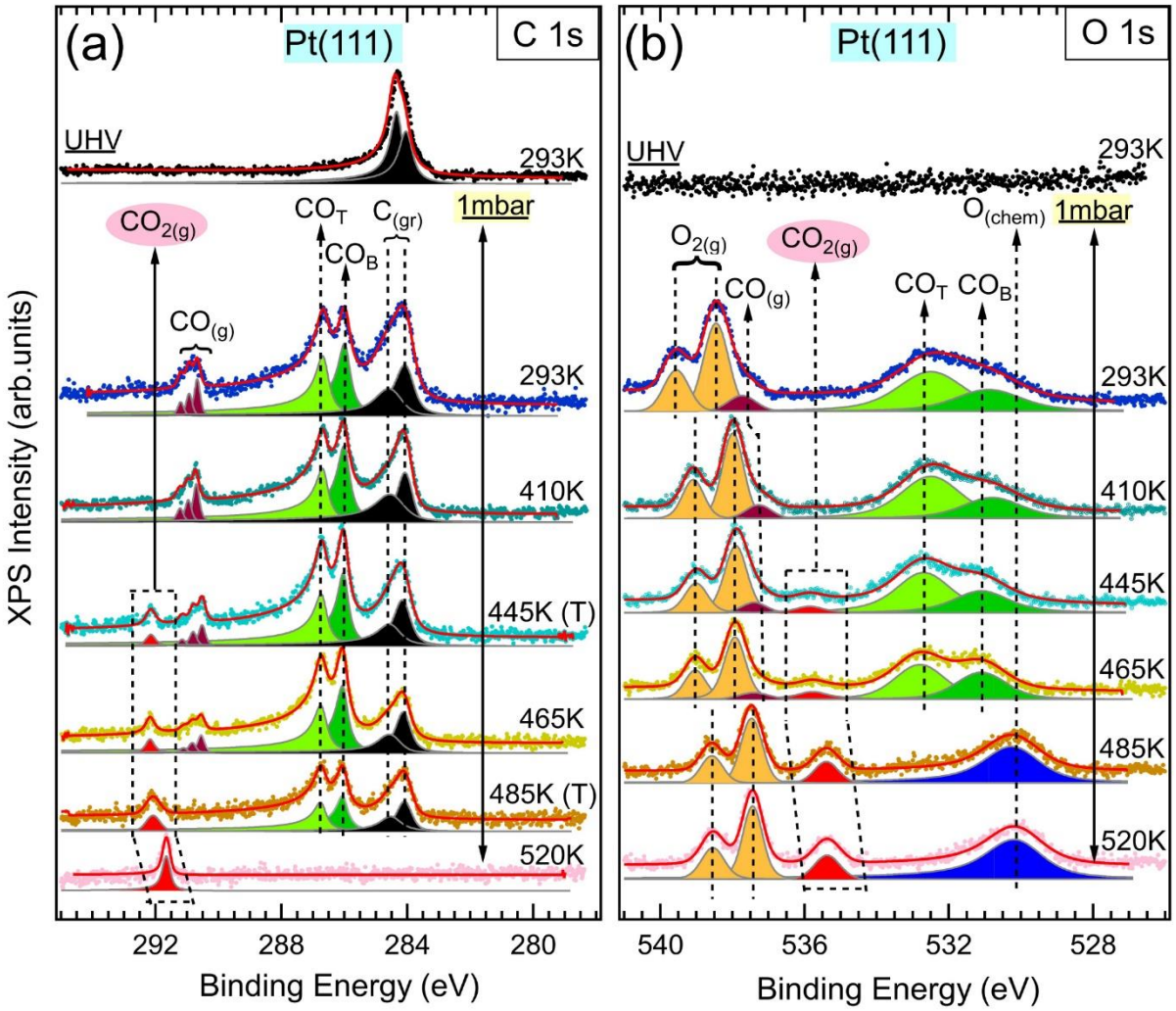

Figure II-3. (a) C1s (measured at hv = 400 eV), and (b) O1s (measured at hv = 635 eV) core-level spectra of the Pt(111) sample. (T) indicates that the spectra were measured in a transient state (when steady state conditions were not reached yet). The spectra labeled UHV were measured at room temperature, before any exposure to gases. The other spectra are recorded under a nominal pressure of 1 mbar, with an O_2 :CO ratio of 4:1 (oxygen rich mixture). Gas-phase components are denoted by the "g" index, their positions are sensitive to changes in the surface work function. In C 1s and O 1s spectra adsorbed CO exhibits two components corresponding to two adsorption geometries on Pt(111), the bridge position noted COB and on-top position noted COT. Form and Carbx* are adsorbed formates and carboxyls species. The components C(gr) and O(chem) are attributed to graphitic carbon and chemisorbed oxygen, respectively.*

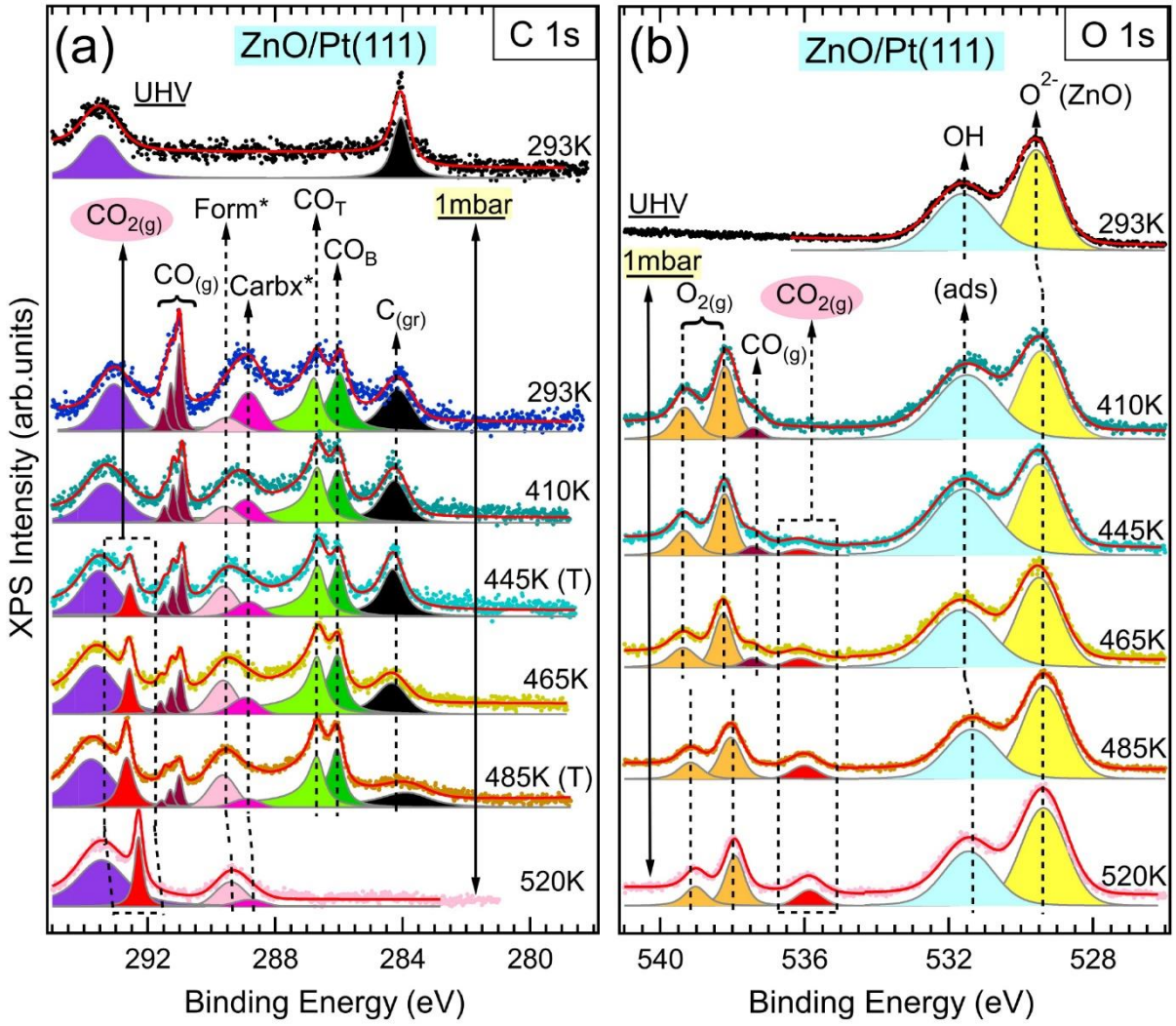

Figure II-4. (a) C1s (measured at hν = 400 eV), and (b) O1s (measured at hν = 635 eV) core-level spectra of the ZnO/Pt(111) sample. (T) indicates that the spectra were measured in a transient state (when steady state conditions were not reached yet). The spectra labeled UHV were measured at room temperature, before any exposure to gases. The other spectra are recorded under a nominal pressure of 1 mbar, with an O_2 :CO ratio of 4:1 (oxygen rich mixture). Gas-phase components are denoted by the "g" index, their positions are sensitive to changes in the surface work function. In C 1s and O 1s spectra adsorbed CO exhibits two components corresponding to two adsorption geometries on Pt(111) (areas left free), the bridge position noted COB and on-top position noted COT. In C 1s, Form and Carbx* are adsorbed formates and carboxyls species. The components C(gr) and O(chem) are attributed to graphitic carbon and chemisorbed oxygen, respectively. In the O 1s spectra the O^{2-} and OH components are the oxygen components of ZnO and of its hydroxide, respectively. In O 1s, the components (noted ads) of the adsorbed CO and of the chemisorbed O of the platinum areas are hidden in the O^{2-} and OH peaks. The violet peak is due to K 2p impurity.*

The plain Pt(111) surface as a reference. We first consider the reference sample, the bare platinum Pt(111) surface, whose corresponding C 1s, O 1s and Pt 4f spectra are given in Fig. II-3, and II-5a, respectively. The UHV C 1s XPS spectrum (Fig. II-3a) taken at room temperature after surface cleaning presents a graphitic contamination at a binding energy (BE_{FL}) of 384.1 eV, but no oxygen contamination is detected in the O 1s spectrum (Fig. II-3b),

and a clear Pt surface component (Pt 4f $_{7/2}$) appears at 70.8 eV to the right of the bulk component (at 71.1 eV) (Fig. II-5a).

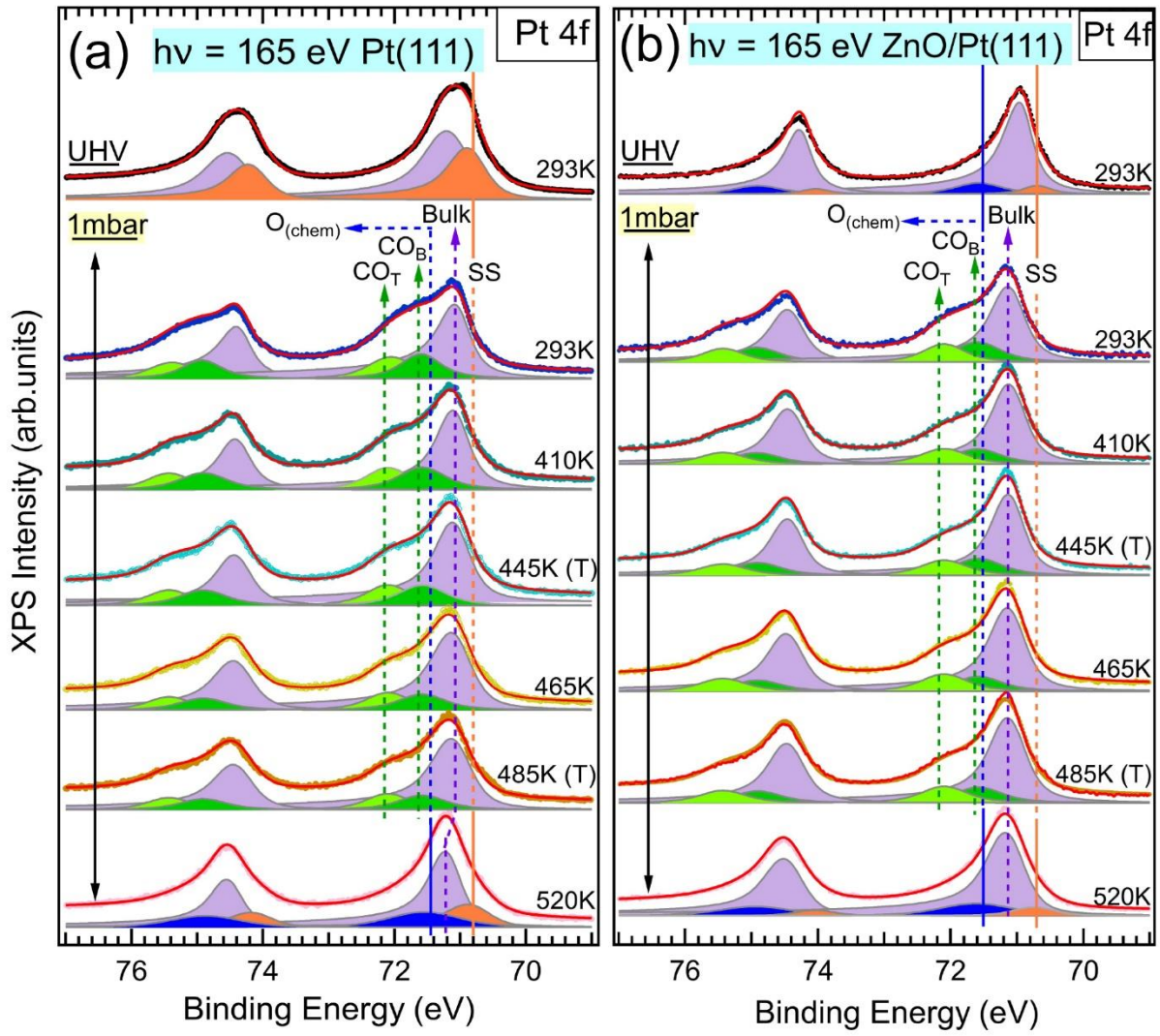

Figure II-5. Pt 4f core-level spectra of Pt(111) (a) and of ZnO/Pt(111) (b). SS are surface states corresponding to Pt atoms on the topmost surface of Pt(111). (T) indicates that the spectra were measured in a transient state (when steady state conditions were not reached yet). COB and COT are the contributions of adsorbed CO on two geometries of the Pt(111) areas, bridge and on-top, respectively. O(chem) is the contribution of chemisorbed oxygen on Pt(111).

Once the 1 mbar CO:O_2 mixture is introduced at room temperature, two new C 1s components appear, one at a BE_{FL} of 286.0 eV (attributed to "bridge" adsorbed CO, noted CO_B) and one at 286.7 eV (attributed to "on-top" CO, noted CO_T).[133] The "on-top": "bridge" ratio is~0.8. The appearance of these two adsorption geometries is corroborated by that of two components of the O 1s spectrum (Fig. II-3b) at 530.9 eV (bridge) and 532.5 eV (on-top). [133] As observed by others,[134] the on-top:bridge ratio of 1.9 is different from that found from the C 1s spectra, but the discrepancy may be attributed to photoelectron diffraction effects. Note that in the O 1s spectrum, there is no measurable component attributable to chemisorbed oxygen, that should

give a distinctive peak at ~ 530 eV.[133] Thus, despite the exposure to a CO/O_2 mixture, only CO bonds to the surface at room temperature. This suggests that CO coverage is close to saturation, between 0.6 ML[133] and 0.68 ML[134]. The Pt 4f spectrum measured in surface sensitive conditions (kinetic energy of $4f_{7/2}$ electrons ~94 eV) confirms the presence of a CO overlayer at room temperature, as the surface component has vanished, and two new peaks have appeared at higher binding energy than the bulk metallic $4f_{7/2}$ peak, at 72.1 eV and 71.6 eV attributable to Pt making bonds with on-top and bridge CO, respectively.[133] The surface states were consumed after exposure.

As discussed before, CO_2 is detected by QMS in Regime I at 410 K, corresponding to $P_{QMS}^{CO_2}$ of ~7×10^{-3} mbar, but its component is not yet visible in the C 1s spectrum. The Pt(111) surface remains poisoned, as demonstrated by the observation of the adsorbed CO components in the C1s (Fig. II-3a) and O 1s (Fig. II-3b) spectra and of the Pt-CO bond components in the Pt 4f spectrum (Fig. II-5a). However, the normalized adsorbed CO intensity parameter $R_{C1s}^{CO}(T)$ shown in Fig. S1 (where $R_{C1s}^{CO}(T) = \frac{I_{C\,1s\,NAP-XPS}^{COads}(T)}{I_{C\,1s\,NAP-XPS}^{COgas}(T)} \times p_{QMS}^{CO}(T)$) estimated from gas-phase and adsorbed CO XPS intensities and corrected from variation of P_{QMS}^{CO} (see SI, Table S1 and Fig. S1) indicates that the CO coverage is now 90% of that at room temperature.

As discussed before, in Regime II, at 465 K (see Fig. II-2a), $p_{QMS}^{CO_2}$ reaches a plateau at 0.09 mbar, greater by an order of magnitude than the CO_2 partial pressure in Regime I. CO is not fully depleted in the gas layers above the surface(P_{QMS}^{CO} is one half of the nominal value of the mixture) and is still found adsorbed on the surface (Fig. II-3). This view is corroborated by the analysis of the Pt 4f spectra (Fig. II-5a) where the characteristic binding energy shifts of the Pt-CO bonds are observed. The CO coverage (see $R_{C1s}^{CO}(T)$ in Fig. S1), has diminished as it is now 74% of that found at room temperature. As the on-top: bridge ratio in the C 1s and O 1s spectra increases with respect to that observed at room temperature, it is possible that bridge sites are depopulated. Despite the surface loses CO adsorbates, the O 1s component related to chemisorbed oxygen that should appear at ~530.1 eV[133] in Fig. II-3b is not yet detectable. The C 1s (O 1s) BE_{FL} (gas-phase) of CO and the O 1s BE_{FL} (gas-phase) of O_2 ($^2\Sigma$) remain rather constant between room temperature and 396 K, at 290.6 ± 0.1 eV and 539.05 ± 0.05 eV, respectively. Therefore, the partial desorption of adsorbed CO has a small impact on the work function. The work function changes between the CO-covered surface (high coverage) and the clean one is extremely small (+15 meV).[135] The O 1s spectrum and the work function variation

do not advocate the formation of sizeable oxidized areas coexisting with CO-covered areas. Therefore, the first MTL regime is reached (with a partial pressure of CO equal to half the nominal pressure) while CO is the largely dominant surface species.

The situation is completely different in Regime III, that starts at the end of the 485 K (the O 1s spectrum displayed in Fig. II-3b pertains to this steady state). Then, CO is fully depleted from the gas layers above the sample, as the CO_2 boundary layer has fully developed. Concomitantly, the components of adsorbed CO have disappeared from the C 1s (Fig. II-3a) and O 1s (Fig. II-3b) spectra. Instead, the O 1s component attributed to chemisorbed atomic oxygen[133] appears at 530.1 eV (see $O_{(chem)}$ component in Fig. II-3b). The latter behavior was also observed by authors using NAP-XPS in the study of CO oxidation with large O_2:CO ratios (9:1, under 0.15 mbar).[136] Passing from Regime II to Regime III, a new interesting observation is that of a change in the gas-phase binding energies. We measure a. ΔBE_{FL}(gas-phase) of -0.45 eV from CO_2 C 1s and of -0.48 eV from O_2 O 1s. Therefore, the replacement of a CO-covered surface by an O-covered one is accompanied by a *positive increase* of the work function by $+0.5$ eV. This behavior is quite the opposite to that of the Pd(110) surface whose work function *diminishes* ($\Delta\Phi \approx -0.5$ eV) when the surface shifts from CO-covered to O-rich (see the supporting information of Ref. [137]). In the latter case a surface oxide develops at the surface. *The present observation may be a useful piece of evidence in the ongoing debate about the presence of active platinum oxide phases on top of platinum surfaces.*[101]

What's new with the surface of the inverse metal-oxide, ZnO/Pt(111), model catalysts? As previously discussed, the CO_2 pressure plateaus on bare and ZnO covered Pt(111) are practically identical from a temperature of 445 K as, MTL, leading to CO depletion in the gas overlayers, determines the steady states for both surfaces. However, in Regime I, at 410 K, the reactivity is low and MTL is not yet a limiting step. In this range the ZnO/Pt(111) is more active than the bare Pt(111) one (the CO_2 partial pressure is ~30% higher). Therefore, in this context, an examination of the surface chemistry of the ZnO/Pt(111) is all the more interesting, in this regime, as this point was not addressed in the previous work by Martynova *et al.*.[112]

At room temperature and in UHV conditions, the C 1s spectrum (Fig. II-4a) of the as-prepared sample presents a graphitic contribution at ~284 eV, similar to the reference Pt(111) surface. Note also the presence of a K 2p component resulting from the ZnO deposition process (absent in the UHV spectrum of the reference plain platinum surface, Fig. II-3a). The corresponding O

1s spectrum (Fig. II-4b) exhibits two components related to the zinc oxide layer. The one at lower binding energy, 529.5 eV, matches that of O^{2-} in bulk ZnO.[138] It corresponds to 57% of the spectral weight. The second one (43% of the spectral weight), found at higher binding energy, 531.7 eV, is attributed to hydroxyls HO^{-},[139] stabilizing the ZnO layers. Indeed, Pt(111),[116,117] like Pd(111),[118] is able to decompose residual H_2 or H_2O. While hydroxyls were previously detected by IRAS spectroscopy on this system,[117] NAP-XPS has the advantage of quantifying their distribution.

When the gas mixture is introduced at room temperature, the C 1s spectrum (Fig. II-4a) exhibits the two characteristic components of CO adsorbed on Pt(111) at binding energies of 286.6 eV and 285.9 eV, corresponding to CO molecules adsorbed on on-top and bridge sites of plain Pt(111), respectively. The on-top: bridge distribution is also the same as in the case of the reference platinum surface at the same temperature (Fig. II-3a). This indicates clearly that the ZnO is discontinuous and patches of CO-covered Pt(111) coexist with ZnO areas.

We define the ratio θ_{Pt} as

$$\theta_{Pt} = \frac{[R_{C\ 1s}^{CO}(T)]_{ZnO/Pt(111)}}{[R_{C\ 1s}^{CO}(T)]_{Pt(111)}}$$

Where $[R_{C\ 1s}^{CO}(T)]_{ZnO/Pt(111)}$ is the normalized adsorbed CO intensity parameter measured on ZnO/Pt(111) sample. The ratio θ_{Pt} can be assimilated to the fraction of the surface which is *not* covered by ZnO (The CO coverage on plain Pt(111) depends on temperature (see above)). The evolution of θ_{Pt} as a function of temperature is shown in Fig. II-6a. Considering that, at each

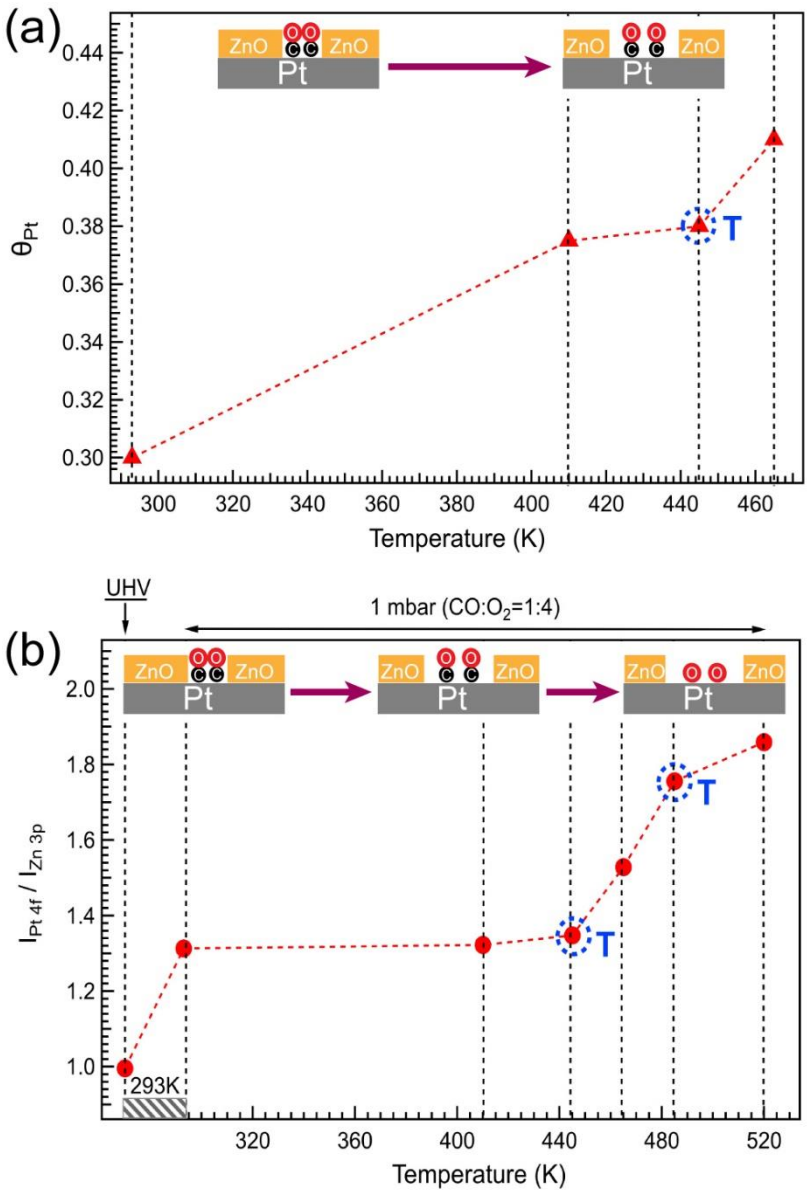

Figure II-6. (a) Variation of θ_{Pt} (the fraction of Pt substrate uncovered by ZnO). (see text) for the ZnO/Pt(111) surface exposed to the O_2:CO mixture (total pressure of 1 mbar) in the temperature range where CO is still adsorbed on Pt patches (steady-state conditions, except for 380 K). (b) The I_{Pt4f}/I_{Zn3p} ratio evolution as a function of the temperature (obtained from the fits of Zn 3p and Pt 4f spectra measured at hν =165 eV, see SI, Fig. S2). Solid lines are only guides for the eye. T stands for transient.

heating step, the CO surface density is the same on the pure Pt(111) and on the ZnO-free Pt(111) patches, platinum areas covered with CO make up 28% of the total surface at room temperature.

The Pt 4f to Zn 3p intensity ratio I_{Pt4f}/I_{Zn3p} (see Fig. 6b) gives also qualitative information on the surface fraction uncovered by ZnO, especially when CO titration is impossible (i.e. in UHV). A variation in the I_{Pt4f}/I_{Zn3p} ratio sheds light on a rather unexpected event: ZnO de-wetting already occurs *at room temperature* upon exposure to CO. Despite the fact that the Pt 4f signal should be attenuated at 90 eV kinetic energy by the adsorption of a layer of CO (CO

does not adsorbs on ZnO), the I_{Pt4f}/I_{Zn3p} intensity *increases* after introduction of the gas mixture.

ZnO de-wetting at room temperature after exposure to the gas mixture is confirmed by changes in the STM images of the ZnO/Pt(111) surface. Fig. II-7a shows the surface at room temperature in UHV, after the fabrication of the ZnO layer. Most of the Pt(111) surface is covered by ZnO: most of the surface is covered by a *ZnO* monolayer film (*89.5% of the whole surface), and a bi-layer film ZnO (7% of the surface).* The free Pt(111) area is only 3.5% of the whole area. We only observe the compact Zn_6O_6 structure: the coincidence mesh (a moiré pattern) between ZnO (5×5) and Pt(111) (6×6) appears at white dots adopting a compact hexagonal cell. Note the absence of the (4×4) pattern that appears only at very low ZnO coverage.[116] DFT calculations of the cognate system, ZnO/Pd(111), show that the (6×6) layer could be also hydroxylated under the form of $Zn_6(OH)_6$.[118]

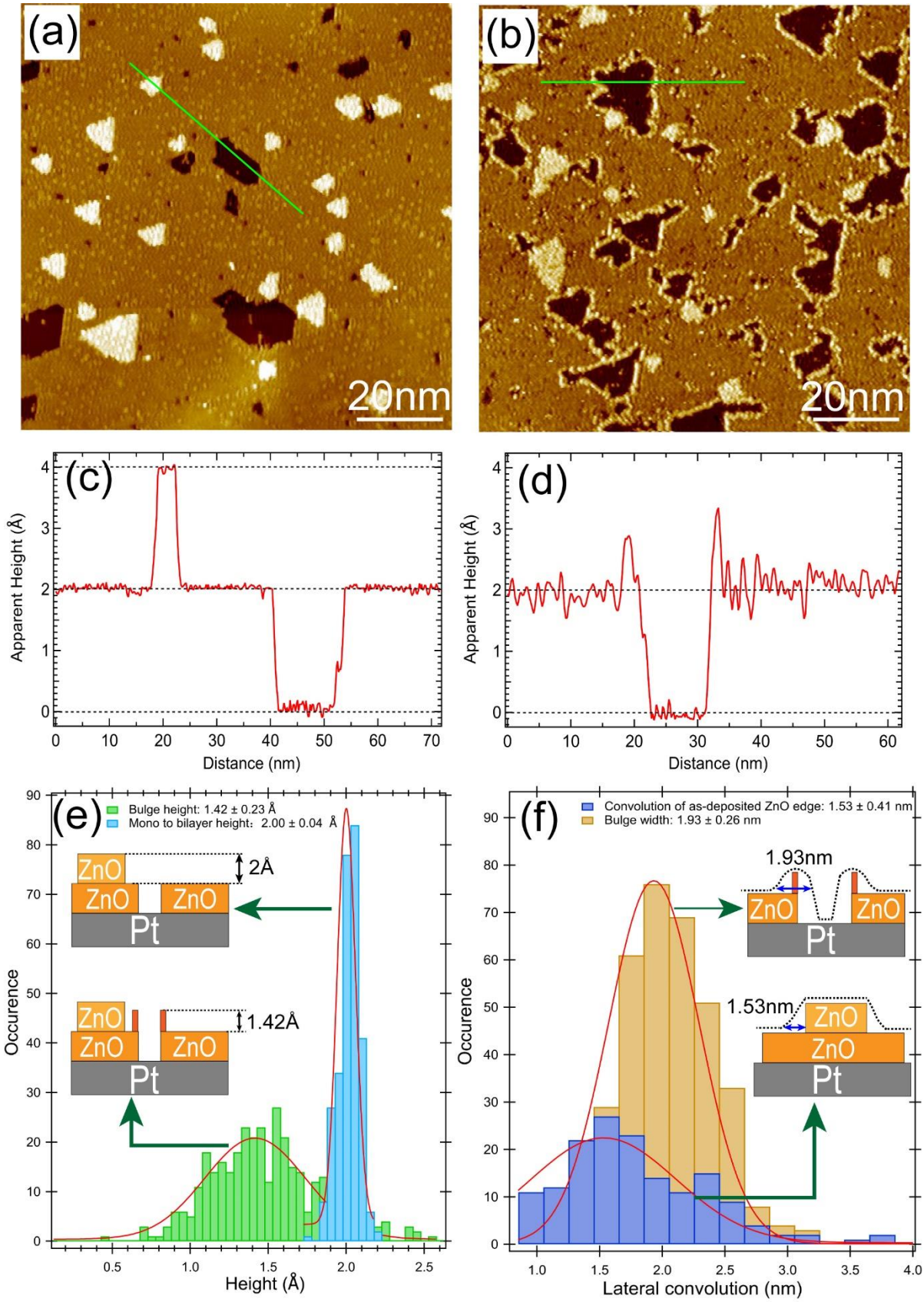

Figure II-7. (a) STM image (1.7 V, 270 pA) and (c) line scan plot of an as-deposited ZnO film covering 96.5 % of the whole Pt(111) surface. Dark brown, medium brown and light brown areas correspond to bare Pt(111) (3.5 % of the whole surface, at zero height), single-layered ZnO (89.5% of the whole surface at a nominal height of 2 Å), and bi-layered ZnO (7% of the surface, at nominal height 4 Å), respectively. The Pt/ZnO boundary length per surface unit is 0.060 ± 0.007 nm/nm^2. (b) STM image (1.7 V, 270 pA) and (d) line scan plot of the same sample as in (a) but after exposure to 1 mbar of the O_2:CO mixture (4:1) at room temperature, followed by pumping down to UHV. Note that the percentage of CO-covered Pt area has increased to 17.5%, and that of double-layer ZnO patches to 12.5%. A "bulge" tends to form at the Pt/ZnO boundary. (e) Histogram height distribution of the "bulge" and of the mono-to-bilayer ZnO domain as schematized. (f) Histogram lateral extension of the STM tip convolution at the ZnO domain and the "bulge" boundaries as schematized. The Pt/ZnO boundary length per surface unit has now increased to 0.17 ± 0.02 nm/nm^2.

Fig. II-7b shows the same surface after exposure to 1 mbar of the gas mixture ($CO+O_2$) and pumping down to UHV. We see that the dark brown platinum areas have increased at the expense of the ZnO areas. They correspond now to 17.5% of the whole area. The latter value is somewhat smaller than the CO-titrated platinum area fraction θ_{Pt} of 28%. Not only have the ZnO patches shrinked, but their morphology has changed. The exposure to the gas mixture, has eliminated the moiré pattern and led to an apparent disorder. Interestingly, a "bulge" forms specifically at the platinum/ZnO boundary (see the line-scan in Fig. II-7b and II-7d). The observed bulge can result (i) either from a chemical reaction at the Pt/ZnO boundary affecting the electron density or (ii) from the formation of a second ZnO sheet. Fig. II-7e compares the statistics on "peripheral bulge" heights (1.42 ± 0.23 Å) to those on "mono-to-bilayer" step heights, prior to gas exposure (2.00 ± 0.04 Å). Fig. II-7f shows also that the lateral extension of the bulge is ~19 Å. In fact, this extension is only apparent, being due to the inertia of the tip during scanning. An evidence of this effect is given by the lateral extension of the atomically abrupt "platinum-to-ZnO-monolayer" step of the pristine ZnO/Pt(111) surface that is already ~15 Å. Therefore, the hypothesis of a chemical reaction limited to the Pt/ZnO boundary copes with the STM data.

Besides the de-wetting effect due to the exposure to the gas mixture at room temperature, the second noticeable observation provided by NAP-XPS is the appearance of a C 1s component peaked at 289.0 eV (Fig. II-4a). Such a component is *absent* in the spectrum of the reference bare platinum surface (Fig. II-3a). Therefore, we attribute it to an adsorbate sitting on the ZnO patches and/or at their periphery. The observed binding energy is too low for being attributed to that of a carbonate (290.4 eV[140] on wurtzite ZnO), but falls within the range of a carboxyl (OCOH), found at ~289 eV (on OH/Au(111) at 90 K[141]) or of a formate (HCOO), found at 289.6 eV on wurtzite ZnO.[140,142] Carboxyls make strong bonds on Pt top sites (-2.44 eV according to DFT calculations,[143] via the formation of a Pt-C bond), and therefore they should be expected at the ZnO/Pt boundary. Formates, that form on hydroxylated wurtzite surfaces,[144] may also appear on the ZnO patches. They could also be present at the Pt/ZnO boundary, as the bond energy of the bidentate on platinum (2 Pt-O bonds) is similar to that of the carboxyl (-2.31 eV[143]). The C 1s spectrum (Fig. II-4a, see also Table S2) is in fact fitted with two components of FWHM = 0.5 eV each, one positioned at 289.0 eV (carboxyls) and one at 289.5 eV (formate). At room temperature the carboxyl component dominates the spectral weight.

We conjecture that the appearance of the carboxyl/formate species results from the *associative reaction* of CO with hydroxyls provided by the ZnO patches (the issue of a reaction occurring

on the oxide patches or at the ZnO/Pt boundary will be addressed further on). At room temperature and after exposure, the calibrated ratio of carboxyl/formate by the corresponding adsorbed CO, ($\frac{I_{C\,1s\,NAPXPS}^{carboxyl/formate}(293\,K)}{I_{C\,1s\,NAPXPS}^{CO_{ad}}(293\,K)}$), is ~0.67 (see Table S3). $I_{C\,1s\,NAP-XPS}^{carboxyl/formate}$ is the ratio of carboxyls/formates integral intensities as obtained from the fitting of the carboxyls and formates peaks in the C 1s XPS spectra, and . $I_{C\,1s\,NAP-XPS}^{COgas}$ is the integral intensity obtained from the fitting of the CO gas phase peaks in the XPS C 1s spectra. Therefore, taking into account that the Pt fraction is ~0.3, and taking a (maximum) CO coverage of 0.68 $ML_{Pt(111)}$ on Pt(111)[134], the surface density of the carboxyl/formate species is 0.67 × 0.3 × 0.68 $ML_{Pt(111)}$, that is 0.136 ML (1 $ML_{Pt(111)}$ is 1.5×10^{15} atoms cm^{-2}) or 2×10^{14} atoms cm^{-2}. Most importantly for the following discussion, the evolution of the carboxyl/formate surface coverage as a function of temperature was determined from its calibrated C 1s intensity, via the parameter $R_{C1s}^{carboxyl/formate}(T) = \frac{I_{C\,1s\,NAP-XPS}^{carboxyl/formate}(T)}{I_{C\,1s\,NAP-XPS}^{COgas}(T)} \times p_{QMS}^{CO}(T)$ (Table S3) The $R_{C1s}^{carboxyl/formate}$ value does not change much (the variation is less than 17%) between room temperature and 485 K (a transient state). Its coverage at 520 K is unknown due to the lack of gaseous signal.

In Regime I, at 410 K, ZnO/Pt(111) is more reactive than plain Pt(111), as indicated by the QMS data. The de-wetting of the ZnO layer has still increased with respect to room temperature, as now platinum patches represent ~38% of the surface area. The binding energy of the centroid of carboxyl/formate species increases by 0.2 eV with respect to the room temperature value, corresponding to an increase of the formate component at the expense of the carboxyl one (now 66 % of the spectral weight, Table S2). The solid phase O 1s spectrum encompasses several components relative to the (hydroxylated) oxide and the various adsorbates that may have overlapping binding energies: O^{2-} in ZnO (529.5 eV), bridge CO on Pt (531.0 eV), OH in ZnO at 531.7 eV, on-top CO on Pt (532.5 eV) and the carboxyl/formate on ZnO (~533.0 eV according to Ref.[140]) (Fig. II-4b). Keeping the two components (at 529.38 eV, FWHM = 0.8 eV) and (at ~531.4 eV, FWHM = 1.2 eV, noted (ads)), that accounted for the O^{2-} and OH in UHV (prior to the exposure to the gas mixture), the component at 531.4 eV /component at 529.38 eV / ratio doubles at 410 K in the presence of the gas mixture (see Fig. S3). This is due to the appearance of the "CO+OH" (carboxyls/formates) at ZnO patches and of CO molecules on Pt(111) areas (see component noted (ads) in Fig. II-4b).

In regime II (up to 465 K), as in the case of plain Pt(111), there is an appreciable increase in surface reactivity as CO starts to be depleted in the gas layers close to the surface. As CO is

still adsorbed on Pt patches (see Fig. II-4a, we can determine θ_{Pt} and find that de-wetting still increases as $\theta_{Pt} = 41\%$ (Fig. II-6a). Despite the ZnO film coverage is about 60%, the measured partial pressure of CO (or of CO_2) is identical to that of the plain Pt(111) surface. Unless the intrinsic CO oxidation rates on plain Pt(111) and on ZnO/Pt(111) are coincidentally equal at this temperature, one would expect some scaling effect[100] of θ_{Pt} on the steady-state CO_2 partial pressures. Imagine for instance that Pt is orders of magnitude more reactive than ZnO, then one would have expected a lower partial CO_2 pressure for ZnO/Pt(111) than for plain Pt(111). This is not observed. The intricacy between physics (transport) and surface chemistry is already such that the intrinsic reaction rates cannot be determined for both types of surfaces, although the CO partial pressure is not nullified, a generally admitted criterion for MTL. Although the intrinsic TOFs of ZnO/Pt(111) and plain Pt(111) cannot be compared in this regime, the NAP-XPS setup still provides invaluable data on the chemical state of the surface in operando conditions. Besides oxide de-wetting, we observe a binding energy change in the "CO+OH" (OCOH/HCOO) species. Indeed, the corresponding C 1s binding energy centroid increases from 289.0 eV (room temperature) to 289.46 eV. This 0.46 eV binding energy shift is significant of a change in the bonding configuration. With the two-component fitting we see now that the formates are majority species (see Table S2). This situation holds for higher temperatures (see below).

Therefore, we propose that carboxyls transform into formates when the temperature is raised. Indeed, this process is certainly activated as the OH bond and the Pt-C bond must be broken. Note that the produced CO_2 does not transform ZnO film into $ZnCO_3$.

In Regime III (up to 520 K) the surface intrinsic reactivity is so high that gaseous CO is fully depleted, similar to what is seen for plain Pt(111). However, dramatic changes in the NAP-XPS spectra of the condensed phase concern essentially the platinum patches. As for the reference Pt(111) surface, the C 1s spectrum (Fig. II-4a) shows that all CO molecules have desorbed from the surface. The only remaining C 1s component is still peaked at at 289.5 eV, and therefore the majority "CO+OH" species is a formate, as in Regime II. No carbonates are formed. The work function increases by about +0.4 eV (the ΔBE_{FL}(gas-phase) is of -0.37 eV (CO_2 C 1s) and -0.36 eV (O_2 O 1s), which suggests that CO is replaced by atomic oxygen on platinum patches, as it is the case for the Pt(111) reference. However, it is difficult to get a direct evidence of Pt-O bond formation as the corresponding O 1s component, positioned at 530.0 eV (Fig. II-4b), is hidden by the O^{2-} ZnO component. The component at 531.4 eV /component at 529.38 eV / ratio is now smaller than that in UHV (room temperature) (see Fig. S3). This is essentially

due to the desorption of CO and the formation of Pt-O bonds. In this oxygen rich conditions, and because of the extremely low CO partial pressure, one could expect that OHs are replaced by O^{2-}.[145] This is not that we observe. Note that in UHV, hydroxyls on ZnO leave the surface at ~500 K for the monolayer (but at a higher temperature of ~700 K for the bilayer).[117]

The carboxyls and formates species, reaction intermediates or spectators? While there is an abundant experimental and theoretical literature on the adsorption of small molecules" like CO and CO_2 on wurtzite ZnO surfaces,[139,142,146,147] the surface chemistry of partially hydroxylated mono- and bi-layers of ZnO on Pt(111), has not been explored yet in great detail. In fact, the present NAP-XPS study sheds new light on the chemistry of these discontinuous ZnO monolayer films on Pt(111). Two major experimental facts brought about by NAP-XPS are (i) the hydroxylation of the ZnO layer on Pt(111), and (ii) the associative reaction between CO molecules and hydroxyls provided by zinc oxide. In the following, *we will discuss how zinc oxide-bound hydroxyls play a pivotal role these phenomena.* The role of OHs in the catalytic oxidation of CO on ZnO/Pt(111) was not addressed in the preceding work (2013) by Martynova et al.,[112] but the observation that ZnO on Pt(111) is (partially) hydroxylated was made later on by the same group. A negative experiment concerning the ZnO/Ag(111) system points also to the role of hydroxyls: the ZnO/Ag(111) system is not more reactive than the bare noble metal.[122] In fact, Ag(111) does not share the capacity of Pt(111) and Pd(111)[118] to dissociate water (and H_2) from the residual gases, and then to hydroxylate the ZnO layers.[145] Because of the presence of hydroxyls attached to ZnO, it is not surprising that in the present case, the oxidation of CO by O_2 exhibits similarities with the water gas shift reaction, especially with regard to the "CO+OH" species, carboxyls and formates.[16,141,143,148,149]

We believe that the "CO+OH" associative reaction observed by NAP-XPS, at the heart of the discussion on ZnO/Pt synergistic effects, occurs at the Pt/ZnO boundary, following the general screenplay[16,150,151] of inverse oxide/Pt model catalysts. First, the elimination of the moiré pattern in the STM images cannot be used as an evidence for the reaction of "inner" OHs, as the strain due to the peripheral reaction may impact the coincidence mesh. Second, as discussed before, the "bulge" seen in the STM images at the Pt/ZnO boundary may be signature of reaction products building up there. Third, and more importantly, the associative reaction should necessarily take place at the Pt/ZnO boundary, where both adsorbed CO (via a Pt-CO bond) and hydroxyls (bound to ZnO) can be found *at short distances*.

To support this hypothesis, we have estimated the amount of carboxyl/formate species that could be formed considering the Pt/ZnO boundary length per surface unit. For Pt patches representing 17 % of the total surface (see the STM images in Fig. II-7) the boundary length per unit area is ~0.2 nm/nm^2 at room temperature after exposure to the gas mixture. The sample studied by NAP-XPS presents more developed Pt patches (~30% of the whole area), therefore the boundary length per unit area should be greater than that seen in the STM image of Fig. II-7b. Considering the STM data provided by Martynova et al.[112] where the boundary length per unit area is plotted against the ZnO coverage, a value of ~0.3 nm/nm^2 is obtained. Taking the lattice parameter *a* of wurtzite ZnO (0.325 nm), one obtains ~10^{14} O or Zn sites per cm^2. This value has the same order of magnitude as our estimate of the carboxyl/formate coverage (~2×10^{14} cm^{-2}, from calibrated C 1s NAP-XPS, see above), that remains roughly constant through the various temperature stages. Therefore, "CO+OH" species formed at the periphery of the ZnO patches can contribute to a large part of the species detected by NAP-XPS.

To understand the formation of the carboxyl/formate species, the description of the Pt/ZnO boundary must go down to the atomic level. We limit ourselves to the simple case of monolayer ZnO patches on Pt(111). If the "bulge" observed in STM does correspond to a two-layer thick boundary (although the apparent height is less), the present modelling has to be refined, but the general ideas exposed here are still valid. The monolayer ZnO "ribbon" depicted in Fig. II-8 exhibits two types of hydroxyl terminations, the S-type hydroxyl (bonded to 1 Zn ion) and the D-type one (bridging two Zn ions) on O-edges. The "inner" T-type hydroxyl (bonded to 3 Zn ions, the most highly coordinated of all OHs) is not considered for the reaction.

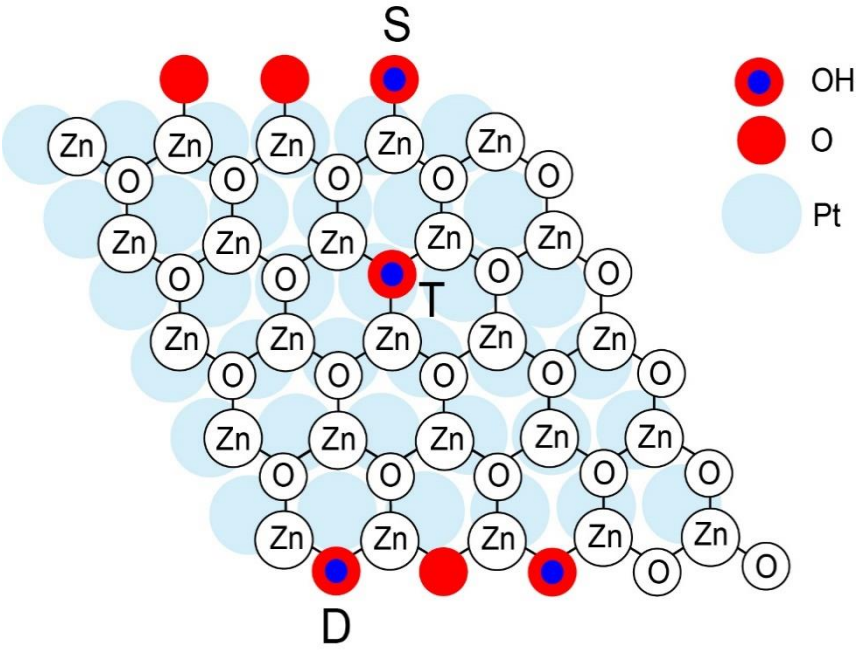

Figure II-8. Scheme of the ZnO/Pt boundaries. "S", "T" and "D" indicate hydroxyl species at three different locations. On the top of the ribbon, the zinc edge presents undercoordinated Zn ions, zinc ions with O terminations resulting from the dissociation of an O_2 molecule, and S type hydroxyl: involving a dissociated oxygen singly coordinated to a zinc atom. In the middle, T type hydroxyl involving an in-plane oxygen coordinated to three zinc atoms. The bottom part of the ribbon is terminated by an oxygen edge, where each oxygen (or hydroxyl) is coordinated to two zinc atoms: D type hydroxyls.

We do not consider in this discussion the direct reaction of a CO molecule with the D type hydroxyl (Fig. II-8), as it would lead to the formation of an O vacancy. We show in Fig. II-9 the possible reaction steps between CO and a S-type hydroxyl. The CO and the OH sit at short distance (step 1). From the transition state (TS), a carboxyl is formed (step 2). An O_2 molecule dissociates (step 3) next to the carboxyl on two free Zn ions (this is the reaction on the coordinatively unsaturated metal cation combined to a nearby platinum atom, described theoretically by Sun et al.[111]), giving 2 Zn-O bonds (step 3). Then the H from the carboxyl can be transferred to one Zn-O to re-form a new S-type hydroxyl, and the CO_2 molecule desorbs (step 4). In that case, CO oxidation is co-catalyzed by the OHs, whose surface density is not

depleted by the reaction. The inverse ZnO/Pt(111) model catalyst should present similarities with the FeO/Pt(111) system, in which hydroxyls act also as co-catalysts.[152]

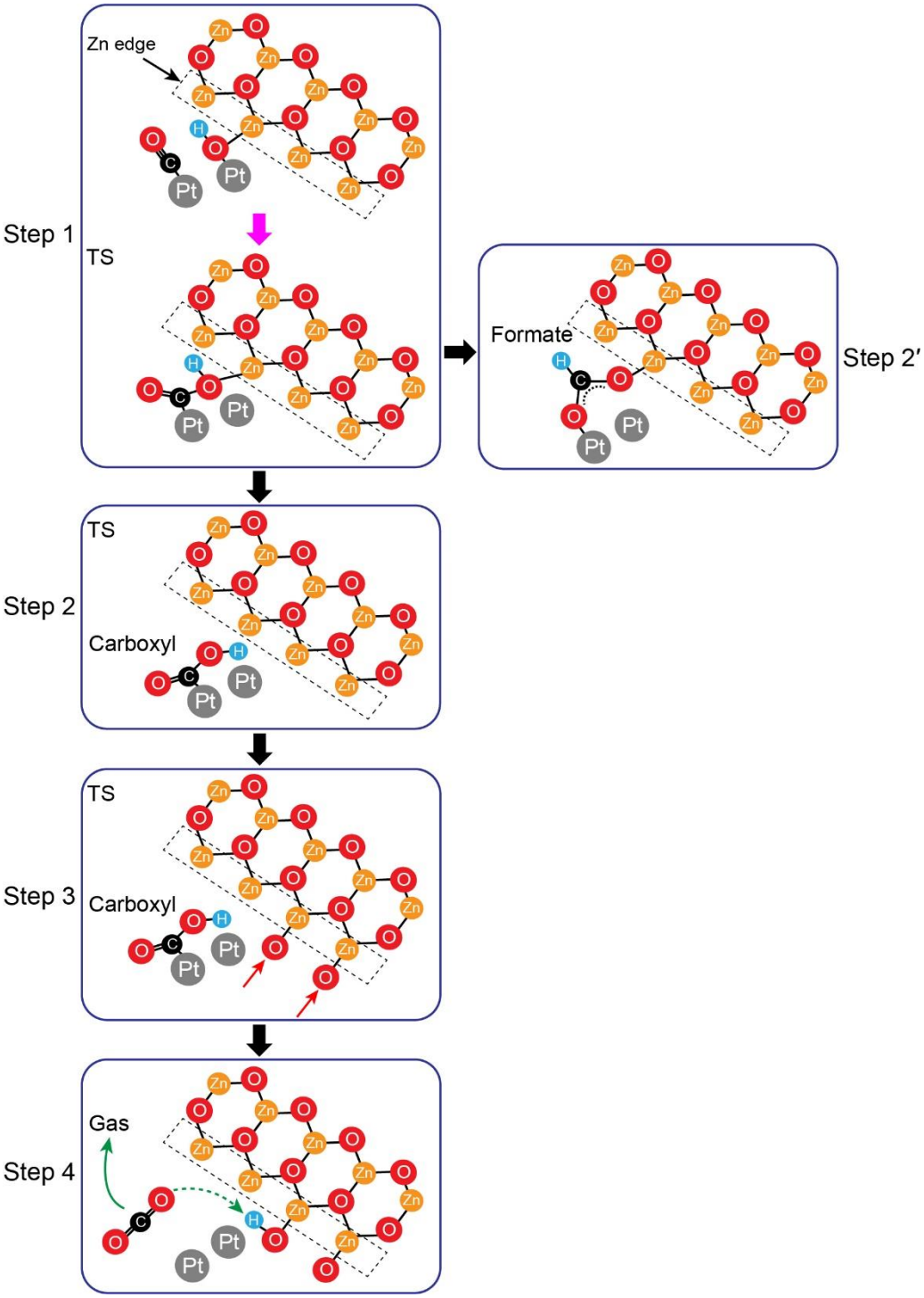

Figure II-9. Scheme of the CO oxidation reaction mechanism. Associative reactions at a Zn-edge ZnO boundary between a CO molecule bound to Pt and an S-type hydroxyl leading to a carboxyl, then to CO_2 desorption (steps 1 to 4) with OH as a co-catalyst or leading to a formate (step 1 to 2').

By increasing the temperature, C 1s NAP-XPS shows that the (CO+OH) associative species change their bonding configuration. On the basis of simple geometric considerations and considering the bonding modes of adsorbed CO on Pt and OH at the periphery of the ZnO patches, the direct formation of a formate HCOO from CO and a S-type OH in a single elementary step seems impossible: in fact, CO binds through its C end to Pt, and thus, CO has to flip and change its orientation before the formate can be produced, as the latter one binds only through its two O atoms. Therefore, we propose that the reaction path leading to a formate species starts from the same TS as that of the carboxyl. However, instead of reaching a nearby O atom, the H atom jumps onto the C atom of the TS while the Pt-C bond is broken (step 2' in Fig. II-9). This leads to a bidendate formate. As there is no re-formation of a peripheral hydroxyl, the production of a formate would be a dead-end. Therefore, contrary to the carboxyl species that are intermediary species in CO oxidation, we believe that the formate species that appear at high temperatures are simply spectators. Even in the water gas shift reaction on plain Pt(111) where water is fed in, formate species are considered as spectators.[143]

That reaction paths envisioned here should be calculated to give a theoretical support to our proposition. However, it is clear that the model used in Ref. [111] (where a single TM oxide monolayer is considered) should be substantially improved, by taking into account the presence of OH species and, possibly, the formation of a two-layer thick zinc oxide at the Pt/ZnO boundary.

Table 1: *The normalized adsorbed CO intensities,* $R_{C1s}^{CO}(T) = \frac{I_{C\,1s\,NAP-XPS}^{COads}(T)}{I_{C\,1s\,NAP-XPS}^{COgas}(T)} \times p_{QMS}^{CO}(T)$*, as a function of the temperature. Time is the acquisition time of the* P_{QMS}^{CO} *corresponding to each C 1s XPS.* P_{QMS}^{CO} *indicates the corresponding pressure of CO monitored by QMS.* $I_{C\,1s\,NAP-XPS}^{COgas}$ *and* $I_{C\,1s\,NAP-XPS}^{COads}$ *are the integral intensities calculated from the fitting of the CO gas phase and the adsorbed CO peaks in C 1s XPS.*

Temperature (K)	Time (min)	P_{QMS}^{CO} (mbar)	$I_{C\,1s\,NAP-XPS}^{COgas}$	$I_{C\,1s\,NAP-XPS}^{COads}$	$Normalized\ R_{C1s}^{CO}$
293	19	0.25	1.20	6.81	1
410	330	0.22	1.09	6.53	0.89
445	485	0.16	1.00	7.26	0.80
465	681	0.13	0.80	6.86	0.74

Table 2: *The fitting parameters of the formate and the carboxyl in C 1s XPS of ZnO/Pt(111) and the evolution of the* $I_{Formate}$ */* $I_{Carboxyl}$ *ratio as a function of the temperature.*

	Formate		Carboxyl		
	BE	FWHM	BE	FWHM	$I_{Formate}$ / $I_{Carboxyl}$
293 K	289.51	0.99	288.79	1.00	0.43
410 K	289.59	0.95	288.92	1.00	0.66
445 K	289.57	0.99	288.83	1.00	1.51
465 K	289.65	1.00	288.95	1.00	1.65
485 K	289.65	0.99	288.91	1.00	3.31
520 K	289.53	1.10	288.80	1.10	3.54

Table 3: *The calibrated formate/carboxyl intensities as a function of the temperature,* $R_{C1s}^{carboxyl/formate}(T) = \frac{I_{C\,1s\,NAP-XPS}^{carboxyl/formate}(T)}{I_{C\,1s\,NAP-XPS}^{COgas}(T)} \times p_{QMS}^{CO}(T)$. *Time is the acquisition time of the* P_{QMS}^{CO} *corresponding to each C 1s XPS.* P_{QMS}^{CO} *indicates the corresponding pressure of CO monitored by QMS.* $I_{C\,1s\,NAP-XPS}^{COgas}$ *is the integral intensity obtained from the fitting of the CO gas phase peaks in the XPS C 1s spectra, and* $I_{C\,1s\,NAP-XPS}^{carboxyl/formate}$ *is the ratio of carboxyls/formates integral intensities as obtained from the fitting the carboxyls and formates peaks in the C 1s XPS spectra.*

Temperature (K)	Time (min)	p_{QMS}^{CO} (mbar)	$I_{C\,1s\,NAP-XPS}^{COgas}$	$I_{C\,1s\,NAP-XPS}^{COads}$	$I_{C\,1s\,NAP-XPS}^{carboxyl/formate}$	$R_{C1s}^{carboxyl/formate}$
293	28	0.25	2.19	3.88	2.6	0.30
410	571	0.18	1.45	3.84	2.0	0.25
445	732	0.17	1.30	3.38	2.07	0.27
465	914	0.13	1.15	4.06	2.07	0.23
485	1108	0.09	0.83	4.4	2.74	0.29

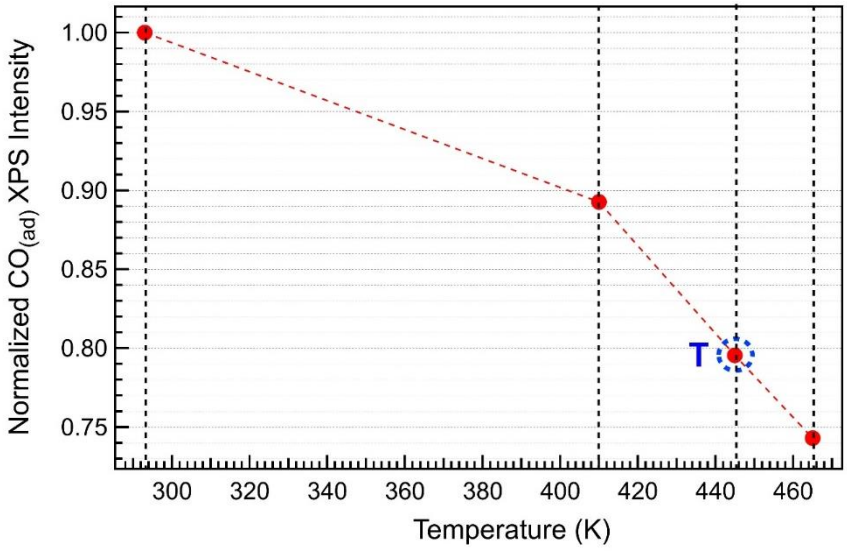

Figure S1. *The normalized adsorbed CO intensities on Pt(111) as a function of the heating temperature.*

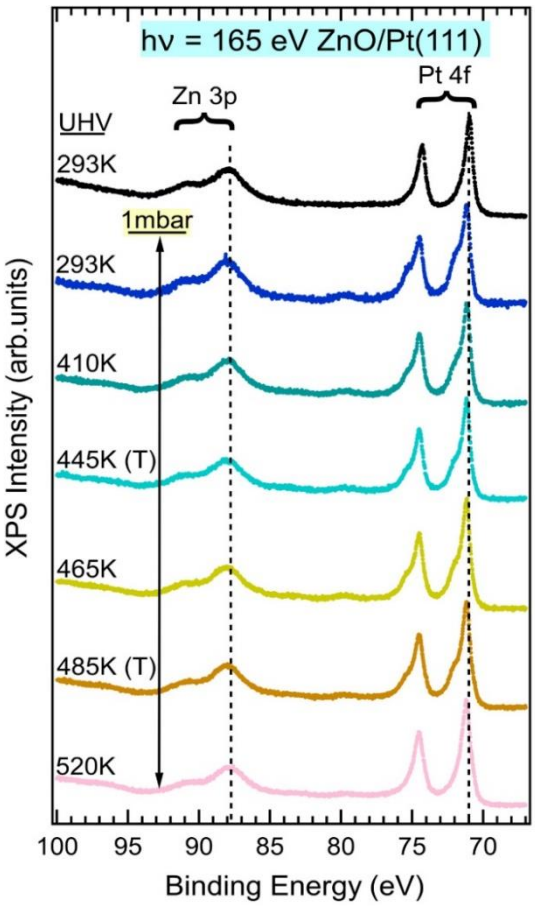

Figure S2. *Pt 4f and Zn 3p binding energy region of the ZnO/Pt(111) sample measured at hυ = 165 eV in a CO:O₂ mixture (1:4) under a total pressure of 1 mbar. The spectra denoted UHV are recorded at 293 K before exposure to gases.*

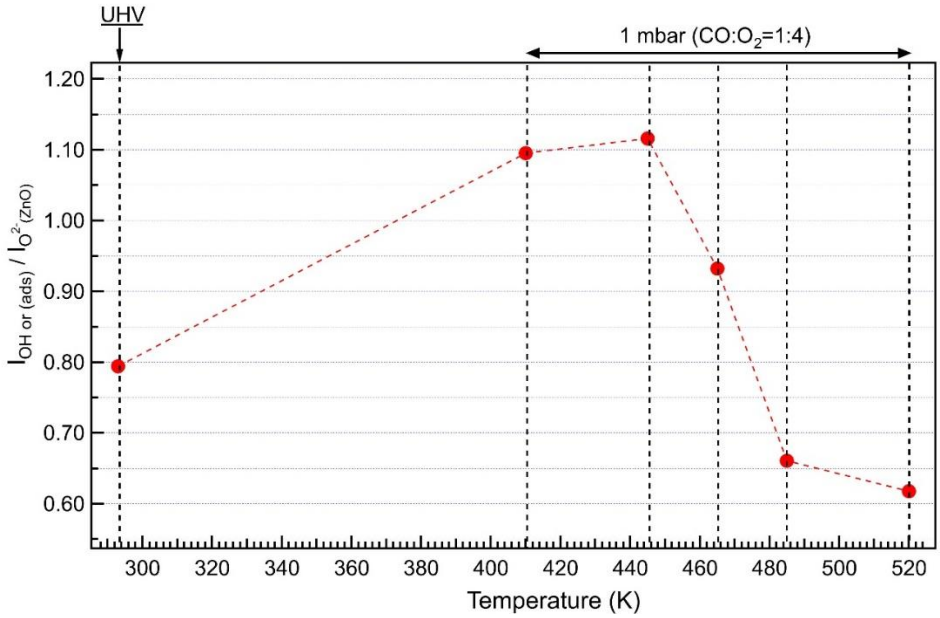

Figure S3. *The evolution of the $I_{OH\ or\ (ads)}/\ I_{O^{2-}(ZnO)}$ ratio as a function of the temperature at 1 mbar of CO: O₂ mixture (1:4) calculated from the O 1s spectra of the ZnO/Pt(111).*

4. Conclusions

The oxidation of carbon monoxide over the inverse model catalyst ZnO/Pt(111), a discontinuous ZnO monolayer on Pt(111), was systematically compared to the same reaction over Pt(111), using principally NAP-XPS in operando conditions (O_2:CO mixture with a 4:1 ratio, under a pressure of 1 mbar), and, additionally STM in UHV and after exposure to the gas mixture. The NAP-XPS analysis chamber is a special case of a flow reactor, with a large volume of 35 L, and a small molar flow rate of 1 mL_n/min. Thanks to a mass spectrometer embedded in the NAP-XPS setup, we could compare the molar fractions of the reagents and products at a given temperature for both surfaces, and validate them by comparison with gas-phase XPS data. It was possible to determine the conditions under which mass transfer limitation effects start to occur and affect the measurement of reaction rates, an issue that is too often overlooked in the field of operando measurements. In particular, contrary to a widely accepted belief, our comparative study has shown that mass transport limitation is seen at a rather early stage, before the CO reactant (the limiting species in the mixture) is fully depleted from the gas layers above the surface, and before CO is replaced by atomic O on Pt. As the present NAP-XPS setup design is one of the most popular worldwide, lessons drawn from the present experiments, especially the mass transfer issue, have some generality and impact.

The general objective of the study was to characterize the surface chemistry of the inverse catalyst, especially in conditions where it appears more reactive than the plain Pt(111) surface. Via the measurement of the steady-state CO_2 molar fraction, a proxy of the reactivity, we observed that the reaction rate over ZnO/Pt(111) system is superior to that over Pt(111) in a temperature range extending to 410 K. At higher temperatures (from 465 K), mass transfer limitation occurs on both surfaces, which makes the comparison of their intrinsic reactivity impossible. However, crucial information on the surface chemistry in operando conditions can be collected at any temperature. This is the great advantage of NAP-XPS with respect to catalytic studies based solely on measurements of reagent/product concentrations in the gas phase.

In addition, the measurement of the gas-phase components in the NAP-XPS spectra, provides a straightforward procedure to calibrate the surface concentration of the various species adsorbed on the surface. The comparison with the plain Pt(111) surface is always fruitful. The CO titration method we used enabled us to follow the dynamics of the discontinuous ZnO monolayer film in the presence of the gas mixture, and more especially the extension of the Pt

patches at the expense of the ZnO ones, even at room temperature. Given that the surface concentration of CO on plain Pt(111) is well known, estimates of the surface concentration of surface reaction products between CO and ZnO could be also obtained.

Indeed, another benefit drawn from the comparison of ZnO/Pt(111) with the well-studied Pt(111) was the possibility to detect straightforwardly the adsorbed species common to both surfaces, i.e. CO on the Pt patches of ZnO/Pt(111), and those specific to ZnO/Pt(111), i.e. the species resulting from the "CO+OH" associative reaction (carboxyl and formates). The OH is provided by the ZnO that is heavily hydroxylated. An estimate of their surface concentration provided by NAP-XPS, and the determination of the ZnO film coverage, make that the "CO+OH" species are, in all likelihood, formed at the Pt/ZnO boundary during the exposure to the gas mixture. The carboxyl, the majority species present at low temperature (410 K), can be the intermediate species that leads to the evolution of CO_2, the zinc oxide bound OH being the co-catalyst. However, the majority species observed at high temperature (from 445 K to 520 K) is a formate. We discuss why the formate should be essentially a spectator, and why the synergistic effects between Pt and (hydroxylated) ZnO can only be expected at low temperature.

Chapter III. Synthesis of Bimetallic PtZn NPs

Continuous consumption of crude oil, increased exhaust emissions into the atmosphere and, as a consequence, inexorably growing cancer diseases cry out for the development of new technology using alternative energy sources other than fossil fuel. One of the most promising technology for efficient power and clean energy generation in the 21st century is polymer electrolyte membrane (or proton exchange membrane) fuel cell (PEMFC).[153–155] Platinum is by far the most effective element used for PEM fuel cell catalysts and nearly all current PEM fuel cells utilize platinum on porous carbon to facilitate both the anodic oxidation of hydrogen anode reaction and the cathodic reduction of oxygen cathode reaction.[156,157] If the hydrogen oxidation reaction (HOR) is a fairly fast kinetic process and does not pose any particular problems, then the oxygen reduction reaction (ORR) is a stumbling block due to the fact that the surface of the platinum catalyst tends to be shielded by the electrolyte or a hydroxy layer.[158] To improve the ORR activity, platinum catalysts should be either made with controlled shapes to reduce the binding strength between platinum atoms and the adsorbed ligands or alloyed with various transition metals.[159] For example, in a H_2SO_4 medium used as the supporting electrolyte, the ORR activity on Pt (100) is higher than that on Pt (111) owing to the different adsorption rate of sulfates and desorption rate of hydrogen.[160,161] Attempts to improve the reaction kinetics in oxygen reduction reaction (ORR) among the low-indexed planes of Pt_3Ni surfaces and Pt monolayer modified palladium particles were demonstrated.[162] These results suggest that one may expect significantly enhanced kinetics by fabricating catalysts with the proper crystal phase and composition so the arrangement of atoms is optimal and active sites are available for oxygen adsorption and reduction.

Along with iron, copper, nickel and cobalt, the alloy of platinum with zinc in recent years has attracted much attention, mainly due to the increased activity of such systems in various processes. As an example, enhancement of activity in PtZn nanoalloys toward the oxidation of formic acid and methanol were shown.[163,164] However, to this day the direct synthesis of these nanocrystals hasn't been widely described.

1. Elaboration of ZnPt Nanoalloys

Metallic nanoalloys consist in a total miscibility of the two constituting metals. In order to favors the miscibility, it is necessary to consider the co-reduction of two metallic precursors to induce a homogeneous nucleation in solution and prevent the segregation inducing the formation of two different populations. In this context, we first considered a mixture of similar

$Pt(acac)_2$ and $Zn(acac)_2$ precursors dispersed in oleylamine ($CH_3(CH_2)_7CH=CH(CH_2)_8NH_2$) by using a one-pot process developed previously in the laboratory.[57]

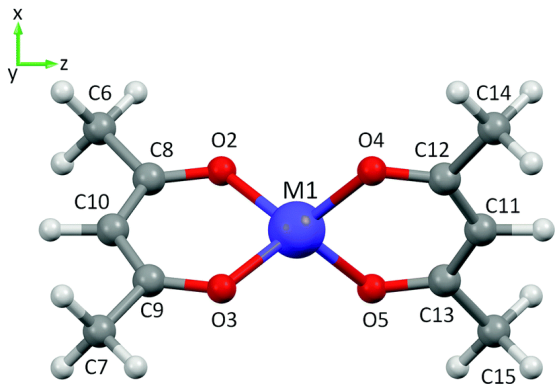

Scheme III-1. Molecular Structure of metal acetylacetonates: metal in blue, oxygen in red and carbon atoms in grey (from ref[165]).

Briefly, in a glove-box under nitrogen atmosphere 11 ml of oleylamine were mixed with 84 mg (0,213mmole) of $Pt(acac)_2$ and 57 mg (0,213 mmole) of $Zn(acac)_2$ in a 25 ml vial caped with a septa pierced by a pipette (to provide overpressure). The solution was stirred and heated using a 50 ml «drysyn» filled with sand. The mixture was heated by increasing the temperature by 5°C every minutes to reach 250°C, and then was kept at 250 °C for 1 hour (Scheme III-2) Then the solution was cooled down to room temperature and the nanoparticles were washed by adding 20 ml of ethanol and then centrifuged during 5 minutes at 4900 rpm. The resulting black precipitate containing the nanoparticles was then dispersed in toluene.

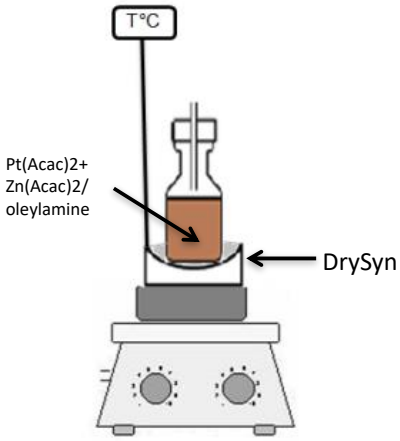

Scheme III-2. Experimental setup for the synthesis of Zn/Pt at 250°. The experiment was performed under nitrogen in a glove box.

The TEM images shown in the Fig. III-1 clearly give evidence of segregated phases. Large crystals of pure zinc oxide and 4 nm platinum nanoparticles are both obtained at the early stage of the reaction (Fig. III-1A). Increasing the synthesis time has no influence on the segregation as it only led to the growth of Pt NPs size from 4 to 8 nm (Fig. III-1 B). Such segregation, can

be explained by a difference in the decomposition rate of the two organometallic complexes depicted their similar $M(acac)_2$ structure (Scheme III-1).[165] Indeed, the decomposition of zinc occurs at 210 °C while the platinum salt decomposes at slightly higher temperature (240 °C). In this connection, the formation and growth of zinc and platinum nuclei occur at different speeds at different time intervals that explains the formation of zinc oxide and platinum nanoparticles instead of an alloy.

In this context it is necessary to consider another approach in order to run the decomposition process of both salts simultaneously to prevent the metals segregation.

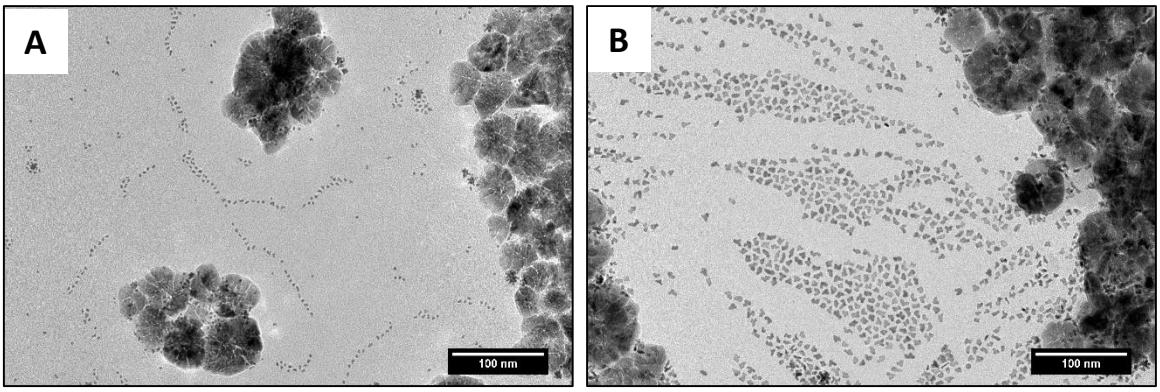

Figure III-1. TEM Images of resulted NPs after 5 min (A) and 3 hours (B)

In the literature, two papers describe the organometallic synthesis of Pt_xZn_{1-x} with different shape, size and compositions.[93,166] Similar $M(acac)_2$ precursors are used and solubilized either in pure oleylamine[93,166] or in acid oleic-oleylamine mixture.[93] A special piquancy to the synthesis is added by the fact that the two single articles on the one-pot production of the NCs are not totally in agreement. For instance, Kang et al[93] claims that the temperature of the reaction is the determining factor to incorporate Zn in the platinum lattice. Pure platinum nanocrystals are obtained at 270 °C while nanoalloys are favored at high temperature (300-350 °C). Thus, a sequential increase in the reaction temperature from 300 °C to the maximum possible 350 °C (the boiling point of oleylamine) increases the proportion of zinc from 15 to a maximal contain of 25 % of Zn. At 300°C in pure oleylamine, Zn_xPt_{1-x} (with $x < 25\%$) spherical nanoparticles with a large size dispersion are obtained (Fig. III-2B). At the same time, Sun et al. demonstrate that 5 nm Zn_xPt_{1-x} nanoparticles with a higher zinc content ($x = 48\%$) can be obtained in the same conditions (pure oleylamine at 300 °C).[166]

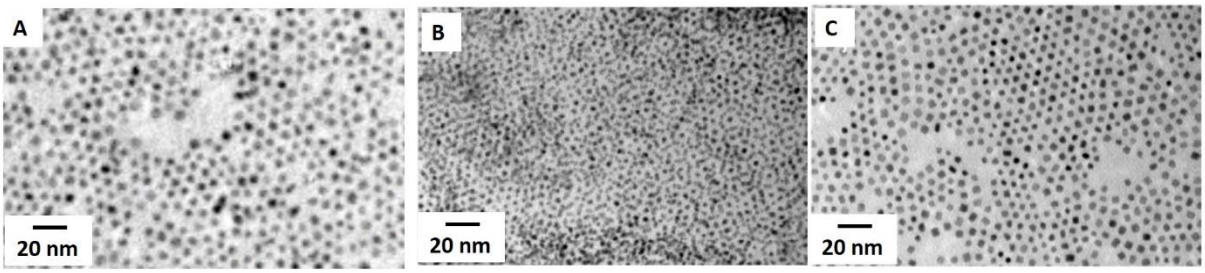

Figure III-2.Zn_xPt_{1-x} nanoparticles obtained at 300°C in the litterature A) 5 nm $Zn_{48}Pt_{52}$ in pure oleylamine from (from ref[166]) B) spherical polydisperse Zn_xPt_{1-x} (x<25%) in pure oleylamine (from ref[93]) and C) mixture of spherical and cubic Zn_xPt_{1-x} (x<25%) (from ref[93]).

In addition, Murray's group give evidence that benzyl ether additive in pure oleylamine could induce a morphological change of the nanoparticles from quasi-spherical (without adding) to cubic (with) (Fig. III-2C).[93] Obtaining predetermined facets of nanoparticles is widely demanded in the field of catalysis in particular the {100} facets. Thus, for example, the ORR activity in PEMFCs is indeed dependent on the shape (much less on the size) of the Pt NPs, which is indicated by the fact that the current density from the ORR for platinum nanocubes (only {100} facets) is four times that of polyhedral platinum or the truncated cubic Pt NP catalyst (mixed {100} and {111} facets). Therefore, producing cubic NPs was of particular interest to us. Thus, we have considered a protocol proposed in the literature and tried to adapt the synthesis.

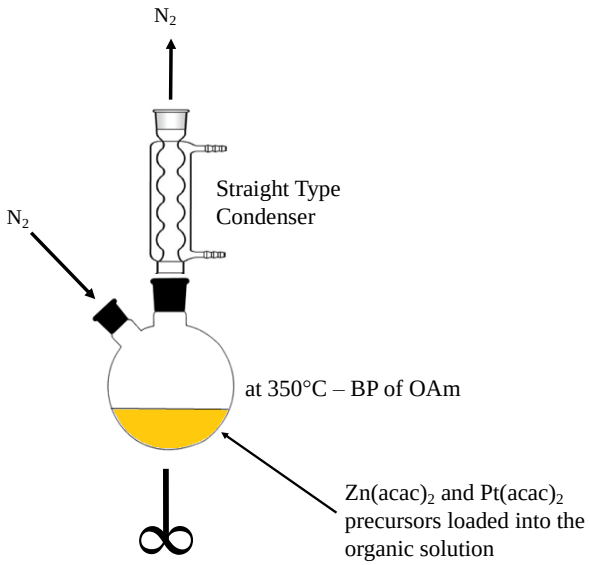

Scheme III-3. Experimental setup for the synthesis of Zn/Pt under reflux at 350°C.

First of all we have considered the synthesis of pure platinum and pure zinc nanoparticles starting from the experimental conditions of 0.05 mmol of $M(acac)_2$ precursor solubilized in 1.95 mL oleylamine (which is used as both stabilizing agent and solvent) and/or 1.25 mL of

benzyl ether under N_2 atmosphere. The solution is brought in reflux at 350 °C and is kept at this temperature for 5 min (see Scheme III-3). The reaction mixture is cooled, exposed to air and purified by ethanol. The final products are redispersed in toluene and few drops are deposited under a TEM grid (Fig. III-3). The synthesis results do not depend on the addition, or lack thereof, of benzyl ether. Thus, fabrication of pure Pt NPs leads to their agglomeration (Fig. III-3A). So if the production of zinc oxide nanoparticles (Fig. III-3B) with a broad size distribution and the large size of the particles themselves (more than 10 nm) is quite common, as has been demonstrated in many works on the synthesis of these nanocrystals from acetylacetonate,[167–170] the inability to obtain platinum nanoparticles in the same manner is a result unexpected in many ways.

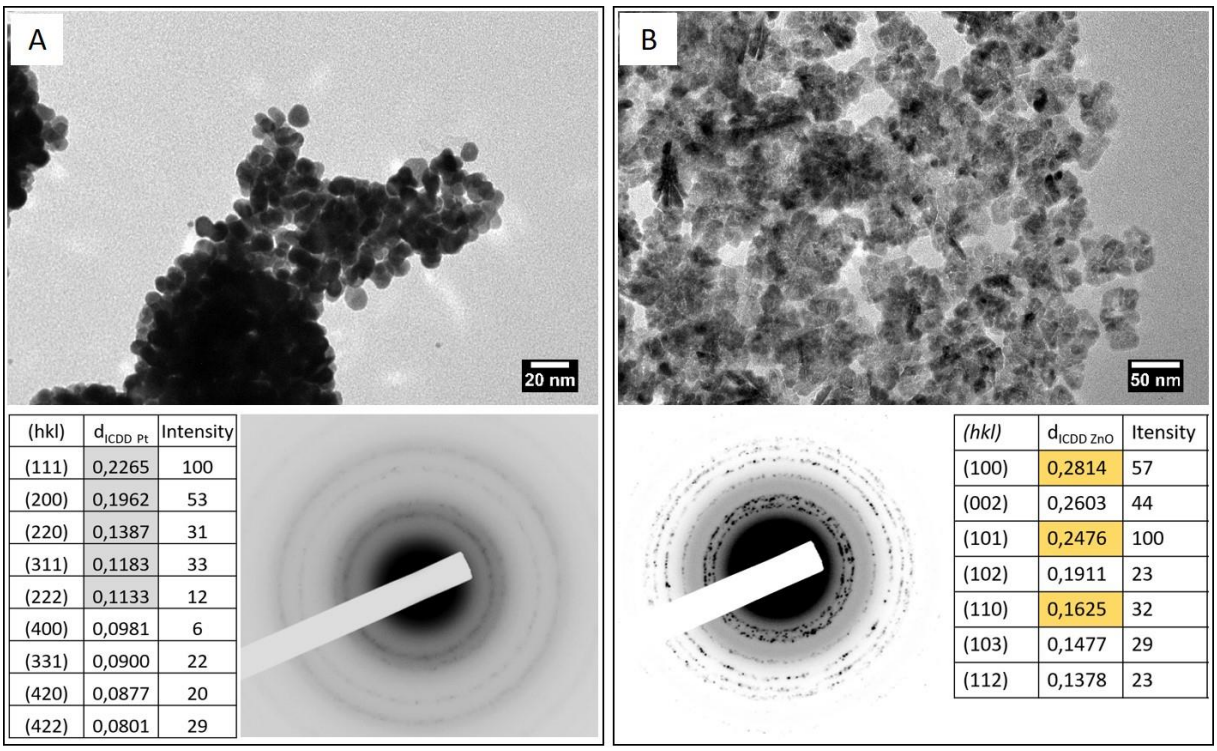

(hkl)	$d_{ICDD\ Pt}$	Intensity
(111)	0,2265	100
(200)	0,1962	53
(220)	0,1387	31
(311)	0,1183	33
(222)	0,1133	12
(400)	0,0981	6
(331)	0,0900	22
(420)	0,0877	20
(422)	0,0801	29

(hkl)	$d_{ICDD\ ZnO}$	Itensity
(100)	0,2814	57
(002)	0,2603	44
(101)	0,2476	100
(102)	0,1911	23
(110)	0,1625	32
(103)	0,1477	29
(112)	0,1378	23

Figure III-3:TEM Images of pure Pt (A) and ZnO (B) NPs and their corresponding diffraction patterns

We then undergo, the elaboration of ZnPt nanoalloy starting from the conditions of ref [93]. In this case a mixture of the two precursors with 0.04 g of platinum acetylacetonate [$Pt(acac)_2$] and 0.025 g of zinc acetylacetonate [$Zn(acac)_2$] dissolved in 7.5 ml of oleylamine (12 mmol) have been consider that corresponds to a molar ratio Pt:Zn of 1 and keeping constant the oleylamine:metal molar ratio of 225. As, in their article they use "*a combination of oleylamine and oleic acid to have monodisperse NCs*"[93] we consider 1.25 mL of oleic acid ($CH_3(CH_2)_7CH=CH(CH_2)_7COOH$) too. In this case, faceted nanoparticles can be obtained. As seen in the Fig. III-4, both metals have a synergistic effect on each other. Indeed as a result of

the reaction, 4.3±0.4 nm mixed-type quasi-spherical and cubic nanoparticles, similar to the benzylether/oleylamine mixture (Fig. III-2C), were obtained even without using benzyl ether. Although the authors insist on the need to use it to obtain cubic nanocrystals.

The structural characterization has been performed by electronic diffraction. It has to be noted that interplanar spacings of lattices planes in ZnPt (table Fig. III-4) are very close to those for pure platinum (table Fig. III-3A), except for the {011} planes (0.2753 nm) that confirms, in our case, the formation of nanoalloy particles (Fig. III-4). In addition, two additional reflections at 0.2505 nm and 0.1643 nm can be respectively attributed to the {101} and {110} planes of the ZnO structure. This is not totally surprising as it is well known that zinc can easily oxidize to form ZnO. Due to their small size, we cannot exclude the formation of a thin ZnO oxide layer.

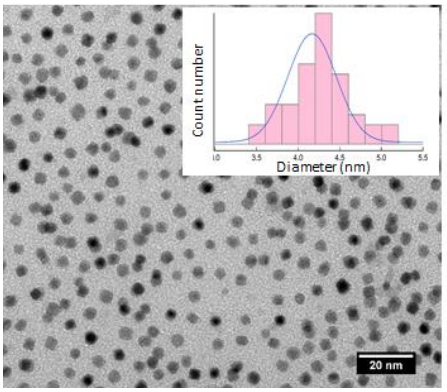

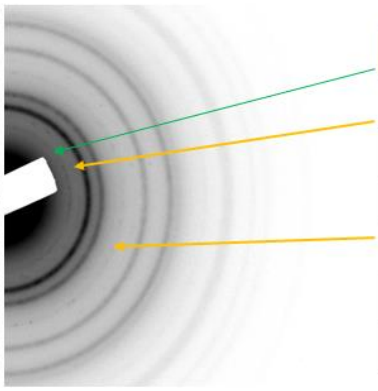

$d_{ICDD\ Pt_3Zn}$	$d_{ICDD\ ZnO}$	d_{exp}
0,2753	0,2814	0,2789
	0,2603	0,2505
0,2248	0,2476	0,2247
0,1947	0,1911	0,1968
	0,1625	0,1643
0,1376	0,1477	0,1389
0,1174	0,1378	0,1188

Figure III-4. ZnPt nanoparticles obtained at 350°C in oleic-acid/oleylamine mixture and the corresponding diffraction pattern.

The HRTEM images confirm the formation of crystallized PtZn nanoalloy (Fig. III-5). This is well illustrated in the calculated power spectra which has three reflections pairs labeled 1, 2, 3 and 4 (Fig. III-5a). The deduced distances d_1 = 0.222 nm and distorted by 5% d_2 = 0.236 nm ≈ d_3 = 0.233 nm correspond to the {111} reflection of the Pt *fcc* structure slightly higher than for bulk values (table Fig. III-3A). However, the faces characteristic of the platinum-zinc alloy can also be detected (Fig. III-5a and 5c). The deduced distances d_1 = 0.201 nm ≈ d_2 = 0.198 nm corresponding to the {002} and the d_3 = 0.275 nm ≈ d_4 = 0.280 nm characteristic of the {011} of the Pt_3Zn *fcc* structure. Pt lattice adaptation probably happens due to the difference in cohesion energy between platinum (5.84 eV/atom) and zinc (1.35 eV/atom), which means that platinum has a greater tendency to self-assemble. Thus, all other things being equal, it is the platinum structure that is the foundation for the growth of the alloy nanocrystals. It is worth

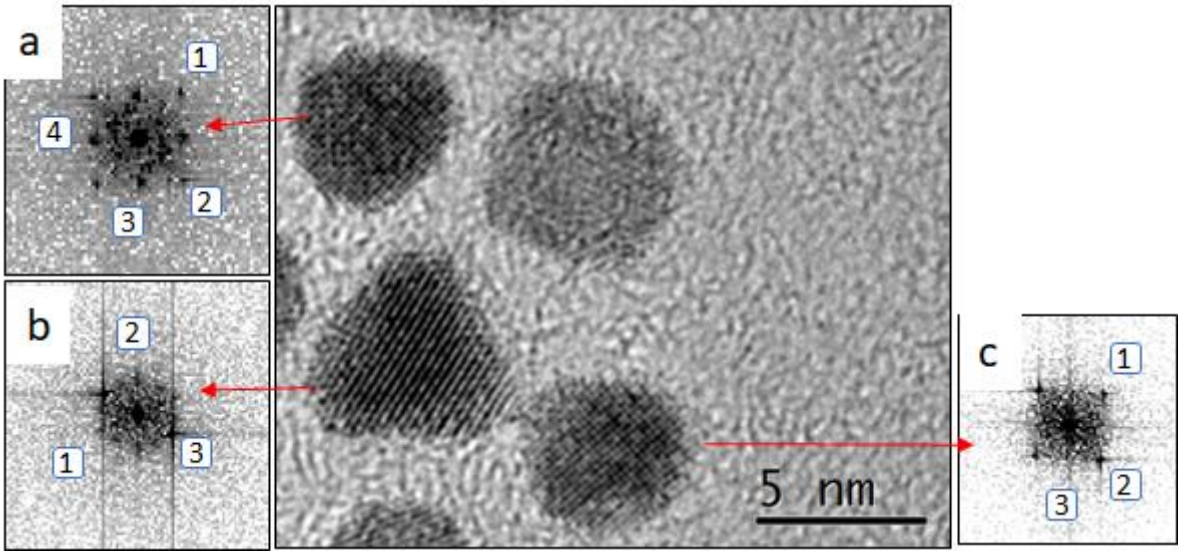

Figure III-5. HRTEM images of ZnPt nanoalloys and their Fast Fourier Transform

noting that the cohesive energy of zinc oxide (7.52 eV/atom) is even higher, which necessitates conducting an experiment in an inert gas atmosphere.

To get information on the NCs composition, energy dispersive spectroscopy (EDS) have been performed using a scanning electron microscope (SEM). Droplets of a solution containing our nanoparticles are deposited on a Si substrate and several different points in the sample are measured. If the measurement error does not exceed one percent, we consider such nanoparticles to be homogeneous in composition. Composition of all our NPs has been received by the method.

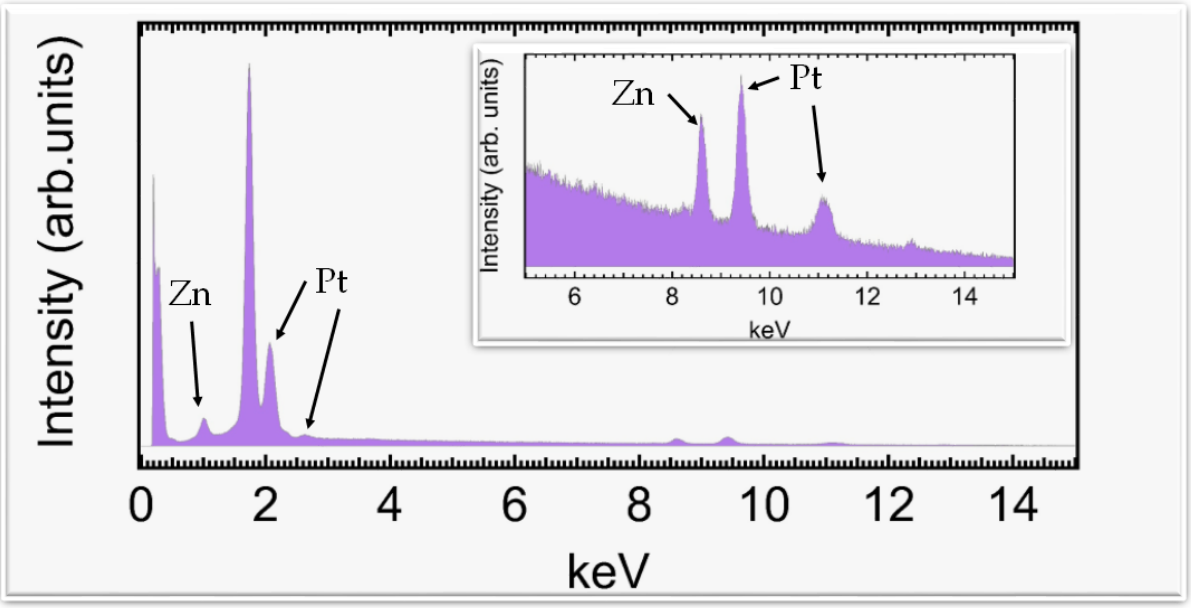

Figure III-6. ED spectrum of PtZn NPs deposited on Si wafer.

EDS measurements confirm the formation of ZnPt nanoalloys with a homogeneous composition of 15% Zn and 85% Pt (Fig. III-6). However, despite the fact that the synthesis using oleic acid, described in the literature [93], can be called successful (Fig. III-4), we have observed experimentally that oleic acid can induce a large variation in the diameter of nanoparticles (~6 nm) and also a heterogeneity in their composition (variation in 18 %). In a recent article, Yin et al. discuss different formations modes of platinum nanocrystals depending on the local ligand environment of the precursor.[171] In particular, they show that when $Pt(acac)_2$ is dissolved in primary amine, the amines coordinate with Pt^{2+} and replace $acac^-$ ligand to form $Pt(amine)_4(acac)_2$. While in presence of carboxylic acid (ex. oleic acid), acting as proton donor, $acac^-$ can react with protonated amine to form $Pt(amine)_4(carboxylate)_2$ complexes. A complete conversion of $Pt(acac)_2$ to $Pt(amine)_4(carboxylate)_2$ is obtained for an OA:$Pt(acac)_2$ ratio higher than 2 (OA:$Pt(acac)_2$ = 40 in the synthesis procedure[93]). Such effect can explain our observations when using acid oleic in presence of oleylamine. Indeed, it is well known that the complexation can modify the potential reduction of the precursor. Hence, considering the presence of different complexes in solution, successive reduction (depending on their reduction rate) can occur inducing heterogeneity during the nucleation steps. All the more, the formations modes of the nanocrystals can be different depending on the precursor. Indeed, they give evidence of a two steps mechanism for the formation of Pt NCs from the $Pt(amine)_4(acac)_2$ precursor : a slow reduction to form Pt(0) atoms and a fast autocatalytic surface growth. In presence of oleic acid, this latter step is not observed and the growth of NCs occurs much slower than that with $Pt(amine)_4(acac)_2$ precursor. These results are important as they illustrate the importance of the metal-ligand interactions both in the prenucleation stage as well on the crystal growth. It has to be noted that such effects can be more drastic for the formation of nanoalloys, where the two precursors have to be reduced simultaneously, even more so we cannot exclude such ligand-metal complexation for $Zn(acac)_2$.

To simplify the system and avoid the formation of competitive precursors, we considered the replacement of oleic acid by an equal amount of oleylamine in the synthesis. We observe experimentally a significant improvement: the dispersion in particle size is decreased and the composition homogeneity is restored. Therefore, the addition of the acid was excluded from the synthesis protocol in the following. In addition, different reaction parameters were studied in order to control the composition and morphology of the nanoalloys: loads of precursors, solution volume, additives ratio and synthesis time.

1.1.Shape Control: Role of the Solvent

In literature different kinds of reaction solvent, such as phenyl ether, benzyl ether, octyl ether, and 1-octadecene, were used in synthesis based on thermal decomposition.[172,173] In particular, some papers report, empirically, the effect of benzyl ether on the morphology.[93] To induce a shape control, phenyl ether and benzyl ether have been used as co-solvents with oleylamine. Both oleylamine and benzyl ether are mentioned in the literature to have a dual functional role: reducing agent and solvent.[173,174] In these experiments 0.02g of $Pt(acac)_2$ and of 0.0125g $Zn(acac)_2$ (corresponding to a molar ratio of 1:1) are solubilized in 3.9 ml OAm. 2.5 ml BE (12.6 mmol) or 2.0 ml PE (12.6 mmol) are added to the mixture and the solution is heated under reflux.

Small 3nm spherical Zn_xPt_{1-x} nanoalloys (with x=23%) are obtained in presence of phenyl ether ($(C_6H_5)_2O$) (Fig. III-7A) while benzyl ($(C_6H_5CH_2)_2O$), on the contrary, induces the formation of 4.7 nm cuboids nanocrystals. However, the composition is characterized by a lower Zn content (x=15%) Fig. III-7B). In this latter case, the size of the nanoparticles could vary from 4.7 to 8 nm. In all likelihood, the diameter of PtZn NPs depends on impurities present in the reaction atmosphere. Thus, in a series of a two identical experiments degazed for 10 minutes OAm under the flow of Ar (99.9 % purity) led to bigger NPs (8 nm in size) than OAm without pretreatment (Fig. III-7C). In such case more cubic NCs are obtained characterized by a Zn content of 17%.

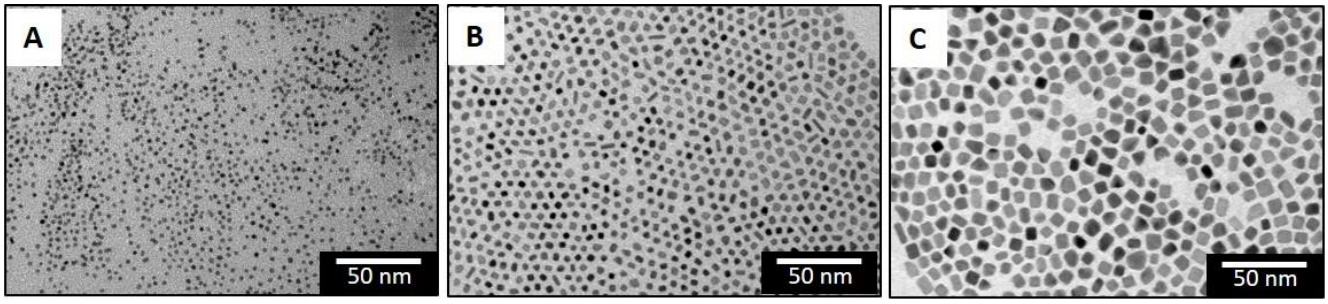

Figure III-7. ZnPt nanocrystals obtained under reflux at 350°C in oleylamine in presence of A) phenylether, B) benzylether without Ar pre-treatment and C) benzylether with Ar pre-treatment

Hence it is possible by considering different additive to induce a morphological control of the NCs. In particular, these results show that benzyl ether has a strong influence in the stabilization of cubic morphology. However, it seems that benzyl contributes to a decrease in the Zn incorporation. One explanation could be that it contributes to higher reductive environment in the chemical media that favour a control of the reduction of platinum precursor at lower temperature.[174] Indeed, as we consider a mixture of oleylamine (boiling point at 350°C) and

benzyl ether (298°C) we can have a reflux temperature slightly different that 350°C and thus a change in the nucleation of Zn and Pt monomer.

It has to be noted that the optimal synthesis time corresponds to 5 minutes of reaction. We observed experimentally that the extension of the synthesis time to 30 minutes (to 60 minutes) partially (completely) nullified the effect of ether on the particles and they were losing their cuboid shape. Such an extension of the synthesis time seems to lead to a kinetically stable product with a smaller particle size of 11.2 ± 2.7 (9.4 ± 2.1) nm and an inhomogeneous (28 % of Zn) composition (Fig. III-8).

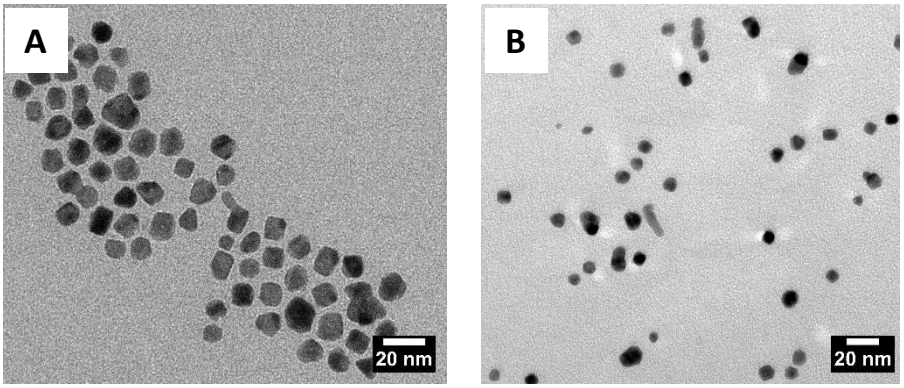

Figure III-8. PtZn nanocrtystals obtained at 350 °C in oleic acid/oleylamine mixture after 30 minutes (A) or after 60 minutes (B) of synthesis

1.2. Control of Composition: Load of Precursors

In order to control the composition, we considered different load of precursors in presence of benzyl ether. Thus, with the initial ratio of zinc salt to platinum salt as 1 : 9 (Fig. III-9A) well-defined 9 nm cubic nanoparticles with 5% zinc content are obtained at the output. On the contrary, a change in the ratio of precursors in favor of zinc (Zn : Pt = 2 : 1) resulted in three differently shaped groups of nanoparticles, namely, cuboid, quasi-spherical, and nanorods, which are very similar in shape to those which were obtained in the synthesis of pure ZnO (Fig. III-9B). [175] It seems from these results that cubic nanocrystals are favored in benzyl ether for rich Pt nanoalloys (Fig. III-9A and III-7C). However, we tried to make pure platinum nanocubes considering only $Pt(acac)_2$ precusor in a mixture of oleylamine and benzyl ether and no cubes were obtained. This observation confirms the synergetic effect on each other as already

observed previously. As a perspective, the synthesis of platinum in pure benzyl ether could be considered in the future.

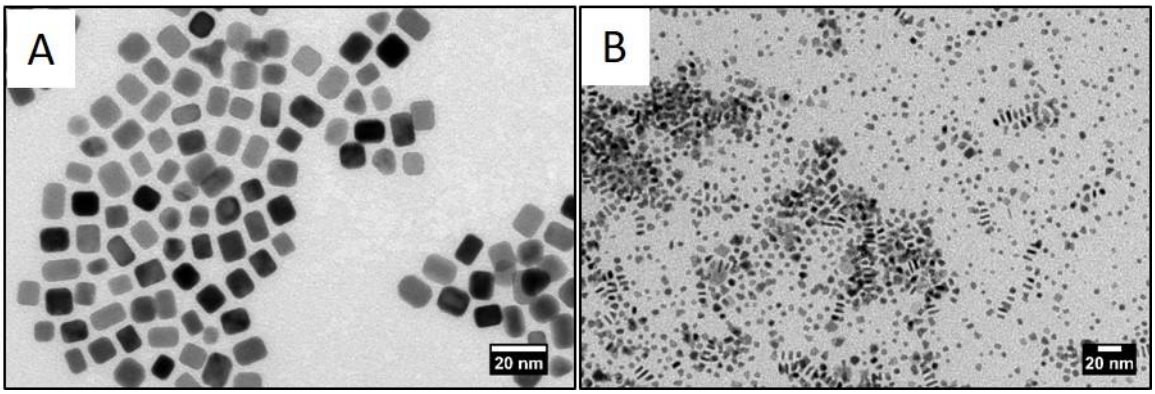

Figure III-9. Zn_xPt_{1-x}: Nanoalloys obtained in oleylamine/benzylether for different molar ratio of $Zn(acac)_2/Pt(acac)_2$ precursors (A) 1:9 and (B) 2:1

In the context of catalysis, it is important to produce stable catalysts both in context of its aging or under real catalytic process environment. Hence, we naturally look at the stability in time of the nanoalloys described above.

2. Stability (Aging)

An important aspect of the stability of nanoparticles is their aging. From the very beginning, we noticed that after several days cuboids PtZn particles change (Fig. III-10). Speaking exactly, one month after the synthesis PtZn NPs size decreased from 4.9 to 4.1 nm and the content of Zn dropped by 3.6 %. In addition, the NCs became more rounded.

Something similar for platinum alloys exists and has been well studied by an example of an alloy with cobalt, where during the oxidation of the nanoparticles cobalt moved to the surface

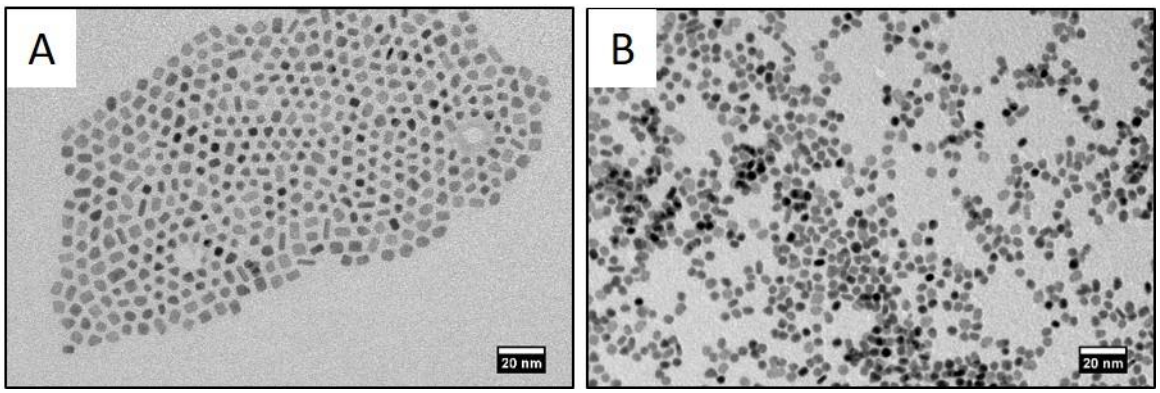

Figure III-10. Evolution of the 4.9 nm $Pt_{86}Zn_{14}$ nanoalloys as-synthesized (A) and after 31 days (B)

where its oxide was formed.[176] However, this phenomenon was of a reversible nature and the composition was restored in a hydrogen atmosphere, where cobalt atoms migrate back into the interior of the crystal and a monolayer of platinum is formed on the surface. In our case both the size and the proportion of zinc decrease as it is shown on the Fig. III-10 which implies the irreversibility of the transformation. Moreover, this effect is more drastic for the smaller nanocrystals (3 nm) with high Zn content (23%). We have observed that at a sufficiently high content of zinc in the nanoparticles (Fig. III-11), its oxide is not only washed out from the surface of the crystal but can also form a bizarre network after a month of storing the nanoparticles in toluene solution. This transformation implies two things. First, zinc oxide does not react with anything else (for example, CO_2) and does not form new compounds, since otherwise finding a zinc oxide network would be excluded. And the second is that the interaction between zinc oxide and an alloy on the surface of PtZn nanocrystals is a delicate balance between two crystalline phases which slowly moves towards segregation. HRTEM image spherical 3 nm PtZn NPs are presented on the Fig. III-11C and D. The deduced distances d_1 = 0.224 nm and d_2 = 0.194 nm correspond respectively to the {111} and {002} reflections of the Pt *fcc* structure. It seems, that in this case we are limited by the technique and not capable to detect the PtZn planes. In addition to the spherical NCs, ZnO network is observed (Fig. III-11B). The calculated power spectra exhibit a unique reflection pair (d=0.262 nm) corresponding to the {002} reflection of the hexagonal zincite structure (Fig. III-11D and 11E).

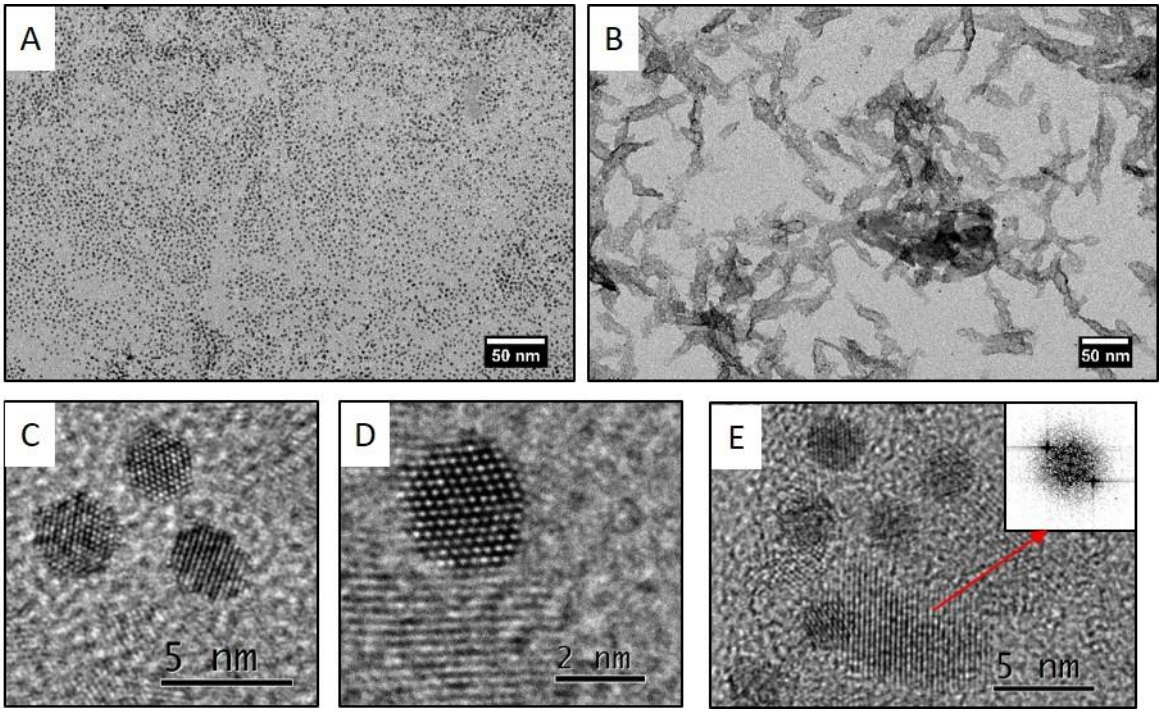

Figure III-11. 3nm spherical $Pt_{77}Zn_{23}$ naoalloys just after synthesis (A) and after one month aging (B). The HRTEM of the aged spherical NCs (C, D) and of the ZnO network (crystallized sheet) obtained with its corresponding FFT (D, E)

3. Conclusions

From all these results we can clearly see that the chemical syntheses appeared to be more complex to elaborate PtZn nanoalloys, as one might expected. The control of the nature of precursor is a key parameter to favor co-reduction, necessary to obtained solid solution. In this context, one difficulty consists in the fact that *in-situ* formation of intermediate complexes can occur in our systems. This can induce different reduction rate leading to inhomogeneous samples (size, shape, composition). In addition the different parameters we can play on to control the size, composition and shape are mostly interdependent. That explain the difficulty to simultaneously control the composition and shape or the size and composition. However considering different experimental conditions, we have successfully synthesized different composition nanoalloys. Small NCs (3 nm) with a Zn rich content (23%), nanocubes of different sizes (4.7 and 8 nm) with a similar composition of almost 15% of Zn and large nanocubes (9nm) with low Zn content (5%). We gave evidence that the stability of the nanoalloys depend on the Zn content. The less zinc there is, the more stable the NCs appear to be. We have to note that an enhancement of this effect with the size cannot be excluded as higher Zn content correspond to smaller size.

To go further in their surface characterization and their reactivity, we then focus our study on the PtZn nanocubes characterized by 14% of Zn (~5 nm) $\boldsymbol{Pt_{86}Zn_{14}}$ and 5% of Zn (9 nm) $\boldsymbol{Pt_{95}Zn_{5}}$. Or the PtZn quasi-spherical NPs characterized by 23% of Zn (~3 nm) $\boldsymbol{Pt_{77}Zn_{23}}$. For HRTEM experiments we used the cubic NPs obtained by using Ar pretreatment resulting in 14% of Zn content (8 nm) $\boldsymbol{Pt_{86}Zn_{14}}$.

Chapter IV. PtZn NPs by XPS: The Role of the Ligand

The key to a successful preparation of nanoparticles with a narrow distribution in size and shape is the presence of bulky and strongly binding surfactant molecules. Such an organic ligand shell produced on the metal surface helps to avoid agglomeration so that NP size is preserved. However, with a ligand-covered nanocrystal, the other side of the coin is the fact that the catalytic activity of nanoparticles usually tends to be significantly reduced due to the almost complete absence of accessible reaction sites. In this matter a "worst case" example is the thiol that is too strongly bound to the particle surface via a Metal-S bond.[177] Therefore, being between Charybdis and Scylla, it is extremely important to find ligands sufficiently bound to the particle to avoid coalescence, but sufficiently labile to let the access to the reactants. For such a procedure to be effective, it is necessary to clearly understand the nature of the metal-bound ligands. We will see in the following that X-ray photoelectron spectroscopy gives evidence that oleylamine on PtZn nanoparticles may be an excellent ligand of PtZn alloys, due to the nature of its bonding geometries.

1. X-ray Photoelectron Spectroscopy

Samples were prepared by repetitive dropwise addition of a concentrated nanoparticle solution onto Au film on Mica. The short time (~1 hour) between the synthesis and the sample load into the UHV chamber is important as it helps to minimize an influence of the solution on the nanoparticles.

The XPS experiments were carried out with a PHOIBOS 150 spectrometer from SPECS, equipped with a monochromatized source Al Kα of 1486.6 eV, and fitted with a delay line detector. The machine installed in LCPMR, is now part of the so-called "Surface" experimental platform of the Paris Institute of Physical and Theoretical Chemistry (IP2CT). The spectrometer bought a decade ago was recently upgraded (monochromatic source and detection) thanks to a grant from Agence Nationale de la Recherche, in the context of the NUMEN Project (**Nu**cleation, growth and reactivity of **ME**tallic and bimetallic **N**anocrystals, 2018-2022), which gathers together researchers from LCPMR (SU), MONARIS (SU) and CINaM (Marseille), who are all involved in the present study. The upgrade of the XPS setup was carried out from January of 2019, and several experimental slots were allowed to the study of the PtZn NC until late June.

All XPS experiments shown in the following pages were carried out with an X-ray source bandwidth of 600 meV (unfocussed mode), at a pass energy of 10 V, using a 7 mm slit. The overall experimental resolution is 640 meV. This setting is good trade-off between resolution and acquisition times. Acquisition times lasting tens of hours were used for certain core-levels like N 1s.

In the following, the photoemission experiments are presented and interpreted according to the logic that governed the actual conduct of the experiments. We first present the results for pure zinc NCs, then for zinc-platinum alloy NCs, from the lowest in zinc (5% atomic) to the highest (23%). The spectra presented are all those of fresh samples, produced in the oleylamine solution, then quickly washed with ethanol and introduced into the preparation chamber of the spectrometer. We then examine the chemical evolution of these NCs. We have had the opportunity to become aware of a phenomenon of ageing in the NC storage toluene solution, and we are addressing this issue in detail. Finally, we carry out heat treatments and gas exposures (in a CO *plus* O_2 mixture), similar to those carried out in the context of NAP-XPS.

The examination of the core levels gives highly valuable insights on the oxidation state of the surface (most specifically of the zinc atoms), on the oleylamine ligand chemical binding, on the possible presence of "hetero-species", that can be byproducts[171,178,179] of the reaction (water, hydrogen, imines etc.) or even contaminants (water, O_2, carboxylic acids etc.) resulting from exposure to air. However given the complex chemistry involved - two metals are involved with two very different oxophilicity - a full understanding of the mechanisms will need more extensive studies.

We first tried to synthesize the pure zinc and platinum NCs, to have significant *spectroscopic* elements of comparison with the alloyed NCs. If we succeeded for zinc (we produced zinc oxide NCs), we failed for pure platinum NCs, as the samples showed strong charging effects during the XPS experiments, making it difficult to interpret them. Fortunately, we will see that good approximants of pure platinum NCs are provided by very low zinc alloys, or aged particles. We will also see that the interpretation of binding energies, especially those of the components of the N 1s spectrum relative to oleylamine, will be carried out through surface chemistry experiments, specifically the adsorption of CO, or annealing in UHV.

The writing of a scientific article will necessarily involve a major overhaul of the material presented in this thesis, as the discourse will focus on the nature of the chemical bonds of the

amine head with the surface, and the role of interface water in this chemistry. In the meantime, we will explain how we have progressed, even if the path is tortuous.

2. Growth Mechanisms of Metallic Nanocrystals in Oleylamine

Before beginning any discussion on the surface chemistry of the NCs, it is important to recall which mechanisms are proposed in the literature leading to metal reduction, nucleation and growth in oleylamine. Concerning platinum, Xi Yin et al.[171] have studied the growth of NCs with UV-vis spectroscopy and MALDI-TOF mass spectrometry. Their main point is the replacement of the $acac^-$ ligands by the $R\text{-}NH_2$ ones, and then the further reaction of oleylamine with the freed acac to give several byproducts like amino ketones (via a condensation reaction). However detailed mechanisms are lacking for $Pt(acac)_2$.

On the other hand, the reduction of $Pd(acac)_2$ in a primary amine solvent has attracted more interest. We can cite for instance the DFT supported mechanism proposed by Carenco et al..[179,180] Pd is particularly interesting for our study, as like Pt, it has a strong dehydrogenation capacity of the primary amine solvent. In a paper published in 2012, Man, Brown and Wolf have proposed a mechanism for the formation of Pd^0 nanoparticles.[178] We reproduce here below in scheme IV-1 and 2 the two reaction schemes given in their paper. Detailed explanations are given in the paper.

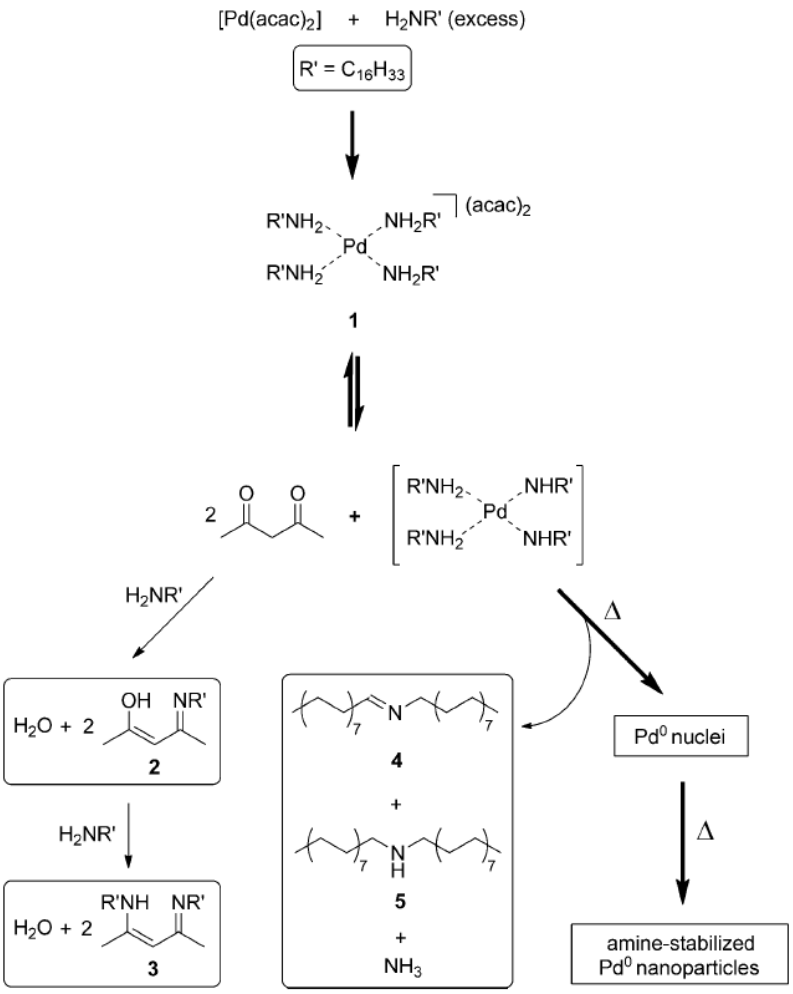

Scheme IV-2. Proposed mechanism for the formation of Pd^0 NPs from $[Pd(acac)_2]$ and a primary amine.

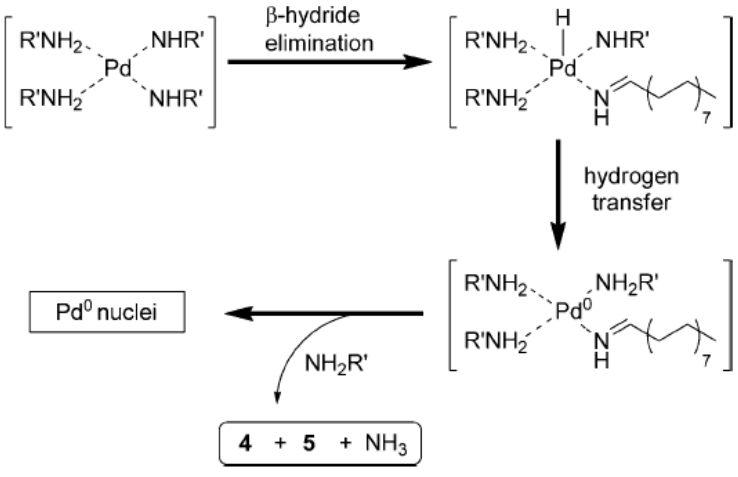

Scheme IV-1. Formation of Pd^0 by β-hydride elimination and hydrogen transfer.

Scheme IV-1 indicates several byproducts, all detected by solution ^{1}H NMR, that can be formed: water, ammonia, species 2 (a ketimine), species 3 (a diketimine), species 4 (an aldimine) and species 5 (a dialkylamine). The ketimine and diketimine species result from a condensation reaction between the primary amine and Hacac, giving water as the byproduct. The presence of water is important as we may see it by XPS (see below), and if it is dissociated on the NC surface, the hydroxyls may explain the so-called ionic bonding with a protonated amine head. Ammonia resulting from the complex reaction depicted in Scheme IV-2, can also react with the metallic surface to give H atoms (ammonia breaks down on a (553) Pt surface at 300 K, see [181]). These points are not addressed in the paper by Man et al. who do not consider surface reaction, and focus on the reduction process of the individual metallic atom.

Concerning photoemission, the alkylamine should appear at 399.4 e V (at the same position as the oleylamine R-NH_2), and the imines at 398.4 e V.[182] We shall see in the following that the two main components of the N 1s spectra are also at ~399.8 e V and 398.3 e V. The question to be raised is the following: are byproducts like diketimines bonded to the NC surface by some specific mechanism? Or is the oleylamine solvent the majority species around the particle. While we have no experimental evidence of the latter assertion, we will make this reasonable hypothesis.

3. Pure ZnO NPs Examined by XPS

Zinc NCs (characterized in a previous chapter) cannot set a good example of a successful catalysts synthesis: large (~15 nm), stuck together with a broad size distribution, these NCs do not represent much interest in the field of catalysis of CO oxidation. However, it is an interesting point to get a fundamental understanding of the state of the surface of PtZn nanoalloys obtained in exactly the same way as zinc oxide NCs. The Zn LMM and Zn $2p_{3/2}$ spectra are given in Fig. IV-1, while the O 1s, C 1s and N 1s are reproduced in Fig. IV-2. Due to a ~1 eV charging effect, all spectra are rigidly shifted in such a way that the C 1s main component (the dominantly sp^3 C tail of oleylamine) is at 284.8 eV. This procedure will be systematically applied in the following. Note that charging is unavoidable with a monochromatized source due to a weak emission of stray electrons (a flood gun will be installed in the next future).

The main information provided by XPS is that it is impossible to produce metallic zinc NCs. Zinc is completely oxidized under the present conditions of synthesis. This was observed by others.[168]

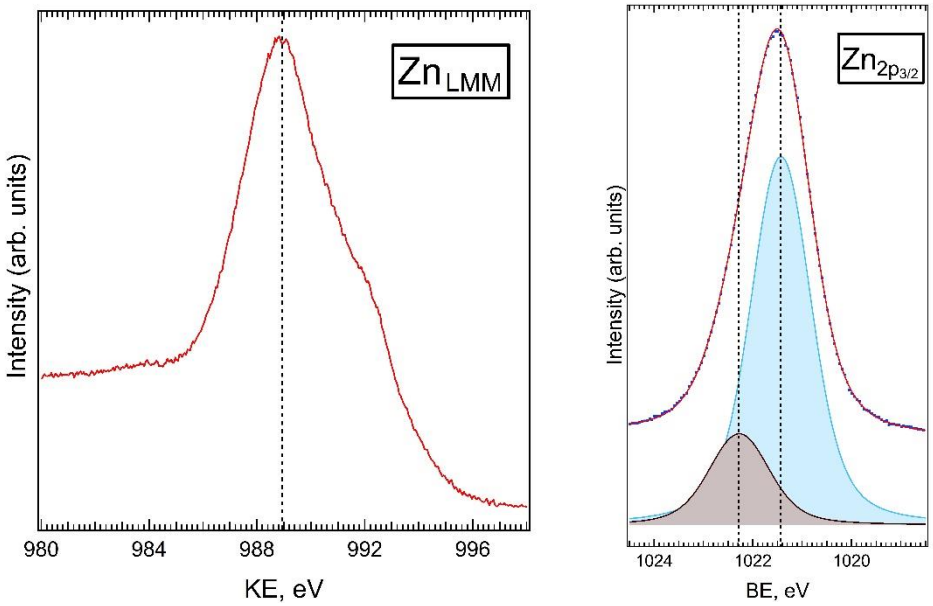

Figure IV-1. Zn Auger and $2p_{3/2}$ spectra of pure ZnO NPs. Monochromatized Al K_α source. The overall resolution is 640 meV.

As we see from the Auger Zn LMM spectrum, zinc is entirely represented by the Zn^{2+} component at a KE of 988.9 eV. The metallic Zn^0 with its characteristic peak at ~996 eV is

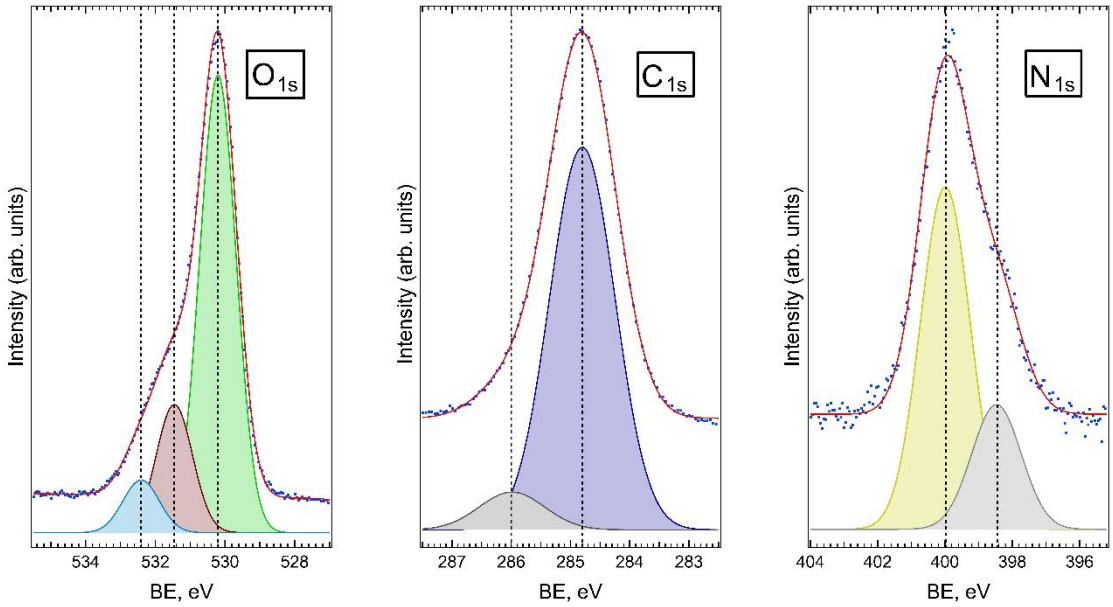

Figure IV-2. O1s, C1s and N1s Spectra of pure ZnO NCs. Monochromatized Al K_α source. The overall resolution is 640 meV.

completely absent. As we do not see a metallic core, the oxidation necessarily takes place during the synthesis from the Zn $acac_2$ precursor in oleylamine at 350°C.

In the present case we believe that water plays a prominent role in the production of zinc oxide. Water can be produced by a condensation reaction in the pot: the amines can react with the acetylacetone molecules (Hacac) to give water molecules and aminoketones,[171] ketimines and diketimines (see above).[178]

In order to adequately fit the Zn $2p_{3/2}$ spectrum two peaks are needed (Fig. IV-1). In the Zn $2p_{3/2}$ spectrum shown in Fig. IV-1, the main peak at 1021.4 eV corresponds to Zn^{2+}, in ZnO. The peak asymmetry to higher binding energy is accounted for by a smaller component at 530.2 eV corresponds to O^{2-} in ZnO lattice. Then come at higher binding energies the hydroxyls at 531.5 eV (surface hydroxylation is a common way to relax the ZnO surface) and adsorbed water at 532.4 eV.[138,139,145,183] The C 1s spectrum is composed of two peaks: apart from the main component at 284.8 eV (the C atoms of the tail), the peak at 286.0 eV most likely includes C-N from oleylamine (or its byproducts), and C-O bonds from contaminants.

In the N 1s spectrum we see two contributions. The major one at 400.0 eV is assigned to an intact R-NH_2 head weakly bound to or not directly in contact with ZnO. Therefore the observed component likely pertains to free head in a second oleylamine shell. The same observation will be made for the PtZn particles. The peak appearing at a lower binding energy, at 398.5 eV, is attributed to an oleylamine head having reacted with the ZnO surface. However the precise nature of the Zn-N bond remains elusive. Oleylamine is a *primary* amine that can lose one or two hydrogen atoms. The 398.5 eV component is also seen for primary/secondary amines that are dehydrogenated *once* on clean transition metal surfaces.[184] Then, Zn-NH-R moieties could form (the released H may react with ZnO to form a surface hydroxyl). Trioctylamine, a *tertiary amine*, bonded to a ZnO film has also a binding energy of 398.5 eV.[185] The same bonding type for primary and tertiary amines could only occur if the breaking of the N-C bond is as facile as the N-H one. A full decomposition of the amine head is also not excluded. N ions substituting O^{2-} ions in ZnO are found at this low binding energy.[186]

4. Bimetallic Nanoalloys Examined by XPS

To get a smooth transition from pure Pt nanoparticles to bimetallic alloys we have gradually increased the proportion of zinc in the crystals. We believe it allows us to better understand the

nature of the samples, and the bonding of the ligands around them. As we have noticed the loss of Zn during storage of the NCs in toluene, we have avoided the storage step and speeded up the transfer from the "pot" to the XPS analysis chamber. The samples were all measured by XPS immediately (within hours) after they were synthesized.

1. $Pt_{95}Zn_5$ (9 nm)

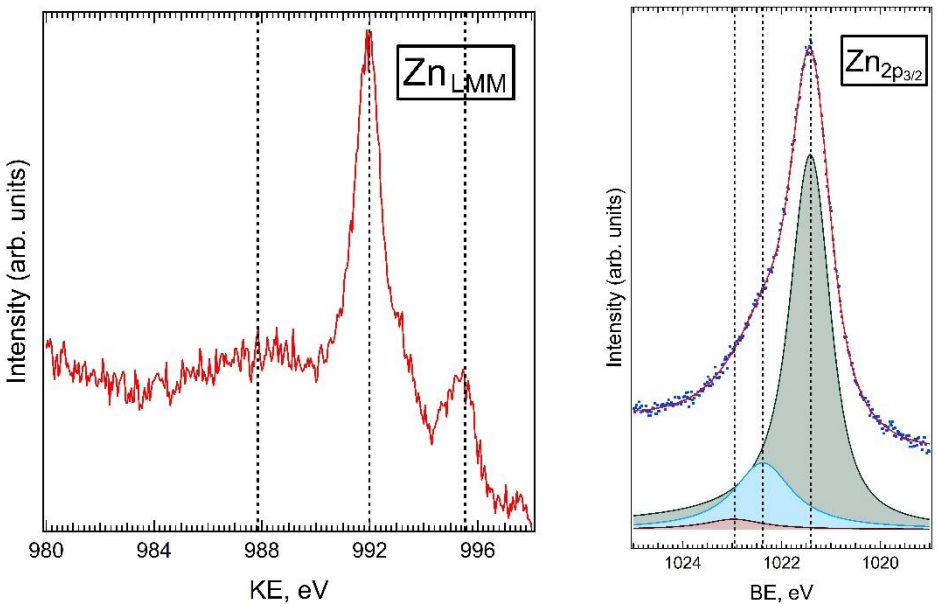

Figure IV-3. Zn Auger and $2p_{3/2}$ spectra of fresh $Pt_{95}Zn_5$ NPs

In this part, we will present the XPS analysis of the nanoparticles with the lowest zinc content, i.e. of 5 %. Accordingly, at that low Zn content the surface chemistry should be dominated by platinum. If some zinc atoms are nevertheless present on the surface of the NCs, they must be in an oxidized state. The Zn LMM and Zn 2p spectra are shown in Fig. IV-3. The O 1s, C 1s and N 1s peaks are shown in Fig. IV-5. Charging is corrected as indicated before.

The Auger spectrum (Fig. IV-3) suggests unambiguously that only a small fraction of Zn metal is in a +2 oxidation state (note the small bump at ~988 eV). In fact, they are mostly present as metallic Zn (Zn^0) as shown by the strong peaks at 992 and 995.5 eV.[187] The same is true for the Zn 2p (Fig. IV-3) spectrum where the main component lies at 1021.4 eV.[90,183] The absence of noticeable ZnO signal suggests that metallic Zn is protected against oxidation. Therefore zinc is located inside the particles away from the surface, in a metallic state, and only a fraction of it in an oxidized state is at the surface. *When one considers that using exactly the same fabrication conditions with $Zn(acac)_2$ alone we got only ZnO, the fact that XPS shows without any ambiguity that an alloy is formed, with Zn in a metallic sate, is a major finding.* The

presence of $Pt(acac)_2$ prevents Zn from being fully oxidized. It is not completely clear whether some Zn atoms are oxidized during the preparation, or afterwards due to exposure in air.

Although the contribution of the Zn^{2+} ions is small in the Zn LMM and Zn $2p_{3/2}$ spectra, the O 1s spectrum is dominated by the contribution of its oxide. However, the peaks do not coincide with those of the Zn NC, being shifted by about +1.2 eV. The reason for it is likely a Fermi level shift that will be addressed in the next section. The peak at 531.3 eV can be attributed to O^{2-} in ZnO and the component at 532.4 eV to hydroxyls or to carbonates (or related compounds).[188] The last peak at 533.6 eV has been assigned to adsorbed molecular water.[188]

Now if we consider a platinum (or a Pt-rich) surface, one should expect a (sub-) monolayer of chemisorbed O atoms, or a (sub-)monolayer of hydroxyls at 529.6 eV and 530.5 eV,[189] respectively. We cannot detect them clearly due to the width and intensity of the 531.3 eV peak. Molecular water on (hydroxyl covered) Pt(111) is found between 531.1 eV (the water layer in contact with the surface) and 532.4 eV (the water overlayer).[189] Molecular water on the Pt areas can also contribute to the 532.4 peak, we have already attributed to OHs on ZnO.

The N 1s spectrum is fitted with four contributions. As for Zn NCs, the component at 399.7 eV corresponds to the free amine head ($R\text{-}NH_2$), having no or little contact with the particle, for instance being interdigitated in the first oleylamine ligand shell. We exclude any amine head datively bonded to platinum (or Pt-rich) areas, although molecular adsorption at cryogenic temperatures gives also a component at that precise energy.[184] In fact, primary amines such methylamine are prone to dissociate on Pt(111) once the temperature is raised. A thermally programmed desorption experiment[190] for methylamine on Pt(111) shows that H_2 and HCN desorb at temperatures below the fabrication temperature of 620 K. An infrared spectroscopy study shows also that the methylamine dosed Pt(111) surface has methylamine adsorbed intact at 84 K and remains so until 300 K. Above 350 K methylamine yields aminomethylidyne (CNH_2) as a stable surface intermediate.[191]

The 401.2 eV and 397.6 eV components that are not seen in the Zn sample, can be attributed straightforwardly to oleylamine bonded to Pt (or Pt-rich) surfaces. The component at 398.5 eV is seen both in Zn NCs and the present alloy. However, we shall see it corresponds to a specific bonding geometry of oleylamine to platinum. The ambiguity will be totally resolved by an experiment where the particles will be exposed to CO at room temperature.

Let us consider the component at 401.2 eV, specific of the alloy. This binding energy is in the range of amine heads making acceptor hydrogen bonds with surface hydroxyls,[192–196] and also

not too far from that of protonated amines (R-NH_3^+) seen at 401.6 eV.[197,198] For example, Nicklin et al. have found a component NH_3^+ at BE of 401.7 eV in adsorbed l-alanine on Ni(111).[198] At the moment it is not easy to decide between the two options. However, if we assume a "wet" Pt/OAm interface, where HO^- ions are present, the protonated amine head hypothesis is becoming credible. Remarkably, the monolayers of hexadecylamine and dodecylamine self-assembled on Au(111) exhibits a component at 401.4 eV[199] (Au $4f_{7/2}$ at 84.0 eV), interpreted as a protonated head making a ionic bond with a surface hydroxide ion.

Two other strong components are found at lower BEs, at 398.4 and 397.6 eV. We shall consider only the attachment of the molecule to platinum. We can first consider that the platinum surface is "dry". Such binding energy shifts are also reported for stepwise primary amines decomposed on a nickel surface in UHV conditions.[184] Then the component at 398.4 eV and at 397.6 eV can be attributed to amine heads having lost one H (R-NH-Pt) and two H atoms (R-N<Pt) respectively. A linear dependence in the BE shift on the number of nearest-neighbor H atoms, of about 1 eV per H is known in the literature.[200]

The interpretation here above relies on data from UHV surface chemistry. The question is whether this is applicable to the present case. Although all NCs growth conditions imply the oleylamine solvent environment, the process (see the byproducts in Ref. [178]) suggests that water

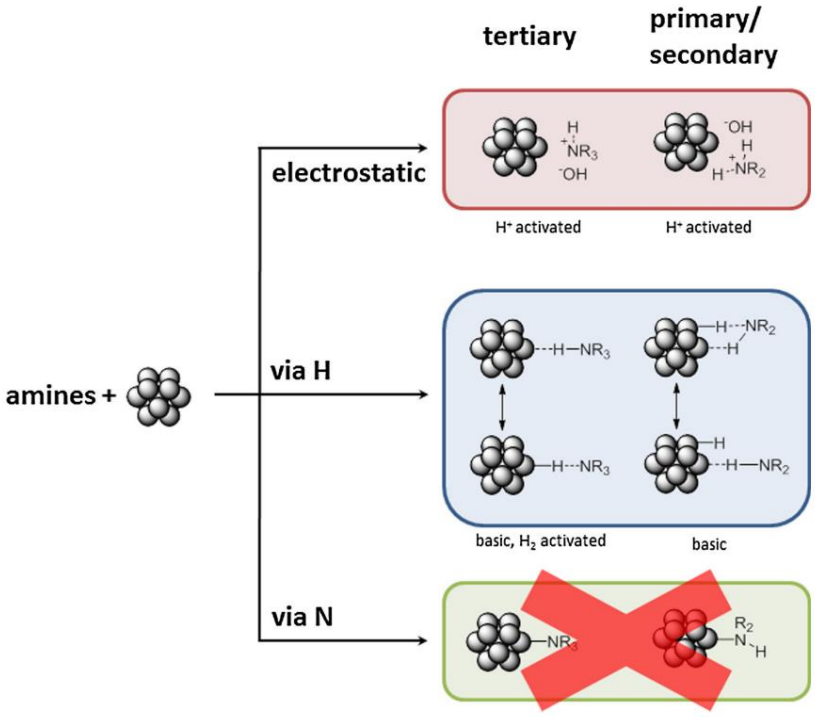

Figure IV-4. Potential binding modes for amine ligands to the NPs surface (from ref[177]). In our interpretation of the N 1s spectra, the protonated amine (R-NH_2^+) should appear at 401.2 eV, the H acceptor/H donor R-NH_2 head at 398.4 eV, and the single H-donor R-NH_2 head at 397.6 eV. We exclude the presence of datively bonded amines, considering the fabrication temperatures.

may be present. There are also hints in the O 1s spectrum of Fig. IV-5 that molecular water is present around the particle. Then, water could be dissociated at the metal surface, and Pt-H and HO^- species could be present (as in the case of the Au(111) surface). Ammonia, another possible byproduct, could also provide H atoms after dissociation[181] on the Pt surfaces. The presence of H atoms and hydroxyls (hydroxide ions) will have a considerable role in the binding of oleylamine at the NC surface. In this context, Wand and coworkers [177] proposed recently the following bonding configurations for amines on H covered pure Pt NPs. We believe that this configurations are applicable even in the case of PtZn alloys.

They propose that primary or secondary amines bond via an electrostatic interaction between surface HO^- and protonated heads $R\text{-}NH_3^+$ (see Fig. IV-4). This situation corresponds also to the case of the Au(111) surface.[199] This should correspond to the peak at 401.2 eV. Wand and colleagues propose two other bonding geometries, see Fig. IV-4**,** where H-bonds between the amine and the Pt surface, or between Pt-H and the amine head play a major role. Typically, the amine could donate one H to the platinum surface, or alternately establish a double bond, by donating one H to Pt, and accepting one H from a Pt-H moiety. When the amine donates a H to platinum the N 1s BE will decrease with respect to free head.[192] Conversely when the amine

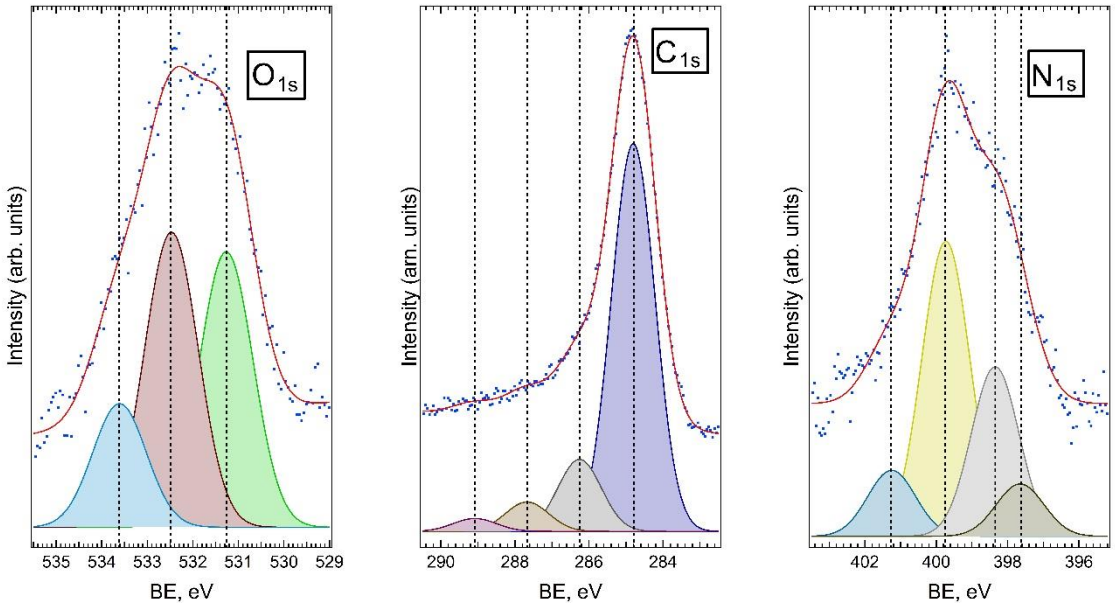

Figure IV-5. O1s, C1s and N1s spectra of fresh $Pt_{95}Zn_5$NPs

makes an acceptor H bond with a Pt-H moiety, the N 1s BE increases. The low binding energy component at 397.6 eV may be attributed to a Pt….H-NH-R configuration (…. symbolizes the H bond). When the amine makes both a donor and an acceptor bond the binding energy should be found at 398.4 eV, half way between that of the former configuration and that of the free amine head.

Once the presence of molecular water is ascertained at the contact surface between the metallic particle and the ligand shell, Wand's model is the only applicable one. It remains to give a sound theoretical proof that acceptor/donor H-bonds give rise to the two components at 398.4 eV and 397.6 eV. Ab initio core-level spectroscopy in the framework of DFT theory could answer the question.[201] The fact that the observed binding energies are equal to those of stepwise dehydrogenated amines on clean metals in UHV (the "dry") may be only a mere coincidence. In the following, we shall see, using the CO molecule as a probe, that Wand's model seems appropriate to the present situation.

2. $Pt_{86}Zn_{14}$ (5 nm)

If one increases the zinc content to 14%, then we see a striking differences between in the Zn LMM and Zn 2p spectra with respect to the $Pt_{95}Zn_5$ NC case (Fig. IV-6). Here, a majority part of the zinc atoms is in the oxidized form, as shown by the LMM peak at 987.9 eV. As discussed before, Zn^0 appears at kinetic energies of 991.8 and 995.4 eV in the Auger spectrum.

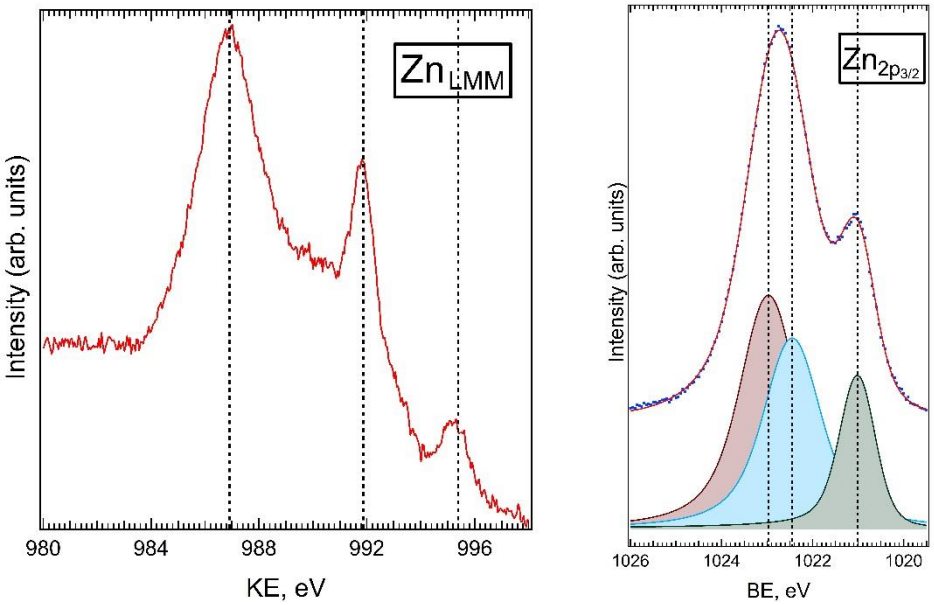

Figure IV-6. Zn Auger and $2p_{3/2}$ spectra of fresh $Pt_{86}Zn_{14}$ NPs

The Zn $2p_{3/2}$ spectrum exhibits also components in the 1022.5-1023.0 eV range, clearly distinct from the Zn^0 component at 1021.0 eV. This binding energy shift of ~1.2 eV is very surprising, as it is commonly accepted that Zn 2p XPS peak positions are nearly identical in Zn metal and ZnO, which makes the Auger Zn LMM spectrum the only practical way to distinguish between the metal and its oxidized forms. These coincidence in the Zn 2p BEs for the reduced and oxidized states of zinc is theoretically explained by Rössler et al..[202] In fact, the sum of initial and final state effects is *accidentally* the same for the two systems though the individual contributions differ quite significantly: the initial and final state shifts amount to +2.4 and -5.1

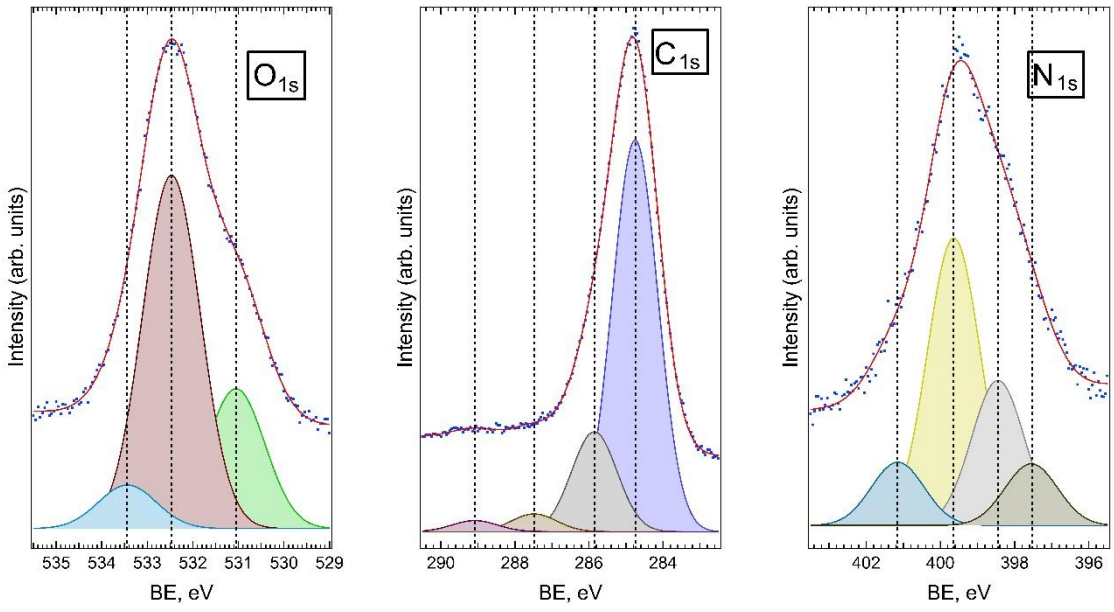

Figure IV-7. O1s, C1s and N1s spectra of fresh $Pt_{86}Zn_{14}$ NPs

eV for Zn metal vs. - 2.1 and -1.0 eV for ZnO. To account for this large BE splitting displayed in Fig. IV-6, one must consider a Fermi level shift, pushing rigidly all core-level values, *including the components in the O 1s spectrum*, to higher binding energy by about 1.2 eV. In other terms, ZnO (whose gap is 3.3 eV) is *more n-doped* than in the case of the Zn NCs. This could be due to Pt doping of ZnO.[203] Calculations show that Pt doping decreases the oxygen vacancy formation energy in ZnO, and a higher concentration of vacancies means more electrons in the conduction band. Other physical phenomena could be called upon, such as a downward band bending[188] at the surface of the ZnO material.

Let us now discuss the O 1s spectrum (Fig. IV-7). The green component at 531.0 eV can be attributed to O^{2-} ions ZnO (normally at 539.8 eV) because of the Fermi level rigid shift we have already talked about. Compared to the $Pt_{95}Zn_5$ cube composition, the $Pt_{86}Zn_{14}$ cuboids exhibit a marked increase in the O 1s region at 532.4 eV, which should be attributed to the additional formation of zinc hydroxyls. This may be due to the production of active hydrogen by water splitting on Pt. Note the presence of a peak at 533.4 eV attributable to water, as in the case of $Pt_{95}Zn_5$.

The N 1s spectrum still presents a strong (yellow) peak at ~399.8 eV we attribute to free amine heads, as in the other samples, Zn and $Pt_{95}Zn_5$. What is much more interesting is the fact that the components interpretable in the framework of Wand's model of amine bonding on Pt are still there at 401.2 (ionic bonding), 398.5 (acceptor-donor H bond) and 397.6 eV (donor bond), despite the higher Zn content in the NC (14%) than in the $Pt_{95}Zn_5$ sample.

3. $Pt_{77}Zn_{23}$ (3 nm)

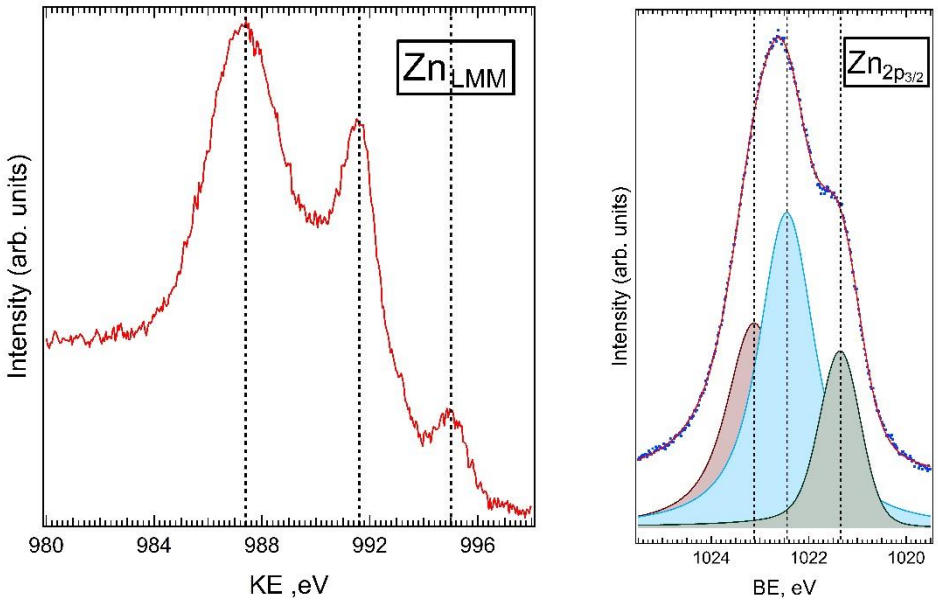

Figure IV-8. Zn Auger and $2p_{3/2}$ spectra of fresh $Pt_{77}Zn_{23}$ NPs

Here we will show the results on the quasi-spherical NPs where the influence of Zn on the spectra is the most pronounced, because it corresponds the highest zinc content in the series.

The Zn spectra (Auger and Zn $2p_{3/2}$, Fig. IV-8) are similar to those of particles having a lower zinc content. We only see a larger proportion of oxidized zinc, which is a logical outcome. The N 1s spectrum presents the same components as in the preceding samples, with a very similar distribution. This is however an information of paramount importance. If the $Pt_{95}Zn_5$ sample is

practically an extrapolation to the pure Pt NC, then this means that oleylamine bonds preferentially to platinum surfaces even in high zinc content NCs.

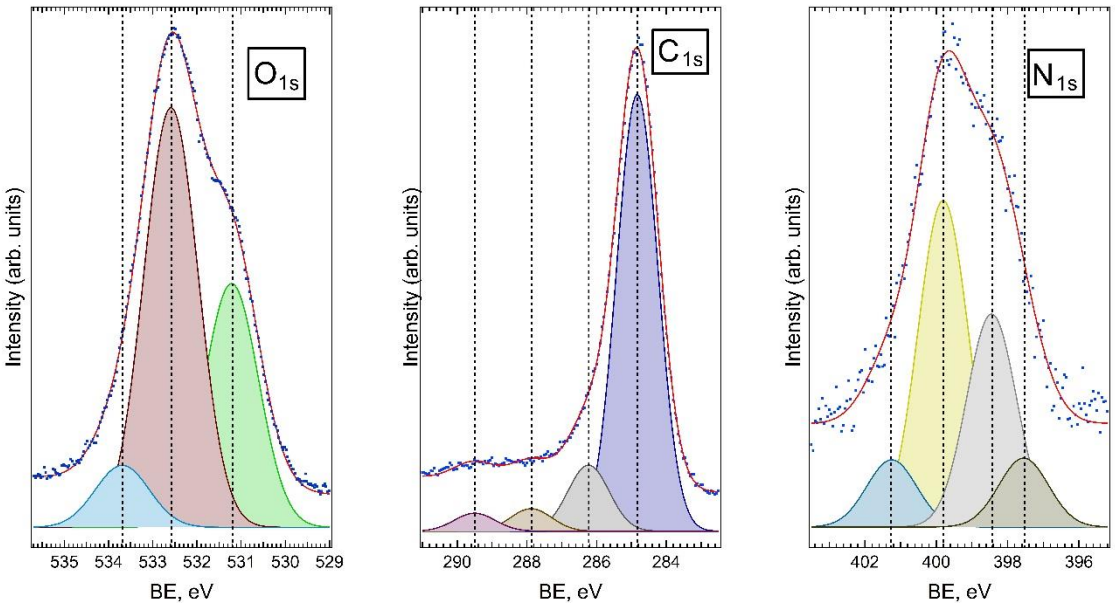

Figure IV-9. O1s, C1s and N1s spectra of fresh $Pt_{77}Zn_{23}$ NPs

3. $Pt_{89}Zn_{11}$ (4.5 nm)

Nanoparticles prepared in the same way as $Pt_{86}Zn_{14}$ from the earlier part and left storing in the toluene solution were analyzed by XPS. Preliminary tests by SEM showed that after 2 month storage the Zn portion in the aged NCs decreased by 3%. Which is in agreement with XPS results shown below (Fig. IV-10). The particularly telling Auger spectrum still exhibits Zn^{2+}

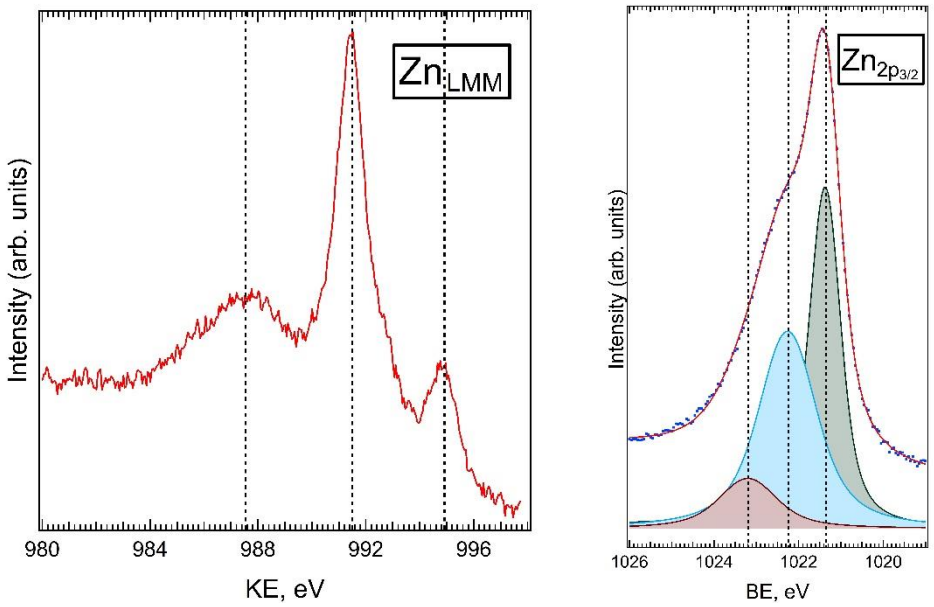

Figure IV-10. Zn Auger and $2p_{3/2}$ spectra of aged $Pt_{89}Zn_{11}$ NPs

contribution (987.6 eV), along with metallic peaks at 991.5 and 994.9 eV. However the relation to the total amount of Zn (Zn^{2+}/Zn_{total}) is more modest than for the fresh NPs. The same true for

the Zn 2p spectrum where now Zn^0 emission (1021.4 eV) dominates over Zn^{2+} (1022.3 and 1023.2 eV). This phenomenon will be discussed further below in the section on the aging of NPs.

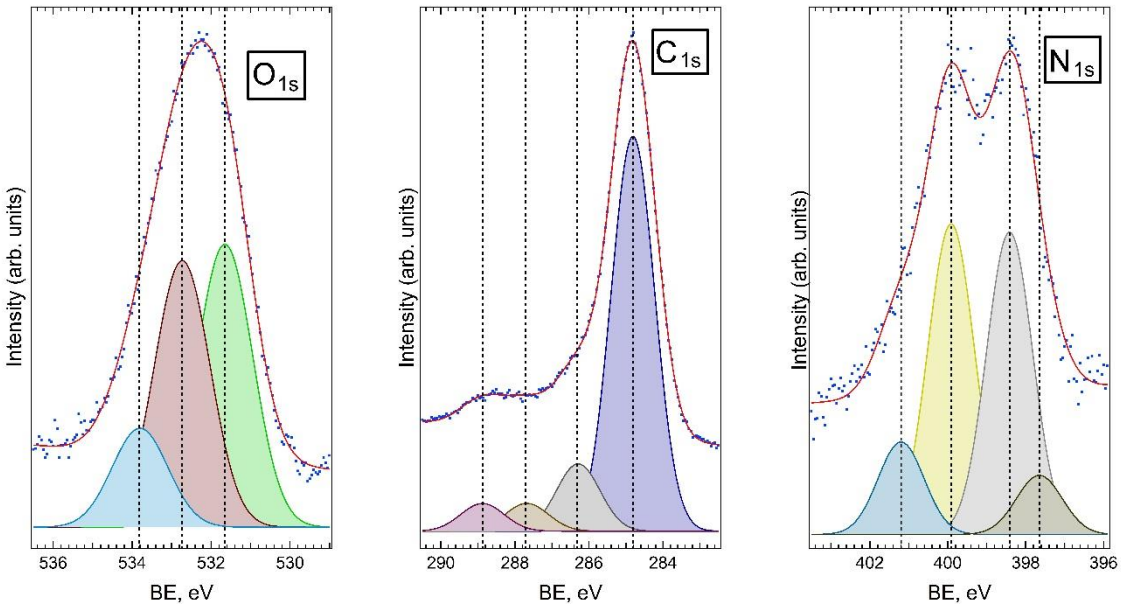

Figure IV-11. O1s, C1s and N1s spectra of aged $Pt_{89}Zn_{11}$ NPs

5. Aging of PtZn NPs in Toluene: a Zn^{2+} Free NC that Proves Water is Present

The $Pt_{86}Zn_{14}$ (5 nm) nanoparticles shown in the previous chapter were analyzed by XPS after 4 days storage in a toluene solution, and then washed in ethanol prior to XPS analysis. In Fig. IV-12 we give the Zn LMM and Zn $2p_{3/2}$ spectra, and in Fig. IV-13 the O 1s spectrum. The fresh sample spectra are also reported for the sake of comparison. All spectra are corrected from charging.

The Zn spectra have changed dramatically after a storage of 4 days in the toluene solution. As we see from the Auger spectrum, zinc is only metallic (Zn^0). The Zn $2p_{3/2}$ spectrum confirms this observation.

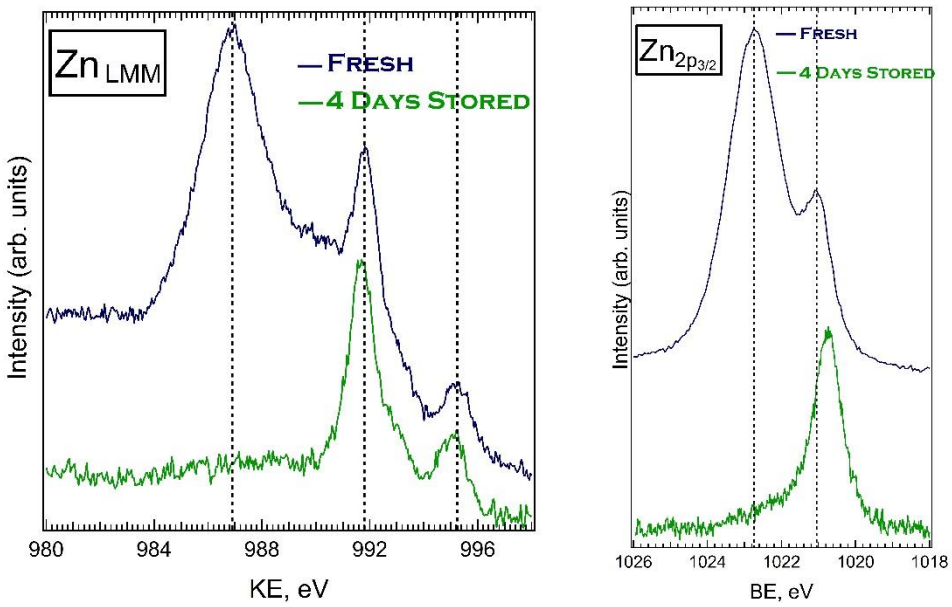

Figure IV-12. Zn Auger and Zn $2p_{3/2}$ spectra of $Pt_{86}Zn_{14}$ NPs fresh (in black) and aged and washed in EtOH (in green)

We have measured the ratios Zn $2p_{3/2}$/Pt $4f_{7/2}$ = 0.56 (0.08) and the O 1s/Pt $4f_{7/2}$ = 0.76 (0.79) of the fresh (aged) samples. Qualitatively, this means that the aged (and then washed out) NCs have undergone a strong loss of zinc (this was already suggested by the elimination of the Zn^{2+} component in the Zn Auger spectrum).

However, the O 1s content is about the same. This means that the oxygenated species present on the aged alloy NC are not related to ZnO nor to hydroxylated ZnO. We find now a single narrow peak at 532.5 eV in Fig. IV-13. *The presence of oxidized zinc had somewhat obscured the picture in the previous discussions. Now that zinc oxide is fully eliminated, we are more confident to attribute the main peak at 532.5 eV to molecular water confined by the ligands around the NC,* in agreement with Ref. [189]. The smaller shoulder at 530.5 eV is attributed to

OH species[189] adsorbed on the platinum (or Pt-rich) surface of the NC. Note the complete absence of chemisorbed oxygen that should be found at 529.6 eV.[189] Therefore the aged NC, because it is zinc oxide free, gives us strong hints that the "platinum" NC surface is "wet". This makes the application of the Wand's model much more credible. The N 1s of the aged NC is also given in Fig. IV-13. Due to a less effective washing in ethanol than for the fresh NC, the R-NH_2 component at 399.8 eV tends to overwhelm the contributions of the other components. Nevertheless, the ionic bonding and the H bonding components must be include to obtain a good fit.

The "peeling" of the zinc oxide film in toluene is not well understood. It may be related to the weak bonding of ZnO films on platinum, and their dewetting, as discussed for the monolayer

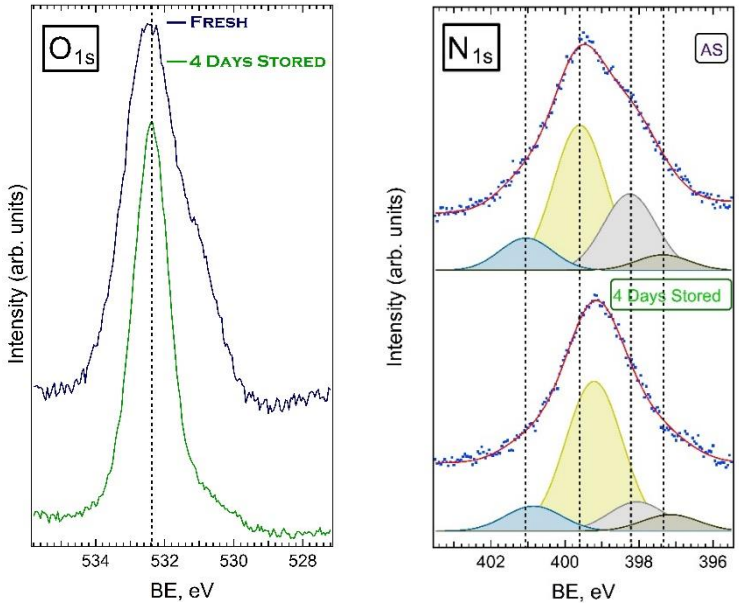

Figure IV-13. O1s spectra of $Pt_{86}Zn_{14}$ NPs fresh (in black) and aged (in green). Monochromatized Al K_α source. The overall resolution is 640 meV. The N 1s spectrum of the fresh and aged sample is also shown. The washing in ethanol was less effective for the aged NC than for the fresh one, hence the higher intensity of the R-NH_2 component.

ZnO/Pt(111) system. If films thicker than a monolayer are concerned, we know from STM, they are not prone to de-wetting. Thus other mechanisms should be called upon. In a context of wet chemistry, one could think to the gradual transformation of ZnO into its hydroxide $Zn(OH)_2$. Zinc hydroxide is tridimensional and poorly soluble. Then one could imagine a delamination process of the latter, taking the habit of a brucite-like structure. Formation of 2D layers of ZnO and of $Zn(OH)_2$ are reported in the literature.[204]

Chapter V. CO Oxidation: HRTEM and XPS

1. HRTEM

Carbon monoxide oxidation has attracted a great interest due to its importance in various industrial and environmental applications, and it has also become a benchmark reaction for examining the activity of heterogeneous catalysts.

As we have already shown in Chapter III, HRTEM is a powerful tool that allows to directly visualize the atomic structure of the sample. In this part, we use the capabilities of the microscope in order to follow the evolution of the PtZn NCs under oxygen or mixed oxygen with carbon monoxide atmosphere at room temperature. We would specifically like to underscore the valuable contribution of Suzanne Giorgio from CiNAM in Marseille to the present part of a research.

Experimental Details:

The ETEM microscope is a standard 300 kV microscope (Jeol 3010) equiped with two pole pieces, easy to change. The pole piece with a Cs = 0,6 mm gives a resolution of 0.17 nm, the pole piece with a Cs = 1,4 nm gives a resolution of 0.21 nm and allows the introduction of the environmental sample holder in the column. The environmental sample holder is schematically drawn in Fig. V-1. The sample (powder catalysts) is deposited on the heating wire made of W-Re. The heating wire is isolated from the grids by an insulator ceramic. The cell is closed by two copper discs where seven holes have been drilled, which are pre-covered by amorphous carbon films (E10 nm), located inside the cell. The sealing of the cell towards the vacuum of the TEM column is provided by the help of viton O-rings. Before insertion of the sample holder in the microscope, the sealing is tested ex situ until 200 mbar. The electrical connections for the heating wire and both tubes for gas circulation are included in the sample holder. It is important to note that owing to the small dimensions of the cell, it is very delicate to insert both copper discs perfectly centered and the heating wire supported on a micro-fabricated ceramic, without breaking the carbon films. The pumping into the sample holder is performed by a turbomolecular pump (150 $L*s^{-1}$). The small diameter of the connecting tubes, together with even smaller tubes inside the cell, dramatically limits the pumping rate. Then, without gas circulation, the actual pressure in the sample holder was not accurately known since the measurement corresponds to the entrance of the pump. In order to improve the pressure

measurements in the E-cell, we have connected a vacuum gauge at the exit of the E-cell. The pressure at the exit of the E-cell without gas is about 3 x 10^{-2} Pa.

The sample holder is a reactor closed by two carbon windows and it can be used in a standard TEM microscope (JEOL 3010). For ETEM observations, at a pressure lower than 10 mbar and at varying temperature between RT and 350 °C, the large gap pole pieces allows a resolution

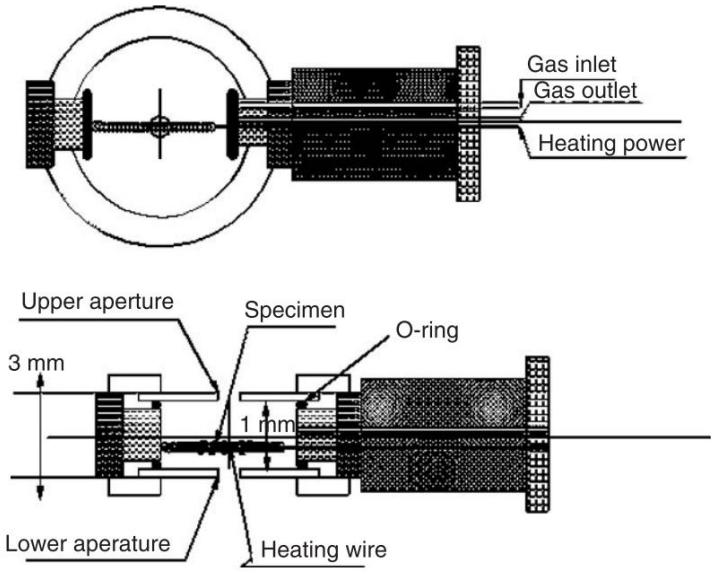

Figure V-1. E-cell heating holder in top and profile view.

of 0.21 nm. The images are recorded with a CCD camera and the adjustments minimize the effect of the electron beam. The well- known effect of quasi melting due to the electron irradiation15 is never observed in these conditions. The PtZn particles used in the present study are dispersed in ethanol on a microscope grid covered with carbon. They were first observed in standard conditions in the vacuum of the microscope (10^{-5} Pa).

$Pt_{86}Zn_{14}$ (8nm)

NPs, fully characterized in Chapter III and IV were analyzed after a 2-month storage in toluene solution, after most of the transformation has been completed. Considering what was said in the previous chapter regarding the aging process of the PtZn nanoparticles, where after 4 days

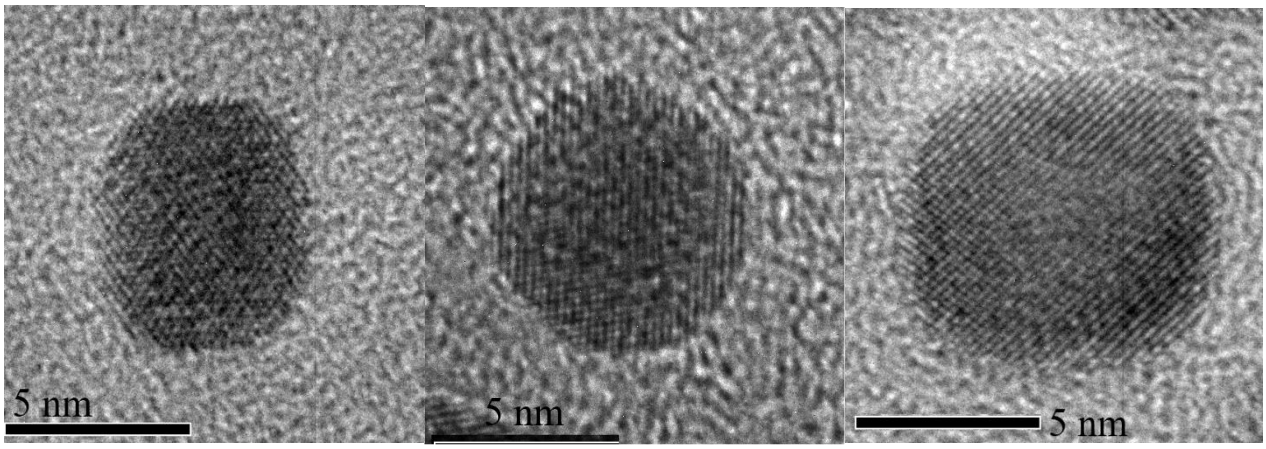

Figure V-2. HRTEM of ZnPt nanoalloys after aging. All the particles present a core shell structure with a well ordered shell and a disordered core

storage in toluene solution the amount of Zn^{2+} contribution dropped to almost zero, in combination with NCs images obtained by HRTEM (Fig. V-2), in which we observe the *fcc* shell of platinum and the distorted core, we can make a conclusion, which, in principle, as suggested from the XPS results is self-evident: the concentration gradient of zinc increases from the surface to the center of the PtZn nanoparticle, the core itself is a Pt_3Zn structure (was revealed by characteristic reflection pair of {011} planes in Chapter III), from which during the aging process zinc atoms are pulled out by oxygen molecules.

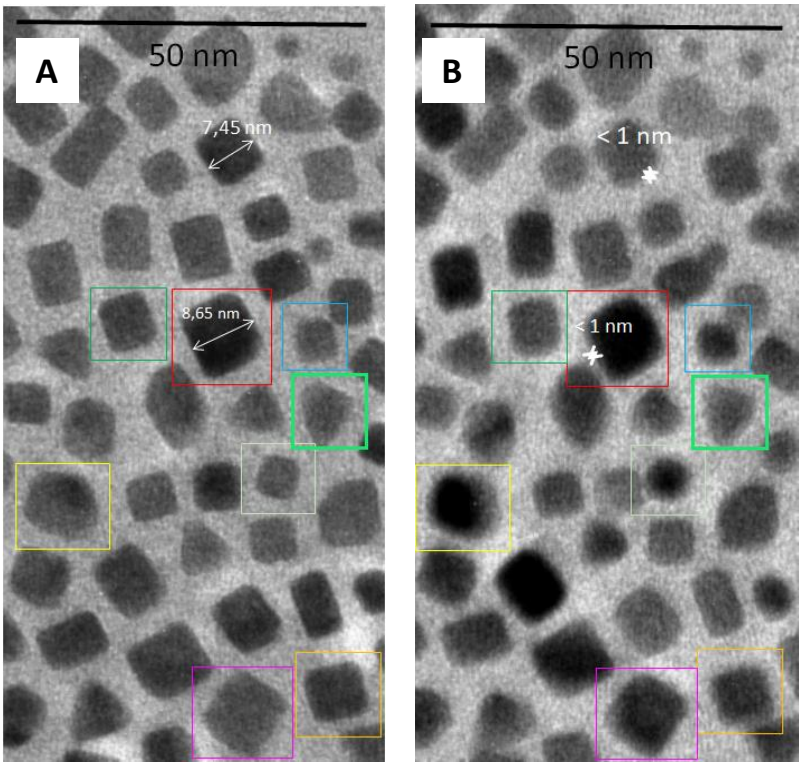

Figure V-3. PtZn NPs under vacuum at RT in the ECELL prior to (A) and under gas pressure of 4 mbar of CO + O_2 (1:4) (B)

During circulation of O_2 or CO and O_2 (1:4) mixture at 3 mbar at room temperature the NPs exhibited segregation and a ~1 nm thickness layer of ZnO was formed on the surface after 1 minute of the gases exposure (Fig. V-3). Had the exposure continued at the same pressure for 3 minutes, there would have been observed CO surface contamination (Fig. V-4).

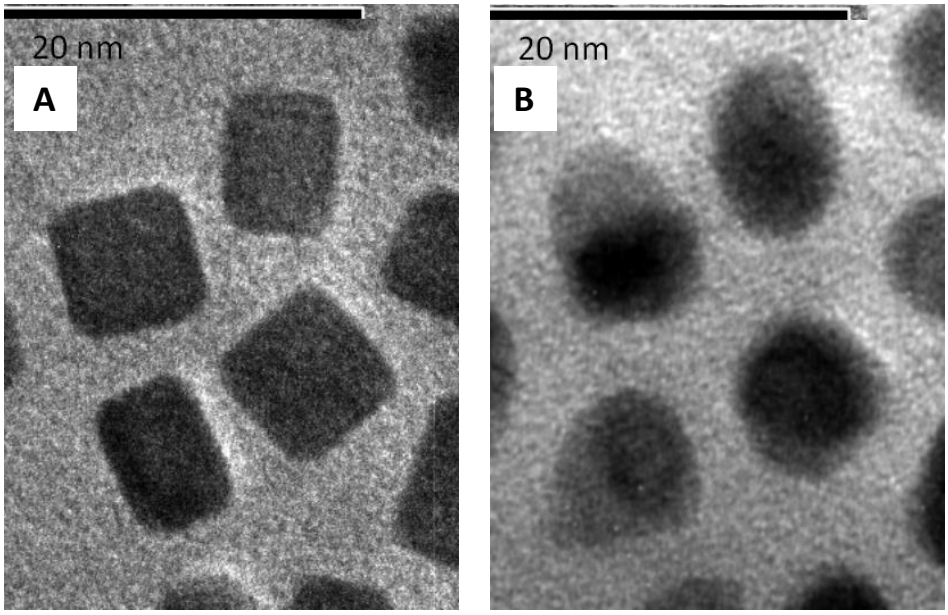

Figure V-4. PtZn NPs under vacuum in the ECELL prior to (A) and under gas pressure of 4 mbar of CO + O_2 (1:4) after a 3 min exposure (B)

If the gases contamination of Pt NPs is quite common resulting in rounding of their shape and making NPs observation extremely difficult[1,205], the metals segregation is a special feature of the PtZn bimetallic system resulting in a formation of a surface zinc oxide.

2. CO Oxidation on PtZn NCs: Post-Mortem Analysis by XPS

Despite the fact that the challenge posed by modern catalysis of CO oxidation is to reduce the reaction temperature as much as possible, efficient catalysts operating in high yields at room temperature do not exist yet. Therefore, the study of this prototypical reaction on PtZn NCs was very motivating because we thought we could have identified several surface species that play a key role in CO oxidation, and determined the correlative transformations of the NC surface, as we did in real-time NAP-XPS experiments for the ZnO/Pt(111) model system. These objectives could be not entirely fulfilled for two reasons. First the analyses are made post-mortem, and not in operando conditions as in NAP-XPS and mass-spectrometry experiments. Thus reaction products could not be detected. Second, as the interesting adsorbates CO, carboxyls, formates observed in the case of the ZnO/Pt(111) model system show up essentially in the C 1s spectrum., the large contribution of the carbons oleylamine tail overwhelms them, making their detection impossible. However, in the N 1s spectra we have obtained a clear evidence of the changes in adsorption mode of oleylamine upon CO adsorption, or H_2 elimination. This could only be interpreted in the context of Wand's model, and is a valuable contribution to a better understanding of the role of oleylamine as a ligand around metallic NCs.

2.1 The annealing condition: the temperature

The experimental conditions were essentially dictated by our previous CO oxidation experiment described in Chapter II. The ZnO/Pt(111) model system has taught us that very large CO oxidation rates are observed from 520 K. However, when the inverse catalyst sytsem is compared to pure Pt(111), no positive impact in the presence of ZnO on the reactivity can be measured. This is due to mass transport limitation as discussed before. Moreover the presence of formates (that are spectator species) suggests that the CO + OH associative reaction at the ZnO/Pt boundary is ineffective (no synergistic effect is expected). On the other hand, there is a clear enhancement of CO_2 production at low temperature (410 K) whith respect to the plain Pt(111) case.

Due to the aformentionned reasons, we have chosen a temperature of ~400 K to study changes in the chemistry of the PtZn NC. Under actual conditions of a catalytic reaction, it is often difficult to untangle the influence of specific factors (temperature, presence of the gas phase) on the catalysts used which renders the interpretation of the results complicated. In such cases, the general approach of splitting a complex problem into smaller ones helps to significantly simplify the task. Therefore, we have split the problem into two parts. First we have made a thermal annealing under UHV, and, second we have exposed the material to a 1 mbar CO +O_2 mixture (1:4), as in our NAP-XPS work. Both treatments were made in the preparation chamber. Then the samples were introduced into the XPS chamber operated under UHV. In the future, treatments above 520 K could be performed, to have a wider view of the processes. In particular the stability of the oleylamine ligand with an increasing annealing temperature should be studied in detail. We recall that the NC were prepared at 620 K in oleylamine. However the stability under UHV or gas mixture may be different.

2.2 Annealing at 400 K under UHV

Pure ZnO NCs. When heated to 400 K in UHV, the oxidized Zn NCs exhibit a major changes in the N 1s region when they are compared to as synthesized NCs (AS). In contrast, the other spectra (O 1s, C 1s not shown here) do not exhibit any remarkable change. In Fig. V-5 we

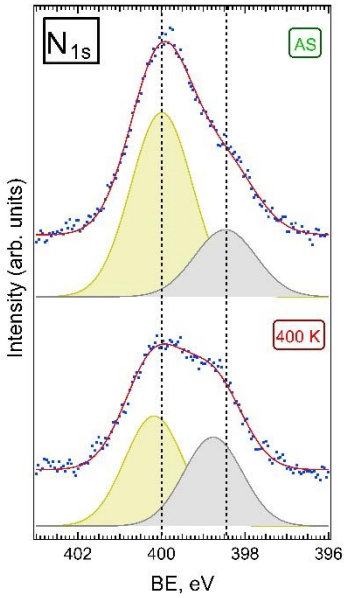

Figure V-5. The N1s spectra of ZnO NPs before and after heating to 400 K under UHV. Monochromatized Al K_α source. The overall resolution is 640 meV.

observe that the intensity of the component associated to unbound amines (400 eV) diminishes. Qualitatively, we also observe that overall N 1s intensity diminishes, via the change in the N 1s

to Zn $2p_{3/2}$ intensity ratio ($5.2x10^{-3}$ vs. $2.6x10^{-3}$). Our conclusion is that the interdigitated, unbound amine is evaporated in the vacuum.

Alloyed NCs. $Pt_{77}Zn_{23}$ NCs with a size of 3 nm possess both the largest specific surface area and the highest zinc content of the series. Changes in the Zn Auger and 2p spectra (Fig. V-6) suggest that the oxidized zinc tends to be reduced by the thermal treatment under vacuum.

The O 1s region helps to follow the fate of the hydroxyls, lattice O^{2-}, water, oxidized carbon species (Fig. V-7). By increasing the sample temperature to 400 K the ratio between hydroxyl groups (in brown) and lattice oxygen (in green) decreases. This means that we see a partial desorption of water and the decomposition of hydroxyls, followed by the formation of additional zinc oxide.

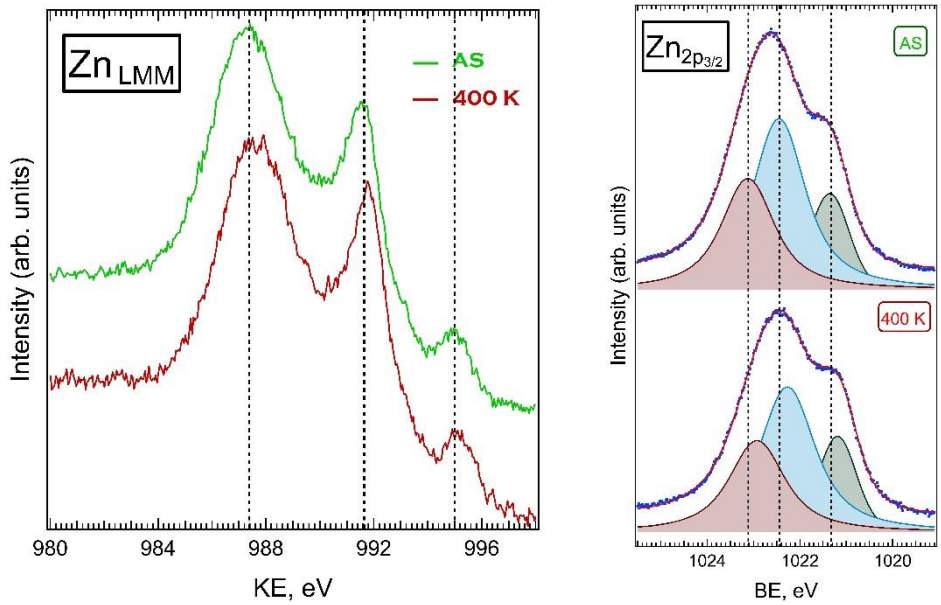

Figure V-6. $Pt_{77}Zn_{23}$ NCs Monochromatized Al K_α source. The overall resolution is 640 meV.

The most interesting information concerns changes in the bonding of the oleylamine ligand. They are contained in the N 1s spectra of Fig. V-7. When the NC is heated in vacuum, the component at 398.4-398.2 eV diminishes (the shoulder is clearly attenuated), while the 397.2 eV component increases. So far, all the interpretations proposed for the N 1s lead to the fact that oleylamine is bonded to platinum. Indeed, if the platinum surfaces of the NC is "dry", this modification of the N 1s spectrum suggests we are now witnessing the second stage of dehydrogenation, i.e. R-NH-Pt species transform into R-N<Pt_2 species. Now, if the NC surface is "wet", the platinum surface is covered with Pt-H species, and, in the framework of Wand's

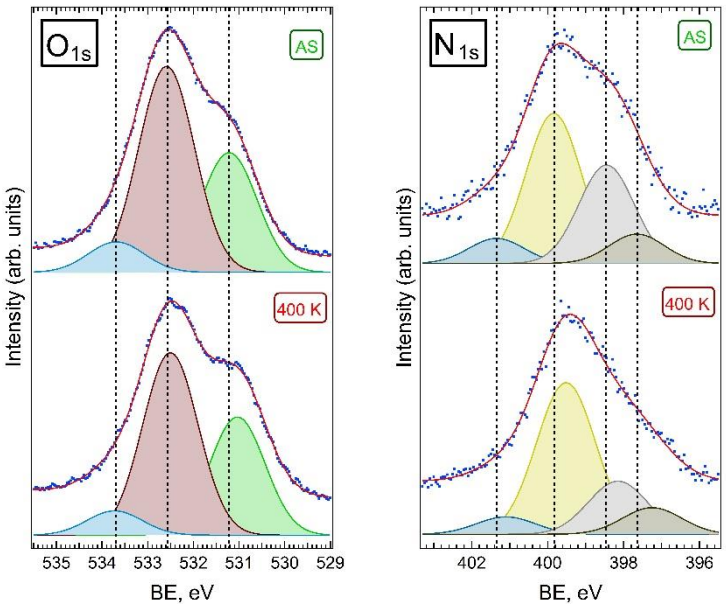

Figure V-7. $Pt_{77}Zn_{23}$ The O1s and N1s spectra of $Pt_{77}Zn_{23}$ NPs before (AS) and after (400K) heating treatment under UHV. Monochromatized Al K_α source. The overall resolution is 640 meV.

model, the 398.4 eV component corresponds the acceptor-donor amine configuration, see Fig. IV-4. Therefore a decrease of the acceptor-donor configuration and an increase of the purely donor geometry of Fig. IV-4 (positioned at 396.7 eV) is explainable if there is less Pt-H bonds (and thus less Pt-H…N hydrogen-bonds) on the surface when the sample is annealed at 400 K under UHV. In TPD experiments, H_2 is desorbed from the Pt(111) surface, at temperatures above 300 K.[206,190] Therefore a change in the H-bond configurations is also possible. The examination of N 1s spectral changes upon CO adsorption at 300 K will give a strong support to present assumptions.

3. PtZn NPs Exposed to the CO + O_2 Mixture

In this part we have exposed the NCs to the gas mixture CO:O_2 (1:4) under a total pressure of 1 mbar, that reproduces the in situ NAP-XPS experiments at SOLEIL on model surfaces and in situ HRTEM carried out in Marseille.

We start our discussion with the XPS core-levels of the "cuboid" $Pt_{86}Zn_{14}$ NCs, of average size 5 nm. The spectra are shown in Fig. V-8. Let us focus first our attention on the N 1s spectra that carry the most interesting information. After an exposure to the CO+O_2 mixture at room temperature, a clear change is seen in the N 1s. The shoulder at 398.3 eV is attenuated after exposure to the gas mixture at 300 K, similar to what is observed after a thermal annealing in

vacuum at 400 K. Energetic considerations from the literature are helpful to understand the observed phenomenon. CO will prefer platinum to ZnO. CO is weakly bound to ZnO surfaces, as the experimental adsorption energy ranges from 0.17 eV to 0.28 eV,[139] according to the surface termination. In contrast, the adsorption energy of CO on Pt(111) is much larger, ~1.3 eV,[207] and more than 1.45 eV on Pt(100).[208] *Therefore CO adsorption displaces the species found at a binding energy of 398.3 eV.* If we discard the byproduct hypothesis (the imine group in the ketenimine or diketenimine byproducts (see Scheme IV-2) is also at ~398.4 eV), and consider that the 398.3 eV component is related to non-dissociated oleylamine, it indicates *first* that oleylamine bonds to platinum. Second, it tells that this bonding is relatively weak.

With respect to this latter point let us consider again the "UHV platinum surface hypothesis" where the 398.4 eV line is attributed to a Pt-NH-R (one H abstracted) moiety. To remove this configuration, a H atom on the surface must recombine with the partially dissociated head. Taking again methylamine as good approximant of oleylamine, theoretical calculations show the activation barrier for this process is the sum the activation energy of the dissociation reaction $CH_3NH_2 \rightarrow CH_3NH + H$ (1.05 eV) and that of the reaction energy (0.95 eV). A 2.0 eV activation barrier results for the recombination reaction, which makes it unrealistic. The H atom could be dislodged by a CO atom adsorbing on the surface, which has been observed experimentally for the Pt(111) surface,[209] but we do not know how this will affect the potential landscape. Therefore, we do not see how CO could displace a Pt-NH-R entity at room temperature. If we still keep the hypothesis that adsorbed H atoms are displaced by CO atoms at room temperature,[209] the "H-covered platinum surface model" (Wand's model) seems more promising. With more Pt-H entities replaced by Pt-CO ones, we have less Pt-H…N acceptor bonds on the surface, and hence the intensity of the acceptor-donor configuration (398.4 eV) decreases. Note that the "ionic bonding mode" at 401.2 eV is not affected by CO adsorption, which would not be surprising as it does not involve H atoms. Finally, we note that increasing the temperature to 400 K in the presence of the $CO+O_2$ mixture accentuates the trends observed in the N 1s spectrum. This means that they are less adsorbed H on the platinum surfaces.

Finally, we turn our attention to the O 1s spectrum in Fig. V-8. We observe that the component at 531 eV increases after CO exposure. Let us first consider what the O 1s binding energies of CO adsorbed on the platinum surfaces are.

On clean Pt(111) two components appear at 530.9 eV (bridge site) and 532.5 eV (on-top site).[133] Naturally there are other faces than (111) that are exposed to CO, especially the (100) faces in

the cuboid $Pt_{86}Zn_{14}$ NCs. To our knowledge, there is no resolved O 1s spectrum of CO adsorbed on (100) (the work by Brodén et al. has not the sufficient resolution[210]). However, for CO on the unreconstructed (1×1) surface,[211] IRAS reveals that both on-top and bridge sites are occupied with bridge (on-top) sites being preferred over on-top (bridge) surface at 90 K (300 K). On-top CO has the same O 1s binding energies on (110) and (111). This also true for bridge CO.[208] If we extend this property to (100), we can expect that, independently from the crystallographic orientation on-top CO and bridge CO will show up at~532.6 eV and ~531 eV, respectively. Unfortunately, these components will coincide with the preexisting "brown" (hydroxyl) and "green" (ZnO lattice $^-$ ion) of the remaining oxidized zinc. However, the change in Fig.V-8 is sufficiently clear. Therefore, the increase of the 531 eV component intensity may be associated to the bonding of CO molecule on these platinum areas, in which case more "bridge" CO molecules are adsorbed than "on-top" ones.

With regard to ZnO, we see no effect in the Zn $2p_{3/2}$ spectrum due to the adsorption of CO at room temperature. The rise in temperature (in the presence of the gas mixture) leads to a slight reduction of the oxidized component which can be detected in the Zn $2p_{3/2}$ spectrum.

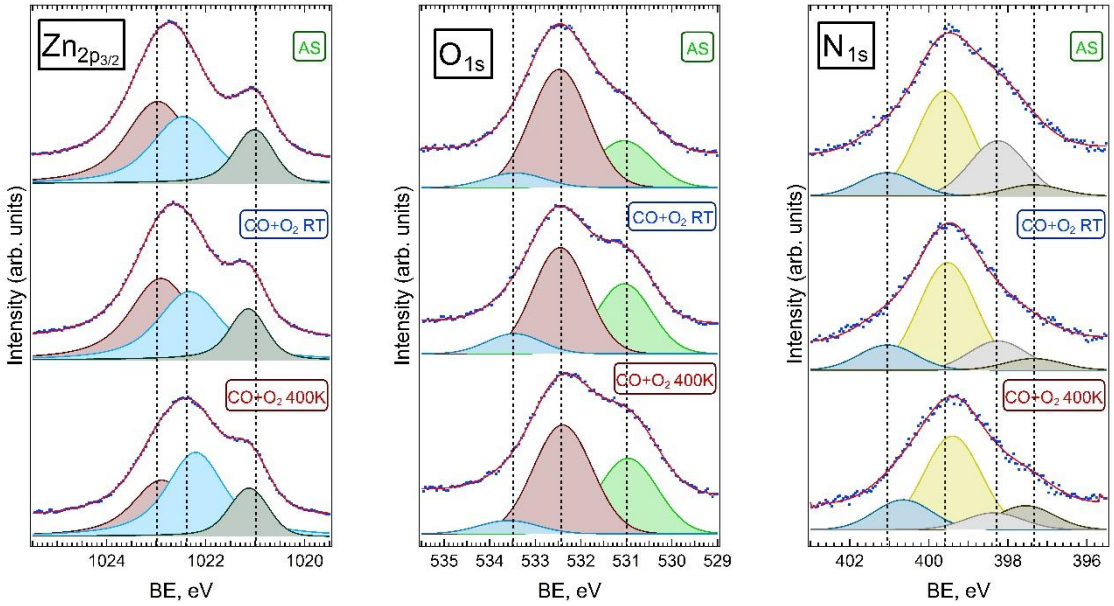

Figure V-8. XPS spectra of $Pt_{86}Zn_{14}$. Monochromatized Al K_α source. The overall resolution is 640 meV.

The Zn 2p, O 1s and N 1s spectra of samples having a smaller zinc content are shown in Fig. V-9 ($Pt_{89}Zn_{11}$) and V-10 ($Pt_{95}Zn_5$). The N 1s spectrum of the $Pt_{89}Zn_{11}$ NCs is particularly interesting because the free oleylamine component (R-NH_2 in yellow) is well reduced due to an efficient washing in ethanol. Therefore, the decrease of the component at 398.4 eV is

particularly spectacular after exposure to CO at 300 K. A subsequent heating at 400 K in the gas mixture enhances the phenomenon. Now the component at 397.6 eV predominates over the one at 398.4 eV. Similar trends are seen for the $Pt_{95}Zn_5$. The effects are less dramatic than for the $Pt_{89}Zn_{11}$ NC, simply because the free R-NH_2 oleylamine component is larger, due to a less efficient washing. Therefore, the lower zinc content NCs confirm the trends observed for the $Pt_{86}Zn_{14}$ NCs.

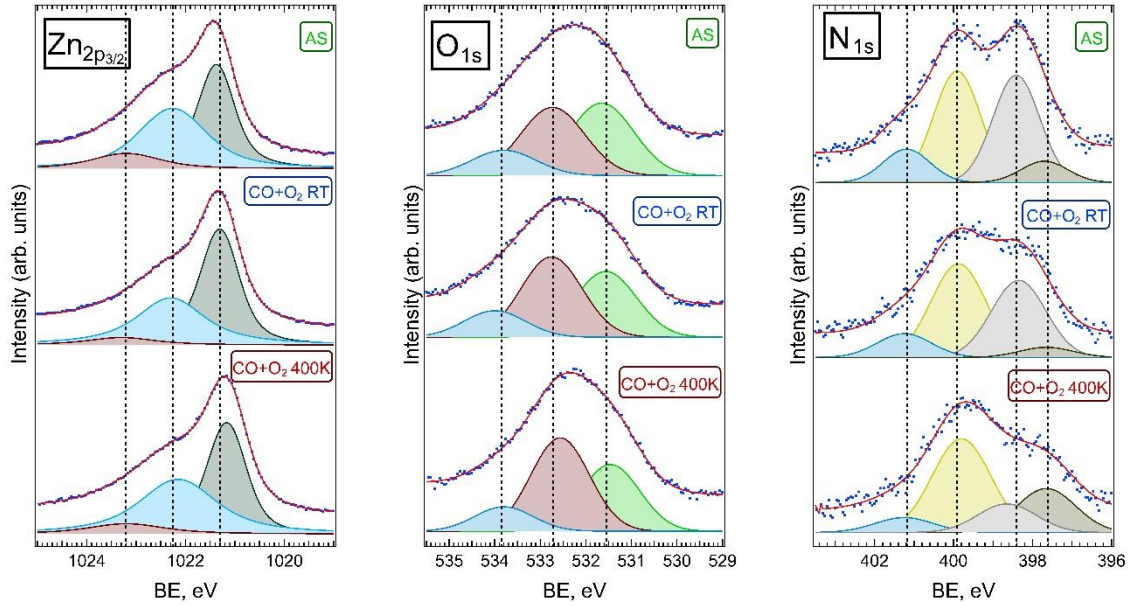

Figure V-9. XP spectra of $Pt_{89}Zn_{11}$. Monochromatized Al K_α source. The overall resolution is 640 meV.

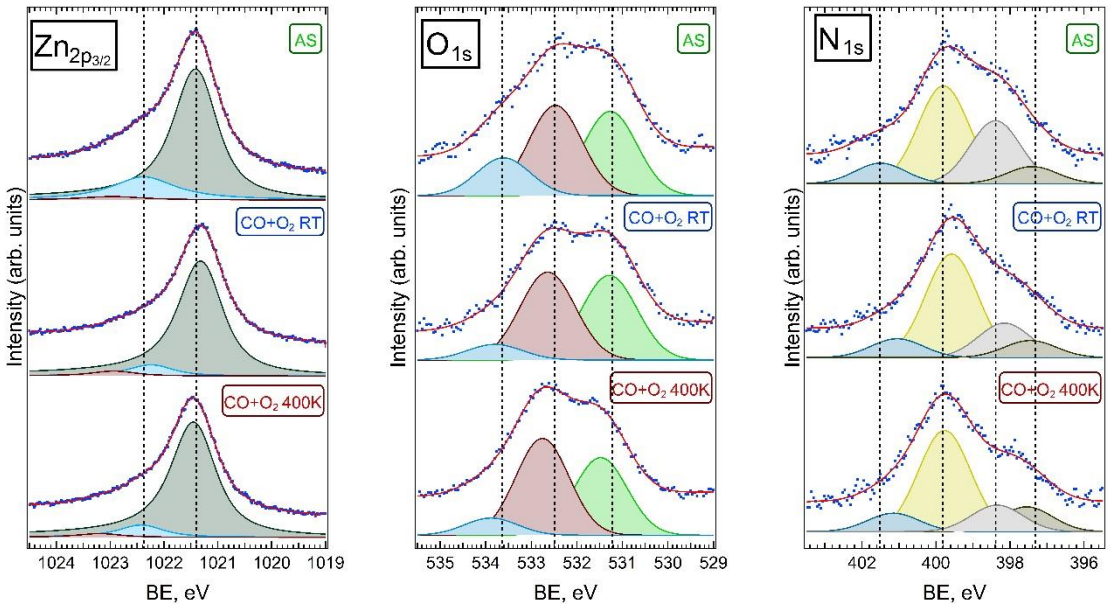

Figure V-10. XP spectra of $Pt_{95}Zn_5$. Monochromatized Al K_α source. The overall resolution is 640 meV.

Concerning the O 1s spectra of the "cubic", 9 nm NCs ($Pt_{95}Zn_5$) in Figure V-10 we observe that the components, brown (where on-top CO appears) and green (where bridge CO appears), increase after exposure to CO. Correlatively the light blue component (water on ZnO) is dwarfed.

For the sake of consistency with the O 1s spectrum of $Pt_{86}Zn_{14}$ (Fig. V-9), we must assume that CO occupies more bridge-sites than on-top ones on $Pt_{86}Zn_{14}$ ("cube-like" NCs of 5 nm diameter), while an equal number of on-top and bridge sites are populated for the bigger $Pt_{95}Zn_5$ NCs ("spherical" NCs of diameter 9 nm). In fact, while the (001) plane predominates in the former case, other planes (including (111)) are present in the latter. This may explain the observed differences.

In summary, our study of PtZn alloys exposed to CO plus O_2 at room temperature (and 400 K) has given a highly valuable insight on the bonding of oleylamine on the PtZn NC. It proves that oleylamine is bonded to the platinum (or Pt-rich) surfaces. As the distribution of the oleylamine adsorption modes changes upon CO adsorption, we favor at present, the explanatory framework proposed by Wand and colleagues,[177] that focuses on the role of Pt-H and the hydrogen bonds it can make with the amine head. Once the adsorbed H atom is displaced by CO adsorption, or leaves the surface by dimerization and desorption at 400 K, the acceptor-donor amine peak at

398.5 eV decreases. On the other hand the peak at 397.4 eV of the donor amine tends to increase. The fact that oleylamine leaves room to the CO reactant means that the surfactant is sufficiently labile to enable the adsorption of reactants on the surface. At the same time, it is sufficiently firmly anchored to protect the growth of the nanocrystals. That’s good news.

General Conclusions and Perspectives

The purpose of this thesis was to explore the surface chemistry of platinum-zinc bimetallic systems, and their catalytic activity in the oxidation reaction of CO. The research on this bimetallic system was carried out on two fronts: a surface science study of the model system, a discontinuous ZnO single layer epitaxied on Pt(111), using scanning tunneling microscopy and synchrotron radiation near ambien pressure x-ray photoemission, and a more "nanomaterial science" oriented study of the same bi-metallic system, using complex colloidal synthesis chemistry, transmission and scanning electron microscopy, and finally laboratory XPS.

First, a model surface consisting of a ZnO monolayer film supported on Pt(111) was fabricated under ultra-high vacuum conditions. Its surface chemistry was explored by STM and then by synchrotron radiation NAP-XPS under operando conditions. We were able to prove that this system was indeed a typical case of inverse catalysis. Synergetic effects due to the presence of both materials were well seen, but only at low temperatures (up to 410 K). Beyond that temperature, mass transport effects prevent the reactivity of the ZnO/Pt(111) and Pt(111) surfaces from being compared. We have shown that reaction intermediates must be formed in the border area between ZnO and platinum, when the ZnO film is discontinuous. We have highlighted the key role played by the hydroxyls present only ion the ZnO patches, which are due to the dissociation of H_2 or H_2O from the residual atmosphere on the platinum patches. In particular, we have detected by NAP-XPS the presence of a carboxyl species (due to the association of OH with CO), which precedes the desorption of CO_2. Above 410 K, a formate appears, and the latter species is likely a spectator in the CO oxidation process.

The transfer of the knowledge accumulated in the preceding surface science and model catalysts studies, to the more realistic case of nanocrystals of the PtZn alloy, while it helped identify some common phenomena, it also shows its limitations. In fact the NC coated with their oleylamine ligands have characteristics that UHV model surfaces do not possess, due to the NC fabrication process itself: we have found spectroscopic hints of the presence of water (possibly a byproduct of the reaction, arising from a condensation reaction between the ketone and the amine); in addition, a capping of the platinum surface by H atoms, is, at present, explanatory of many observed phenomena.

Finding the experimental conditions to produce bimetallic nano-alloys from two metal-$acac_2$ precursors was a daunting task, much more than that of physically depositing a thin film on a UHV monocrystal. Our efforts were rewarded as we were able to produce PtZn alloy NCs. This

one of the main points of the present study. The presence of $Pt(acac)_2$ prevents zinc (whose from being fully oxidized to ZnO, which is the case when $Zn(acac)_2$ alone is present in oleylamine. Monochromatized XPS shows that zinc makes an alloy with platinum, where it remains metallic, while another fraction is under the form of ZnO. It is not completely clear whether two reaction channels are in competion (PtZn alloying versus Zn oxidation by water), or Zn is oxidized afterwards, i.e. after exposure to air.

The alloyed NCs have been studied in detail by advanced methods of electron microscopy (including under operando conditions), diffraction and EDS. Unlike the case of the surface model where the STM images were particularly telling, we do not have at this stage of the study an exact model of the interface between the metal alloy and the zinc oxide that surrounds it. On the other hand, we know that the core of the NCs is occupied by the PtZn alloy, and that the outer planes are identical to those of pure platinum.

XPS allowed us to better understand how the oleylamine molecule binds to the NC. We have examined the question of the byproducts, which apart from water, could consist in ketenimine, diketenimine, and dialkylamine species. If we assume that oleylamine is the largely dominant species at the surface of the NCs (complementary experiments are needed), a reasonable, but tentative, interpretation of the N 1s spectra requires that water, hydroxide ions and H atoms are present on the platinum areas of the NCs. On the one hand, the oleylamine head would form (after protonation) an ionic bond with a HO^-. On the other hand, its non-protonated form ($R-NH_2$) would make a single donor hydrogen bond with platinum or double H-bonds, one donor with Pt and one acceptor with Pt-H. This original model had been previously proposed by Wand and collaborators. By exposing the NCs to CO at ambient temperature we have got indirect evidence of the adsorption of this probe molecule from a change in the N 1s spectrum. This can be rationally explained by considering that CO removes adsorbed hydrogen, and decreases the ability of the amine to create double H-bonds. Similar observations could be made after annealing in vacuum, due to the loss of H from the metallic surfaces.

We believe that combined microscopy and photoemission studies, together with controlled particle growths, are of great interest. The chemistry of bimetallics is particularly puzzling, especially when the two components have so different chemical properties, like Zn end Pt. Moreover, the suspicion that water or hydrogen atoms play a role in the growth reaction and in ligand attachment should be examined both from the point of view of organometallic chemistry (one Pt atom), and from that of surface chemistry. We can notice that those two “worlds” are not yet“bridged”. It is certainly desirable to extend the type of study we started in this thesis by

performing XPS analyses of the growing NC, under real conditions, in the presence of the solvent oleylamine, using graphene encapsulation for instance. The same applies to reactivity. It would be also highly desirable to study the oxidation reaction of CO under NAP conditions, and explore in detail the role of water or of H_2 partial pressures. Then to get fundamental insights, it may be necessary to focus on a simpler system such as pure platinum NCs.

References

1. Cabié, M. *et al.* Direct Observation of the Reversible Changes of the Morphology of Pt Nanoparticles under Gas Environment. *J. Phys. Chem. C* **114**, 2160–2163 (2010).

2. Dessal, C. *et al.* Dynamics of Single Pt Atoms on Alumina during CO Oxidation Monitored by Operando X-ray and Infrared Spectroscopies. *ACS Catal.* **9**, 5752–5759 (2019).

3. Naitabdi, A. *et al.* CO oxidation activity of Pt, Zn and ZnPt nanocatalysts: A comparative study by: In situ near-ambient pressure X-ray photoelectron spectroscopy. *Nanoscale* **10**, 6566–6580 (2018).

4. Roldan Cuenya, B. Metal Nanoparticle Catalysts Beginning to Shape-up. *Acc. Chem. Res.* **46**, 1682–1691 (2013).

5. Gänzler, A. M. *et al.* Tuning the Structure of Platinum Particles on Ceria In Situ for Enhancing the Catalytic Performance of Exhaust Gas Catalysts. *Angew. Chemie Int. Ed.* **56**, 13078–13082 (2017).

6. Bowker, M. Automotive catalysis studied by surface science. *Chem. Soc. Rev.* **37**, 2204 (2008).

7. Carrette, L., Friedrich, K. A. & Stimming, U. Fuel Cells - Fundamentals and Applications. *Fuel Cells* **1**, 5–39 (2001).

8. Jung, N., Chung, D. Y., Ryu, J., Yoo, S. J. & Sung, Y.-E. Pt-based nanoarchitecture and catalyst design for fuel cell applications. *Nano Today* **9**, 433–456 (2014).

9. Tao, F. *et al.* Reaction-Driven Restructuring of Rh-Pd and Pt-Pd Core-Shell Nanoparticles. *Science (80-.).* **322**, 932–934 (2008).

10. Wu, C. H., Eren, B. & Salmeron, M. B. Structure and Dynamics of Reactant Coadsorption on Single Crystal Model Catalysts by HP-STM and AP-XPS: A Mini Review. *Top. Catal.* **59**, 405–419 (2016).

11. Freund, H.-J. Model Studies in Heterogeneous Catalysis. *Chem. - A Eur. J.* **16**, 9384–9397 (2010).

12. Salmeron, M. & Schlogl, R. Ambient pressure photoelectron spectroscopy: A new tool for surface science and nanotechnology. *Surf. Sci. Rep.* **63**, 169–199 (2008).

13. Bluhm, H. *et al.* Methanol oxidation on a copper catalyst investigated using in situ X-ray photoelectron spectroscopy. *J. Phys. Chem. B* **108**, 14340–14347 (2004).

14. Freund, H.-J., Meijer, G., Scheffler, M., Schlögl, R. & Wolf, M. CO Oxidation as a Prototypical

Reaction for Heterogeneous Processes. *Angew. Chemie Int. Ed.* **50**, 10064–10094 (2011).

15. Etman, H. A., Zheleva, Z. V., Held, G. & Bennett, R. A. Epitaxial Growth of Ultrathin Palladium Films on Re{0001}. *J. Phys. Chem. C* **115**, 4191–4199 (2011).

16. Rodriguez, J. A. *et al.* Inverse Oxide/Metal Catalysts in Fundamental Studies and Practical Applications: A Perspective of Recent Developments. *J. Phys. Chem. Lett.* **7**, 2627–2639 (2016).

17. Chen, H. *et al.* CO and H 2 Activation over g-ZnO Layers and w-ZnO(0001). *ACS Catal.* **9**, 1373–1382 (2019).

18. Kattel, S., Chen, J. G. & Liu, P. Active sites for CO 2 hydrogenation to methanol on Cu/ZnO catalysts. **1299**, 1296–1299 (2017).

19. Kim, Y., Trung, T. S. B., Yang, S., Kim, S. & Lee, H. Mechanism of the Surface Hydrogen Induced Conversion of CO 2 to Methanol at Cu(111) Step Sites. *ACS Catal.* **6**, 1037–1044 (2016).

20. Faraday M. Experimental relations of gold and other metals to light. *Philos. Trans. R. Soc. London* **147**, 145–181 (1847).

21. Turkevich, J., Stevenson, P. C. & Hillier, J. A study of the nucleation and growth processes in the synthesis of colloidal gold. *Discuss. Faraday Soc.* **11**, 55 (1951).

22. Pileni, M. P. Reverse micelles as microreactors. *J. Phys. Chem.* **97**, 6961–6973 (1993).

23. Brust, M., Walker, M., Bethell, D., Schiffrin, D. J. & Whyman, R. Synthesis of Thiol-derivatised Gold Nanoparticles in. 801–802 (2000).

24. Demortière, A. & Petit, C. First synthesis by liquid-liquid phase transfer of magnetic Co xPt100-x nanoalloys. *Langmuir* **23**, 8575–8584 (2007).

25. Kameche, F. *et al.* Role of the nanocrystallinity on the chemical ordering of CoxPt100-x nanocrystals synthesized by wet chemistry. *Phys. Chem. Chem. Phys.* **17**, 28162–28170 (2015).

26. Philippot, K. & Chaudret, B. Organometallic approach to the synthesis and surface reactivity of noble metal nanoparticles. *Comptes Rendus Chim.* **6**, 1019–1034 (2003).

27. Zhang, Q., Xie, J., Yu, Y. & Lee, J. Y. Monodispersity control in the synthesis of monometallic and bimetallic quasi-spherical gold and silver nanoparticles. *Nanoscale* **2**, 1962–1975 (2010).

28. Park, J., Joo, J., Soon, G. K., Jang, Y. & Hyeon, T. Synthesis of monodisperse spherical nanocrystals. *Angewandte Chemie - International Edition* **46**, 4630–4660 (2007).

29. Gilroy, K. D., Ruditskiy, A., Peng, H. C., Qin, D. & Xia, Y. Bimetallic nanocrystals: Syntheses,

properties, and applications. *Chem. Rev.* **116**, 10414–10472 (2016).

30. LaMer, V. K. & Barnes, M. D. Monodispersed hydrophobic colloidal dispersions and light scattering properties. I. Preparation and light scattering properties of monodispersed colloidal sulfur. *J. Colloid Sci.* **1**, 71–77 (1946).

31. Beattie, J. K. Monodisperse colloids of transition metal and lanthanide compounds. *Pure Appl. Chem.* **61**, 937–941 (1989).

32. Wu, L., Mendoza-Garcia, A., Li, Q. & Sun, S. Organic Phase Syntheses of Magnetic Nanoparticles and Their Applications. *Chemical Reviews* **116**, 10473–10512 (2016).

33. Petit, C. & Pileni, M. P. Synthesis of cadmium sulfide in situ in reverse micelles and in hydrocarbon gels. *J. Phys. Chem.* **92**, 2282–2286 (1988).

34. Liu, K. & Park, S. J. Preparation of highly luminescent CdSe quantum dots by reverse micelles. *Jpn. J. Appl. Phys.* **53**, 08ME03 (2014).

35. Hanna, H., Bagwe, R., Palmqvist, A., Skoglundh, M. & Svanberg, C. Kinetics of the Formation of Nano-Sized Platinum Particles in Water-in-Oil Microemulsions. **111**, 104–111 (2001).

36. Lisiecki, I. Size, Shape, and Structural Control of Metallic Nanocrystals. *J. Phys. Chem. B* **109**, 12231–12244 (2005).

37. Petit, C., Taleb, A. & Pileni, M.-P. Self-Organization of Magnetic Nanosized Cobalt Particles. *ChemInform* **29**, no-no (2010).

38. Petit, C., Lixon, P. & Pileni, M. P. In situ synthesis of silver nanocluster in AOT reverse micelles. *J. Phys. Chem.* **97**, 12974–12983 (1993).

39. Salzemann, C., Zhai, W., Goubet, N. & Pileni, M. How to Tune the Au Internanocrystal Distance in Two-Dimensional Self-Ordered Superlattices. *J. Phys. Chem. Lett.* **1**, 149–154 (2010).

40. Petit, C., Rusponi, S. & Brune, H. Magnetic properties of cobalt and cobalt–platinum nanocrystals investigated by magneto-optical Kerr effect. *J. Appl. Phys.* **95**, 4251–4260 (2004).

41. Xiong, L. & Manthiram, A. Nanostructured Pt – M / C (M = Fe and Co) catalysts prepared by a microemulsion method for oxygen reduction in proton exchange membrane fuel cells. **50**, 2323–2329 (2005).

42. Shevchenko, E. V *et al.* Colloidal Synthesis and Self-Assembly of CoPt 3 Nanocrystals. *J. Am. Chem. Soc.* **124**, 11480–11485 (2002).

43. Yashima, M., Falk, L. K. L., Palmqvist, A. E. C. & Holmberg, K. Structure and catalytic properties of nanosized alumina supported platinum and palladium particles synthesized by

reaction in microemulsion. **268**, 348–356 (2003).

44. Chen, D.-H. & Chen, C. Formation and characterization of Au–Ag bimetallic nanoparticles in water-in-oil microemulsions. *J. Mater. Chem.* **12**, 1557–1562 (2002).

45. Naitabdi, A. & Roldan Cuenya, B. Formation, thermal stability, and surface composition of size-selected AuFe nanoparticles. *Appl. Phys. Lett.* **91**, 113110 (2007).

46. Brust, B. M., Bethell, D., Schffrin, D. J. & Kiely, C. J. Novel Gold-Dithiol Nano-Networks with Non-Metallic Electronic Properties. 795–797 (1995).

47. Brust, M., Bethell, D., Kiely, C. J. & Schiffrin, D. J. Self-Assembled Gold Nanoparticle Thin Films with Nonmetallic Optical and Electronic Properties. **7463**, 5425–5429 (1998).

48. Wilson, O. M., Scott, R. W. J., Garcia-Martinez, J. C. & Crooks, R. M. Synthesis, Characterization, and Structure-Selective Extraction of 1−3-nm Diameter AuAg Dendrimer-Encapsulated Bimetallic Nanoparticles. *J. Am. Chem. Soc.* **127**, 1015–1024 (2005).

49. Salzemann, C. *et al.* Platinum and platinum based nanoalloys synthesized by wet chemistry. *Faraday Discuss.* **181**, 19–36 (2015).

50. Cheng, Y. & Schiffrin, D. J. Electrodeposition of metallic gold clusters at the water/1,2-dichloroethane interface. *J. Chem. Soc. Faraday Trans.* **92**, 3865 (1996).

51. Varanda, L. C. & Jafelicci, M. Self-Assembled FePt Nanocrystals with Large Coercivity: Reduction of the fcc-to-L1 0 Ordering Temperature. *J. Am. Chem. Soc.* **128**, 11062–11066 (2006).

52. Ai, F., Yao, A., Huang, W., Wang, D. & Zhang, X. Synthesis of PVP-protected NiPd nanoalloys by modified polyol process and their magnetic properties. *Phys. E Low-dimensional Syst. Nanostructures* **42**, 1281–1286 (2010).

53. Bouar, Y. Le, Oikawa, T., Langlois, C., Loiseau, A. & Ricolleau, C. Ostwald Ripening in Nanoalloys : When Thermodynamics Drives a Size-Dependent Particle Composition. **255901**, 1–4 (2010).

54. Sun, S. Recent Advances in Chemical Synthesis, Self-Assembly, and Applications of FePt Nanoparticles. *Adv. Mater.* **18**, 393–403 (2006).

55. Kwon, S. G. & Hyeon, T. Colloidal Chemical Synthesis and Formation Kinetics of Uniformly Sized Nanocrystals of Metals, Oxides, and Chalcogenides. *Acc. Chem. Res.* **41**, 1696–1709 (2008).

56. Pan, C. *et al.* A New Synthetic Method toward Bimetallic Ruthenium Platinum Nanoparticles;

Composition Induced Structural Changes. *J. Phys. Chem. B* **103**, 10098–10101 (1999).

57. Meziane, L. *et al.* Hcp cobalt nanocrystals with high magnetic anisotropy prepared by easy one-pot synthesis. *Nanoscale* **8**, 18640–18645 (2016).

58. Vivien, A. *et al.* Role of Oleylamine Revisited: An Original Disproportionation Route to Monodispersed Cobalt and Nickel Nanocrystals. *Chem. Mater.* **31**, 960–968 (2019).

59. Naitabdi, A. Chemical Functionalization and Surface Nanopatterning. in *Encyclopedia of Interfacial Chemistry* 582–591 (Elsevier, 2018). doi:10.1016/B978-0-12-409547-2.13892-2

60. Pierucci, D. *et al.* Benzaldehyde on Water-Saturated Si(001): Reaction with Isolated Silicon Dangling Bonds versus Concerted Hydrosilylation. *J. Phys. Chem. C* **118**, 10005–10016 (2014).

61. Wang, Z. L. Transmission Electron Microscopy of Shape-Controlled Nanocrystals and Their Assemblies. *J. Phys. Chem. B* **104**, 1153–1175 (2002).

62. De Clercq, A. *et al.* Growth of Pt–Pd Nanoparticles Studied In Situ by HRTEM in a Liquid Cell. *J. Phys. Chem. Lett.* **5**, 2126–2130 (2014).

63. Alloyeau, D. *et al.* Unravelling Kinetic and Thermodynamic Effects on the Growth of Gold Nanoplates by Liquid Transmission Electron Microscopy. *Nano Lett.* **15**, 2574–2581 (2015).

64. Siegbahn, K. Electron spectroscopy for atoms, molecules and condensed matter - an overview. *J. Electron Spectros. Relat. Phenomena* **36**, 113–129 (1985).

65. Shavorskiy, A., Karslioglu, O., Zegkinoglou, I. & Bluhm, H. Synchrotron-based Ambient Pressure X-ray Photoelectron Spectroscopy. *Synchrotron Radiat. News* **27**, 14–23 (2014).

66. Naitabdi, A. *et al.* CO oxidation activity of Pt, Zn and ZnPt nanocatalysts: A comparative study by: In situ near-ambient pressure X-ray photoelectron spectroscopy. *Nanoscale* **10**, 6566–6580 (2018).

67. Tissot, H. *et al.* The Electronic Structure of Saturated NaCl and NaI Solutions in Contact with a Gold Substrate. *Top. Catal.* **59**, 605–620 (2016).

68. Chen, J. G., Menning, C. A. & Zellner, M. B. Monolayer bimetallic surfaces: Experimental and theoretical studies of trends in electronic and chemical properties. *Surf. Sci. Rep.* **63**, 201–254 (2008).

69. Yan, N., Xiao, C. & Kou, Y. Transition metal nanoparticle catalysis in green solvents. *Coord. Chem. Rev.* **254**, 1179–1218 (2010).

70. Yoo, J. S., Abild-Pedersen, F., Nørskov, J. K. & Studt, F. Theoretical Analysis of Transition-Metal Catalysts for Formic Acid Decomposition. *ACS Catal.* **4**, 1226–1233 (2014).

71. Zhang, Q., Uchaker, E., Candelaria, S. L. & Cao, G. Nanomaterials for energy conversion and storage. *Chem. Soc. Rev.* **42**, 3127–3171 (2013).

72. Zanella, R. & Louis, C. Influence of the conditions of thermal treatments and of storage on the size of the gold particles in Au / TiO 2 samples. **108**, 768–777 (2005).

73. Saavedra, J., Powell, C., Panthi, B., Pursell, C. J. & Chandler, B. D. CO oxidation over Au / TiO 2 catalyst : Pretreatment effects , catalyst deactivation , and carbonates production. *J. Catal.* **307**, 37–47 (2013).

74. Carrette, L., Friedrich, K. A. & Stimming, U. Fuel Cells: Principles, Types, Fuels, and Applications. *ChemPhysChem* **1**, 162–193 (2000).

75. Beatriz Roldan Cuenya, Ahmed R. Naitabdi, F. B. Thermally stable nanoparticles on supports. *United States Pat.* **1**, (2002).

76. Qiao, B. *et al.* Single-atom catalysis of CO oxidation using Pt1/FeOx. *Nat. Chem.* **3**, 634–641 (2011).

77. Kang, Y. *et al.* Engineering Catalytic Contacts and Thermal Stability: Gold/Iron Oxide Binary Nanocrystal Superlattices for CO Oxidation. *J. Am. Chem. Soc.* **135**, 1499–1505 (2013).

78. Guo, X. *et al.* Ferrous Centers Confined on Core–Shell Nanostructures for Low-Temperature CO Oxidation. *J. Am. Chem. Soc.* **134**, 12350–12353 (2012).

79. Dacquin, J. P. *et al.* Structural changes of nano-Pt particles during thermal ageing : Support-induced effect and related impact on the catalytic performances. *J. Catal.* **270**, 299–309 (2010).

80. Takei, T. *et al.* Heterogeneous Catalysis by Gold. in 1–126 (2012). doi:10.1016/B978-0-12-385516-9.00001-6

81. Bond, G. C., Louis, C. & Thompson, D. T. *Catalysis by Gold*. **6**, (2006).

82. Louis, C. Gold Nanoparticles: Recent Advances in CO Oxidation. in *Nanoparticles and Catalysis* 475–503 (Wiley-VCH Verlag GmbH & Co. KGaA). doi:10.1002/9783527621323.ch15

83. Qi, C., Zhu, S., Su, H., Lin, H. & Guan, R. Stability improvement of Au/Fe-La-Al2O3 catalyst via incorporating with a FexOy layer in CO oxidation process. *Appl. Catal. B Environ.* **138**–**139**, 104–112 (2013).

84. Li, L. *et al.* Origin of the high activity of Au / FeO x for low-temperature CO oxidation : Direct evidence for a redox mechanism. *J. Catal.* **299**, 90–100 (2013).

85. Freund, H.-J., Nilius, N., Risse, T. & Schauermann, S. A fresh look at an old nano-technology:

catalysis. *Phys. Chem. Chem. Phys.* **16**, 8148 (2014).

86. Liu, Z., Ma, L., Zhang, J., Hongsirikarn, K. & Goodwin, J. G. Pt Alloy Electrocatalysts for Proton Exchange Membrane Fuel Cells: A Review. *Catal. Rev.* **55**, 255–288 (2013).

87. Holton, O. T. & Stevenson, J. W. The Role of Platinum in Proton Exchange Membrane Fuel Cells. *Platin. Met. Rev.* **57**, 259–271 (2013).

88. Behrens, M. *et al.* The Active Site of Methanol Synthesis over Cu/ZnO/Al2O3 Industrial Catalysts. *Science (80-.).* **336**, 893–897 (2012).

89. Schumann, J. *et al.* Promoting Strong Metal Support Interaction: Doping ZnO for Enhanced Activity of Cu/ZnO:M (M = Al, Ga, Mg) Catalysts. *ACS Catal.* **5**, 3260–3270 (2015).

90. Yi, L. *et al.* Electrochemical oxidation of sodium borohydride on carbon supported Pt-Zn nanoparticle bimetallic catalyst and its implications to direct borohydride-hydrogen peroxide fuel cell. *Electrochim. Acta* **158**, 209–218 (2015).

91. Janotti, A. & Van de Walle, C. G. Fundamentals of zinc oxide as a semiconductor. *Reports Prog. Phys.* **72**, 126501 (2009).

92. Martynova, Y. *et al.* CO oxidation over ZnO films on Pt(1 1 1) at near-atmospheric pressures. *J. Catal.* **301**, 227–232 (2013).

93. Kang, Y., Pyo, J. B., Ye, X., Gordon, T. R. & Murray, C. B. Synthesis, shape control, and methanol electro-oxidation properties of Pt-Zn alloy and Pt 3Zn intermetallic nanocrystals. *ACS Nano* **6**, 5642–5647 (2012).

94. Eren, B., Heine, C., Bluhm, H., Somorjai, G. A. & Salmeron, M. Catalyst Chemical State during CO Oxidation Reaction on Cu(111) Studied with Ambient-Pressure X-ray Photoelectron Spectroscopy and Near Edge X-ray Adsorption Fine Structure Spectroscopy. *J. Am. Chem. Soc.* **137**, 11186–11190 (2015).

95. Wang, W.-W. *et al.* Highly Dispersed Copper Oxide Clusters as Active Species in Copper-Ceria Catalyst for Preferential Oxidation of Carbon Monoxide. *ACS Catal.* **5**, 2088–2099 (2015).

96. Stacchiola, D. J. Tuning the Properties of Copper-Based Catalysts Based on Molecular in Situ Studies of Model Systems. *Acc. Chem. Res.* **48**, 2151–2158 (2015).

97. González Carrazán, S. R., Wojcieszak, R., Blanco, R. M., Mateos-Pedrero, C. & Ruiz, P. Modulation of the selectivity in partial oxidation of methanol over CuZnAl catalysts by adding CO 2 and/or H 2 into the reaction feed. *Appl. Catal. B Environ.* **168**–**169**, 14–24 (2015).

98. Clercq, A. De, Margeat, O., Sitja, G., Henry, C. R. & Giorgio, S. Core – shell Pd – Pt nanocubes

for the CO oxidation. **336**, 33–40 (2016).

99. Matera, S., Maestri, M., Cuoci, A. & Reuter, K. Predictive-Quality Surface Reaction Chemistry in Real Reactor Models: Integrating First-Principles Kinetic Monte Carlo Simulations into Computational Fluid Dynamics. *ACS Catal.* **4**, 4081–4092 (2014).

100. Matera, S. *et al.* Evidence for the Active Phase of Heterogeneous Catalysts through In Situ Reaction Product Imaging and Multiscale Modeling. *ACS Catal.* **5**, 4514–4518 (2015).

101. van Spronsen, M. A., Frenken, J. W. M. & Groot, I. M. N. Surface science under reaction conditions: CO oxidation on Pt and Pd model catalysts. *Chem. Soc. Rev.* **46**, 4347–4374 (2017).

102. Campbell, C. T., Ertl, G., Kuipers, H. & Segner, J. A molecular beam study of the catalytic oxidation of CO on a Pt(111) surface. *J. Chem. Phys.* **73**, 5862–5873 (1980).

103. Burnett, D. J. *et al.* In-situ soft X-ray studies of CO oxidation on the Pt(111) surface. *Surf. Sci.* **564**, 29–37 (2004).

104. Libuda, J. *et al.* The CO oxidation kinetics on supported Pd model catalysts: A molecular beam/in situ time-resolved infrared reflection absorption spectroscopy study. *J. Chem. Phys.* **114**, 4669 (2001).

105. Gao, F., Wang, Y., Cai, Y. & Goodman, D. W. CO Oxidation on Pt-Group Metals from Ultrahigh Vacuum to Near Atmospheric Pressures. 2. Palladium and Platinum. *J. Phys. Chem. C* **113**, 174–181 (2009).

106. Blomberg, S. *et al.* In Situ X-Ray Photoelectron Spectroscopy of Model Catalysts: At the Edge of the Gap. *Phys. Rev. Lett.* **110**, 117601 (2013).

107. Gao, F., Wang, Y. & Goodman, D. W. Reply to "Comment on 'CO Oxidation on Pt-Group Metals from Ultrahigh Vacuum to Near Atmospheric Pressures. 2. Palladium and Platinum'". *J. Phys. Chem. C* **114**, 6874 (2010).

108. van Rijn, R. *et al.* Comment on "CO Oxidation on Pt-Group Metals from Ultrahigh Vacuum to Near Atmospheric Pressures. 2. Palladium and Platinum". *J. Phys. Chem. C* **114**, 6875–6876 (2010).

109. Fu, Q. *et al.* Interface-Confined Ferrous Centers for Catalytic Oxidation. *Science (80-.).* **328**, 1141–1144 (2010).

110. Mu, R. *et al.* Synergetic Effect of Surface and Subsurface Ni Species at Pt−Ni Bimetallic Catalysts for CO Oxidation. *J. Am. Chem. Soc.* **133**, 1978–1986 (2011).

111. Sun, D. *et al.* Theoretical Study of the Role of a Metal–Cation Ensemble at the Oxide–Metal

Boundary on CO Oxidation. *J. Phys. Chem. C* **116**, 7491–7498 (2012).

112. Martynova, Y. *et al.* CO oxidation over ZnO films on Pt(111) at near-atmospheric pressures. *J. Catal.* **301**, 227–232 (2013).

113. Knudsen, J., Andersen, J. N. & Schnadt, J. A versatile instrument for ambient pressure x-ray photoelectron spectroscopy: The Lund cell approach. *Surf. Sci.* **646**, 160–169 (2016).

114. Yu, Y. *et al.* Chemical states of surface oxygen during CO oxidation on Pt(1 1 0) surface revealed by ambient pressure XPS. *J. Phys. Condens. Matter* **29**, 464001 (2017).

115. Kondoh, H. *et al.* In situ analysis of catalytically active Pd surfaces for CO oxidation with near ambient pressure XPS. *Catal. Today* **260**, 14–20 (2016).

116. Liu, B. H., McBriarty, M. E., Bedzyk, M. J., Shaikhutdinov, S. & Freund, H. J. Structural transformations of zinc oxide layers on Pt(111). *J. Phys. Chem. C* **118**, 28725–28729 (2014).

117. Liu, B., Boscoboinik, J. A., Cui, Y., Shaikhutdinov, S. & Freund, H. Stabilization of Ultrathin Zinc Oxide Films on Metals: Reconstruction versus Hydroxylation. *J. Phys. Chem. C* **119**, 7842–7847 (2015).

118. Weirum, G. *et al.* Growth and surface structure of zinc oxide layers on a Pd(111) surface. *J. Phys. Chem. C* **114**, 15432–15439 (2010).

119. Schott, V. *et al.* Chemical Activity of Thin Oxide Layers: Strong Interactions with the Support Yield a New Thin-Film Phase of ZnO. *Angew. Chemie Int. Ed.* **52**, 11925–11929 (2013).

120. Deng, X. *et al.* Growth of Single- and Bilayer ZnO on Au(111) and Interaction with Copper. *J. Phys. Chem. C* **117**, 11211–11218 (2013).

121. Deng, X., Sorescu, D. C. & Lee, J. Enhanced adsorption of CO2 at steps of ultrathin ZnO: the importance of Zn-O geometry and coordination. *Phys. Chem. Chem. Phys.* **19**, 5296–5303 (2017).

122. Pan, Q. *et al.* Reactivity of Ultra-Thin ZnO Films Supported by Ag(111) and Cu(111): A Comparison to ZnO/Pt(111). *Catal. Letters* **144**, 648–655 (2014).

123. Duke, A. S., Galhenage, R. P., Tenney, S. A., Sutter, P. & Chen, D. A. In Situ Studies of Carbon Monoxide Oxidation on Platinum and Platinum–Rhenium Alloy Surfaces. *J. Phys. Chem. C* **119**, 381–391 (2015).

124. Kondakov, D. Y. & Young, R. H. Variable sensitivity of organic light-emitting diodes to operation-induced chemical degradation: Nature of the antagonistic relationship between lifetime and efficiency. *J. Appl. Phys.* **108**, 074513 (2010).

125. Blomberg, S. *et al.* Comparison of AP-XPS and PLIF Measurements During CO Oxidation Over Pd Single Crystals. *Top. Catal.* **59**, 478–486 (2016).

126. Zhou, J., Blomberg, S., Gustafson, J., Lundgren, E. & Zetterberg, J. Visualization of Gas Distribution in a Model AP-XPS Reactor by PLIF: CO Oxidation over a Pd(100) Catalyst. *Catalysts* **7**, 29 (2017).

127. Matera, S. & Reuter, K. Transport limitations and bistability for in situ CO oxidation at RuO 2 (110) : First-principles based multiscale modeling. *Phys. Rev. B* **82**, 085446 (2010).

128. Matera, S. & Reuter, K. When atomic-scale resolution is not enough: Spatial effects on in situ model catalyst studies. *J. Catal.* **295**, 261–268 (2012).

129. SPECS. PHOIBOS Hemispherical Energy Analyzer.

130. Green, D.W. and Perry, R. H. *Perry's Chemical Engineers' Handbook*. *McGraw-Hill Professional* **4**, (2007).

131. Martynova, Y. CO oxidation on metal supported ultrathin oxide films, PhD thesis. (Technische Universität Berlin, 2013).

132. Schwartz, S. B., Schmidt, L. D. & Fisher, G. B. Carbon monoxide + oxygen reaction on rhodium(III): steady-state rates and adsorbate coverages. *J. Phys. Chem.* **90**, 6194–6200 (1986).

133. Björneholm, O. *et al.* Overlayer structure from adsorbate and substrate core level binding energy shifts: CO, CCH3 and O on Pt(111). *Surf. Sci.* **315**, L983–L989 (1994).

134. Toyoshima, R. *et al.* A high-pressure-induced dense CO overlayer on a Pt(111) surface: a chemical analysis using in situ near ambient pressure XPS. *Phys. Chem. Chem. Phys.* **16**, 23564–23567 (2014).

135. Poelsema, B., Palmer, R. L. & Comsa, G. Helium scattering and work function investigation of co adsorption on Pt(111) and vicinal surfaces. *Surf. Sci.* **123**, 152–164 (1982).

136. Schnadt, J. *et al.* The new ambient-pressure X-ray photoelectron spectroscopy instrument at MAX-lab. *J. Synchrotron Radiat.* **19**, 701–704 (2012).

137. Axnanda, S. *et al.* Direct Work Function Measurement by Gas Phase Photoelectron Spectroscopy and Its Application on PbS Nanoparticles. *Nano Lett.* **13**, 6176–6182 (2013).

138. Dupin, J. C., Gonbeau, D., Vinatier, P. & Levasseur, A. Systematic XPS studies of metal oxides, hydroxides and peroxides. *Phys. Chem. Chem. Phys.* **2**, 1319–1324 (2000).

139. Wöll, C. The chemistry and physics of zinc oxide surfaces. *Prog. Surf. Sci.* **82**, 55–120 (2007).

140. Au, C. T., Hirsch, W. & Hirschwald, W. Adsorption and interaction of carbon dioxide, formic acid and hydrogen/carbon dioxide mixtures on (1010) zinc oxide surfaces studied by photoelectron spectroscopy (XPS and UPS). *Surf. Sci.* **199**, 507–517 (1988).

141. Senanayake, S. D. *et al.* Interaction of CO with OH on Au(111): HCOO, CO3, and HOCO as key intermediates in the water-gas shift reaction. *J. Phys. Chem. C* **113**, 19536–19544 (2009).

142. Lindsay, R. *et al.* Impact of Defects on the Surface Chemistry of ZnO(0001̄)−O. *J. Am. Chem. Soc.* **124**, 7117–7122 (2002).

143. Grabow, L. C., Gokhale, A. A., Evans, S. T., Dumesic, J. A. & Mavrikakis, M. Mechanism of the Water Gas Shift Reaction on Pt: First Principles, Experiments, and Microkinetic Modeling. *J. Phys. Chem. C* **112**, 4608–4617 (2008).

144. Shido, T. & Iwasawa, Y. Reactant-promoted reaction mechanism for water-gas shift reaction on ZnO, as the genesis of surface catalysis. *J. Catal.* **129**, 343–355 (1991).

145. Liu, B. H., Boscoboinik, J. A., Cui, Y., Shaikhutdinov, S. & Freund, H. J. Stabilization of ultrathin zinc oxide films on metals: Reconstruction versus hydroxylation. *J. Phys. Chem. C* **119**, 7842–7847 (2015).

146. Kiss, J., Frenzel, J., Nair, N. N., Meyer, B. & Marx, D. Methanol synthesis on ZnO(0001̄). III. Free energy landscapes, reaction pathways, and mechanistic insights. *J. Chem. Phys.* **134**, 064710 (2011).

147. Kiss, J., Frenzel, J., Meyer, B. & Marx, D. Methanol synthesis on ZnO(0001̄). II. Structure, energetics, and vibrational signature of reaction intermediates. *J. Chem. Phys.* **139**, 044705 (2013).

148. Rodríguez, J. A. & Hrbek, J. Inverse oxide/metal catalysts: A versatile approach for activity tests and mechanistic studies. *Surf. Sci.* **604**, 241–244 (2010).

149. Mahapatra, M. *et al.* The behavior of inverse oxide/metal catalysts: CO oxidation and water-gas shift reactions over ZnO/Cu(111) surfaces. *Surf. Sci.* **681**, 116–121 (2019).

150. Zhang, J. & Medlin, J. W. Catalyst design using an inverse strategy: From mechanistic studies on inverted model catalysts to applications of oxide-coated metal nanoparticles. *Surf. Sci. Rep.* **73**, 117–152 (2018).

151. Zhao, G. *et al.* Metal/oxide interfacial effects on the selective oxidation of primary alcohols. *Nat. Commun.* **8**, 14039 (2017).

152. Xu, L., Ma, Y., Zhang, Y., Jiang, Z. & Huang, W. Direct Evidence for the Interfacial Oxidation of CO with Hydroxyls Catalyzed by Pt/Oxide Nanocatalysts. *J. Am. Chem. Soc.* **131**, 16366–

16367 (2009).

153. Bose, S. *et al.* Polymer membranes for high temperature proton exchange membrane fuel cell: Recent advances and challenges. *Prog. Polym. Sci.* **36**, 813–843 (2011).

154. Costamagna, P. & Srinivasan, S. Quantum jumps in the PEMFC science and technology from the 1960s to the year 2000: Part II. Engineering, technology development and application aspects. *J. Power Sources* **102**, 253–269 (2001).

155. Curtin, D. E., Lousenberg, R. D., Henry, T. J., Tangeman, P. C. & Tisack, M. E. Advanced materials for improved PEMFC performance and life. *J. Power Sources* **131**, 41–48 (2004).

156. Sun, S. *et al.* A highly durable platinum nanocatalyst for proton exchange membrane fuel cells: Multiarmed starlike nanowire single crystal. *Angew. Chemie - Int. Ed.* **50**, 422–426 (2011).

157. Wang, C., Daimon, H., Onodera, T., Koda, T. & Sun, S. A general approach to the size- and shape-controlled synthesis of platinum nanoparticles and their catalytic reduction of oxygen. *Angew. Chemie - Int. Ed.* **47**, 3588–3591 (2008).

158. Markovic, N. M. & Ross, P. N. Surface science studies of model fuel cell electrocatalysts. *Surf. Sci. Rep.* **45**, 121–229 (2001).

159. Stamenkovic, V. R. *et al.* Trends in electrocatalysis on extended and nanoscale Pt-bimetallic alloy surfaces. *Nat. Mater.* **6**, 241–7 (2007).

160. Markovic, N. M., Gasteiger, H. A. & Ross, P. N. Oxygen reduction on platinum low-index single-crystal surfaces in sulfuric acid solution. Rotating ring - Pt(hkl) disk studies. *J. Phys. Chem.* **99**, 3411–3415 (1995).

161. Markovic, N. Kinetics of Oxygen Reduction on Pt(hkl) Electrodes: Implications for the Crystallite Size Effect with Supported Pt Electrocatalysts. *J. Electrochem. Soc.* **144**, 1591 (2006).

162. Service, R. F. Platinum in Fuel Cells Gets a Helping Hand. *Science (80-.).* **315**, 172–172 (2007).

163. Pei, J. *et al.* Ultrathin Pt-Zn Nanowires: High-Performance Catalysts for Electrooxidation of Methanol and Formic Acid. *ACS Sustain. Chem. Eng.* **6**, 77–81 (2018).

164. Qi, Z. *et al.* Sub-4 nm PtZn Intermetallic Nanoparticles for Enhanced Mass and Specific Activities in Catalytic Electrooxidation Reaction. *J. Am. Chem. Soc.* **139**, 4762–4768 (2017).

165. Carlotto, S., Sambi, M., Vittadini, A. & Casarin, M. Theoretical modeling of the L 2,3 -edge X-ray absorption spectra of Mn(acac) 2 and Co(acac) 2 complexes. *Phys. Chem. Chem. Phys.* **18**, 2242–2249 (2016).

166. Yu, Y. *et al.* Monodisperse MPt (M = Fe, Co, Ni, Cu, Zn) nanoparticles prepared from a facile

oleylamine reduction of metal salts. *Nano Lett.* **14**, 2778–2782 (2014).

167. Schwartz, V. B. *et al.* Antibacterial surface coatings from zinc oxide nanoparticles embedded in poly(N-isopropylacrylamide) hydrogel surface layers. *Adv. Funct. Mater.* **22**, 2376–2386 (2012).

168. Salavati-Niasari, M., Davar, F. & Mazaheri, M. Preparation of ZnO nanoparticles from [bis(acetylacetonato)zinc(II)]-oleylamine complex by thermal decomposition. *Mater. Lett.* **62**, 1890–1892 (2008).

169. Jiang, P. *et al.* CoP nanostructures with different morphologies: Synthesis, characterization and a study of their electrocatalytic performance toward the hydrogen evolution reaction. *J. Mater. Chem. A* **2**, 14634–14640 (2014).

170. Liu, J. F. *et al.* Synthesis of relatively monodisperse ZnO nanocrystals from a precursor zinc 2,4-pentanedionate. *Mater. Lett.* **61**, 2837–2840 (2007).

171. Yin, X. *et al.* Quantitative Analysis of Different Formation Modes of Platinum Nanocrystals Controlled by Ligand Chemistry. *Nano Lett.* **17**, 6146–6150 (2017).

172. Sun, S. & Zeng, H. Size-Controlled Synthesis of Magnetite Nanoparticles. *J. Am. Chem. Soc.* **124**, 8204–8205 (2002).

173. Uni, B. & Uni, P. Oleylamine as Both Reducing Agent and Stabilizer in a Facile Synthesis of Magnetite Nanoparticles. 1778–1780 (2009).

174. Song, L. *et al.* Influence of Reaction Solvent on Crystallinity and Magnetic Properties of MnFe 2 O 4 Nanoparticles Synthesized by Thermal Decomposition. **2016**, (2016).

175. Kahn, M. L. *et al.* Size- and Shape-Control of Crystalline Zinc Oxide Nanoparticles: A New Organometallic Synthetic Method. *Adv. Funct. Mater.* **15**, 458–468 (2005).

176. Xin, H. L. *et al.* Revealing the atomic restructuring of Pt-Co nanoparticles. *Nano Lett.* **14**, 3203–3207 (2014).

177. Wand, P., Bartl, J. D., Heiz, U., Tschurl, M. & Cokoja, M. Functionalization of small platinum nanoparticles with amines and phosphines: Ligand binding modes and particle stability. *J. Colloid Interface Sci.* **478**, 72–80 (2016).

178. Man, R. W. Y., Brown, A. R. C. & Wolf, M. O. Mechanism of Formation of Palladium Nanoparticles: Lewis Base Assisted, Low-Temperature Preparation of Monodisperse Nanoparticles. *Angew. Chemie Int. Ed.* **51**, 11350–11353 (2012).

179. Carenco, S. *et al.* Revisiting the Molecular Roots of a Ubiquitously Successful Synthesis: Nickel(0) Nanoparticles by Reduction of [Ni(acetylacetonate) 2]. *Chem. - A Eur. J.* **18**, 14165–

14173 (2012).

180. Carenco, S. Designing Nanoparticles and Nanoalloys with Controlled Surface and Reactivity. *Chem. Rec.* **18**, 1114–1124 (2018).

181. Günther, S. *et al.* In Situ X-ray Photoelectron Spectroscopy of Catalytic Ammonia Oxidation over a Pt(533) Surface. *J. Phys. Chem. C* **112**, 15382–15393 (2008).

182. Dziembaj, R. & Piwowarska, Z. X-ray photoelectron spectroscopy (XPS) as a useful tool to characterize polyaniline doped by 12-tungstosilicic, 12-tungstophosphoric and 12-molybdophosphoric acids. *Synth. Met.* **63**, 225–232 (1994).

183. Ballerini, G., Ogle, K. & Barthés-Labrousse, M. G. The acid-base properties of the surface of native zinc oxide layers: An XPS study of adsorption of 1,2-diaminoethane. *Appl. Surf. Sci.* **253**, 6860–6867 (2007).

184. Chen, J. J. & Winograd, N. The adsorption and decomposition of methylamine on Pd{111}. *Surf. Sci.* **326**, 285–300 (1995).

185. Jayalakshmi, G., Gopalakrishnan, N. & Balasubramanian, T. Activation of room temperature ferromagnetism in ZnO films by surface functionalization with thiol and amine. *J. Alloys Compd.* **551**, 667–671 (2013).

186. Maki, H. *et al.* Nitrogen Ion Behavior on Polar Surfaces of ZnO Single Crystals. *Jpn. J. Appl. Phys.* **42**, 75–77 (2003).

187. Zuo, J. & Erbe, A. Optical and electronic properties of native zinc oxide films on polycrystalline Zn. *Phys. Chem. Chem. Phys.* **12**, 11467–11476 (2010).

188. Heinhold, R., Williams, G. T., Cooil, S. P., Evans, D. A. & Allen, M. W. Influence of polarity and hydroxyl termination on the band bending at ZnO surfaces. *Phys. Rev. B - Condens. Matter Mater. Phys.* **88**, 38–40 (2013).

189. Wakisaka, M., Suzuki, H., Mitsui, S., Uchida, H. & Watanabe, M. Increased oxygen coverage at Pt-Fe alloy cathode for the enhanced oxygen reduction reaction studied by EC-XPS. *J. Phys. Chem. C* **112**, 2750–2755 (2008).

190. Hwang, S. Y., Seebauer, E. G. & Schmidt, L. D. Decomposition of CH3NH2 on Pt(111). *Surf. Sci.* **188**, 219–234 (1987).

191. Jentz, D., Trenary, M., Peng, X. D. & Stair, P. The thermal decomposition of azomethane on Pt(111). *Surf. Sci.* **341**, 282–294 (1995).

192. Felicíssimo, V. C. *et al.* A theoretical study of the role of the hydrogen bond on core ionization

of the water dimer. *Chem. Phys.* **312**, 311–318 (2005).

193. Carniato, S. *et al.* Characterization of hydroxyl groups on water-reacted Si(001)-2×1 using synchrotron radiation O 1s core-level spectroscopies and core-excited state density-functional calculations. *Phys. Rev. B* **76**, 085321 (2007).

194. O'Shea, J. N. *et al.* Hydrogen-bond induced surface core-level shift in pyridine carboxylic acids. *Surf. Sci.* **486**, 157–166 (2001).

195. Tu, G., Tu, Y., Vahtras, O. & Ågren, H. Core electron chemical shifts of hydrogen-bonded structures. *Chem. Phys. Lett.* **468**, 294–298 (2009).

196. Garcia-Gil, S., Arnau, A. & Garcia-Lekue, A. Exploring large O 1s and N 1s core level shifts due to intermolecular hydrogen bond formation in organic molecules. *Surf. Sci.* **613**, 102–107 (2013).

197. Humblot, V. *et al.* Characterization of Two-Dimensional Chiral Self-Assemblies l- and d-Methionine on Au(111). *Langmuir* **30**, 203–212 (2014).

198. Nicklin, R. E. J. *et al.* "Pop-On and Pop-Off" Surface Chemistry of Alanine on Ni{111} under Elevated Hydrogen Pressures. *J. Phys. Chem. C* **122**, 7720–7730 (2018).

199. de la Llave, E., Clarenc, R., Schiffrin, D. J. & Williams, F. J. Organization of Alkane Amines on a Gold Surface: Structure, Surface Dipole, and Electron Transfer. *J. Phys. Chem. C* **118**, 468–475 (2014).

200. Rignanese, G. M. & Pasquarello, A. First-principles study of NH3 exposed Si(001)2×1: Relation between N 1s core-level shifts and atomic structure. *Appl. Phys. Lett.* **76**, 553–555 (2000).

201. Patrick, C. E. & Giustino, F. Structure of a Water Monolayer on the Anatase TiO2 (101) Surface. *Phys. Rev. Appl.* **2**, 014001 (2014).

202. Rössler, N., Kotsis, K. & Staemmler, V. Ab initio calculations for the Zn 2s and 2p core level binding energies in Zn oxo compounds and ZnO. *Phys. Chem. Chem. Phys.* **8**, 697–706 (2006).

203. Pala, R. G. S. & Metiu, H. Modification of the Oxidative Power of ZnO(10$\bar{1}$0) Surface by Substituting Some Surface Zn Atoms with Other Metals. *J. Phys. Chem. C* **111**, 8617–8622 (2007).

204. Altuntasoglu, O., Matsuda, Y., Ida, S. & Matsumoto, Y. Syntheses of Zinc Oxide and Zinc Hydroxide Single Nanosheets. *Chem. Mater.* **22**, 3158–3164 (2010).

205. Giorgio, S. *et al.* Environmental electron microscopy (ETEM) for catalysts with a closed E-cell with carbon windows. *Ultramicroscopy* **106**, 503–507 (2006).

206. Engstrom, J. R., Tsai, W. & Weinberg, W. H. The chemisorption of hydrogen on the (111) and (110)-(1×2) surfaces of iridium and platinum. *J. Chem. Phys.* **87**, 3104–3119 (1987).

207. Ertl, G., Neumann, M. & Streit, K. M. Chemisorption of CO on the Pt(111) surface. *Surf. Sci.* **64**, 393–410 (1977).

208. Editor & H.P. Bonzel. Landolt-Börnstein Numerical Data and Functional Relationships in Science and Technology New Series / Editor in Chief: W. Martienssen Group III: Condensed Matter Volume 42 Physics of Covered Solid Surfaces Subvolume A Adsorbed Layers on Surfaces Part 4 Ads. in

209. Montano, M., Bratlie, K., Salmeron, M. & Somorjai, G. A. Hydrogen and Deuterium Exchange on Pt(111) and Its Poisoning by Carbon Monoxide Studied by Surface Sensitive High-Pressure Techniques. *J. Am. Chem. Soc.* **128**, 13229–13234 (2006).

210. Brodén, G., Pirug, G. & Bonzel, H. P. Chemisorption of CO on the unreconstructed Pt(100) surface. *Surf. Sci.* **72**, 45–52 (1978).

211. Martin, R., Gardner, P. & Bradshaw, A. M. The adsorbate-induced removal of the Pt{100} surface reconstruction. Part II: CO. *Surf. Sci.* **342**, 69–84 (1995).